CrossMark

Atmospheric Science with InSight

Aymeric Spiga[1,2] · Don Banfield[3] · Nicholas A. Teanby[4] · François Forget[1] ·
Antoine Lucas[5] · Balthasar Kenda[5] · Jose Antonio Rodriguez Manfredi[6] ·
Rudolf Widmer-Schnidrig[7] · Naomi Murdoch[8] · Mark T. Lemmon[9] ·
Raphaël F. Garcia[8] · Léo Martire[8] · Özgür Karatekin[10] · Sébastien Le Maistre[10] ·
Bart Van Hove[10] · Véronique Dehant[10] · Philippe Lognonné[5,2] · Nils Mueller[11,12] ·
Ralph Lorenz[13] · David Mimoun[8] · Sébastien Rodriguez[5,2] · Éric Beucler[14] ·
Ingrid Daubar[11] · Matthew P. Golombek[11] · Tanguy Bertrand[15] ·
Yasuhiro Nishikawa[5] · Ehouarn Millour[1] · Lucie Rolland[16] · Quentin Brissaud[17] ·
Taichi Kawamura[5] · Antoine Mocquet[14] · Roland Martin[18] · John Clinton[19] ·
Éléonore Stutzmann[5] · Tilman Spohn[12] · Suzanne Smrekar[11] · William B. Banerdt[11]

Abstract In November 2018, for the first time a dedicated geophysical station, the InSight lander, will be deployed on the surface of Mars. Along with the two main geophysical pack-

The InSight Mission to Mars II
Edited by William B. Banerdt and Christopher T. Russell

✉ A. Spiga
aymeric.spiga@sorbonne-universite.fr

1 Laboratoire de Météorologie Dynamique (LMD/IPSL), Sorbonne Université, Centre National de la Recherche Scientifique, École Polytechnique, École Normale Supérieure, Paris, France

2 Institut Universitaire de France, Paris, France

3 Cornell Center for Astrophysics and Planetary Science, Cornell University, Ithaca, NY, USA

4 School of Earth Sciences, University of Bristol, Wills Memorial Building, Queens Road, Bristol, BS8 1RJ, UK

5 Institut de Physique du Globe de Paris, Université Paris Diderot, Paris, France

6 CAB, Madrid, Spain

7 Institut für Geophysik, Universität Stuttgart, Stuttgart, Germany

8 Institut Supérieur de l'Aéronautique et de l'Espace (ISAE-SUPAERO), Université de Toulouse, 31400 Toulouse, France

9 Texas A&M university, College Station, TX, USA

10 Royal Observatory of Belgium, Brussels, Belgium

11 Jet Propulsion Laboratory, California Institute of Technology, Pasadena, USA

12 DLR, German Aerospace Center, Institute of Planetary Research, Berlin, Germany

13 Applied Physics Laboratory, Johns Hopkins University, Laurel, MD, USA

14 Laboratoire de Planétologie et Géodynamique, Université de Nantes, Nantes, France

ages, the Seismic Experiment for Interior Structure (SEIS) and the Heat-Flow and Physical Properties Package (HP^3), the InSight lander holds a highly sensitive pressure sensor (PS) and the Temperature and Winds for InSight (TWINS) instrument, both of which (along with the InSight FluxGate (IFG) Magnetometer) form the Auxiliary Sensor Payload Suite (APSS). Associated with the RADiometer (RAD) instrument which will measure the surface brightness temperature, and the Instrument Deployment Camera (IDC) which will be used to quantify atmospheric opacity, this will make InSight capable to act as a meteorological station at the surface of Mars. While probing the internal structure of Mars is the primary scientific goal of the mission, atmospheric science remains a key science objective for InSight. InSight has the potential to provide a more continuous and higher-frequency record of pressure, air temperature and winds at the surface of Mars than previous *in situ* missions. In the paper, key results from multiscale meteorological modeling, from Global Climate Models to Large-Eddy Simulations, are described as a reference for future studies based on the InSight measurements during operations. We summarize the capabilities of InSight for atmospheric observations, from profiling during Entry, Descent and Landing to surface measurements (pressure, temperature, winds, angular momentum), and the plans for how InSight's sensors will be used during operations, as well as possible synergies with orbital observations. In a dedicated section, we describe the seismic impact of atmospheric phenomena (from the point of view of both "noise" to be decorrelated from the seismic signal and "signal" to provide information on atmospheric processes). We discuss in this framework Planetary Boundary Layer turbulence, with a focus on convective vortices and dust devils, gravity waves (with idealized modeling), and large-scale circulations. Our paper also presents possible new, exploratory, studies with the InSight instrumentation: surface layer scaling and exploration of the Monin-Obukhov model, aeolian surface changes and saltation / lifing studies, and monitoring of secular pressure changes. The InSight mission will be instrumental in broadening the knowledge of the Martian atmosphere, with a unique set of measurements from the surface of Mars.

Keywords Mars · InSight · Atmospheric science · Planetary atmospheres

1 Introduction

The InSight 2018 Discovery mission (Banerdt et al. 2018) will land for the first time a dedicated, high-sensitivity, geophysical station on the surface of Mars, after the experimental seismic measurements on board the Viking landers (Anderson et al. 1977; Nakamura and Anderson 1979; Lorenz et al. 2017).

The InSight lander's instrumental suite comprises:

- Very-Broad-Band [VBB] and Short-Period [SP] seismometers (the Seismic Experiment for Interior Structure SEIS, see Lognonné et al. 2018, this issue), protected at the surface by a Wind and Thermal Shield (WTS);

15   NASA Ames Research Center, Mountain View, CA, USA

16   Geoazur, Université Côte d'Azur, Observatoire de la Côte d'Azur, Nice, France

17   Division of Geological and Planetary Sciences, California Institute of Technology, Pasadena, USA

18   Géoscience Environnement Toulouse, Observatoire midi-Pyrénées, Université de Toulouse, 31400 Toulouse, France

19   ETH, Zurich, Switzerland

- a subsurface heat flow and physical properties package (Heat-Flow and Physical Properties Package HP³, see Spohn et al. 2018, this issue) consisting of a penetrating mole at the surface and a radiometer (RAD) underneath the lander's deck;
- the Instrument Deployment System (IDS) comprising an arm to deploy the instruments onto the surface (Instrument Deployment Arm IDA, see Trebi-Ollennu et al. 2018, this issue) and two color cameras (Instrument Deployment Camera IDC & Instrument Context Camera ICC, see Maki et al. 2018, this issue) based on Navcam and Hazcam on board the Mars Exploration Rovers (MER, Spirit & Opportunity) and Mars Science Laboratory (MSL, Curiosity);
- an X-band radio Doppler receiver/transponder to detect rotational variations of Mars (Rotation and Interior Structure Experiment RISE, see Folkner et al. 2018, this issue);
- and the Auxiliary Payload Sensor Suite (APSS, see Banfield et al. 2018, this issue) comprising a magnetometer (InSight Flux Gate IFG, see Russell et al. 2018, this issue), and a meteorological station composed of a highly sensitive pressure sensor (PS), and two meteorological booms measuring wind and temperature (Temperature and Winds for InSight, TWINS) akin to the meteorological package on the Curiosity rover (Rover Environmental Monitoring Station REMS, see Gómez-Elvira et al. 2012, 2014).

The InSight mission's highest level goal is to understand the processes of formation and differentiation that have occurred on terrestrial planets (Banerdt et al. 2018). Thus, the major science objectives of the InSight mission to Mars are to probe the seismic activity of an extraterrestrial body, to measure its internal heat flux, and to reconstruct the structure of the interior of the planet. Yet atmospheric science remains a key science objective for InSight, for a variety of reasons.

First and foremost, a thorough assessment of the seismic noise caused by the atmosphere is a key element of success of the primary science goals of the mission. This is why InSight carries a complement of meteorological sensors, so as to understand when winds preclude good seismology and to possibly remove meteorological effects from the seismic signals. The Viking seismology experiments demonstrated that winds can have a significant effect on seismometry (e.g., Anderson et al. 1977; Nakamura and Anderson 1979). InSight will mitigate this effect to a much larger degree than did Viking by placing its seismometers directly in contact with the ground, isolating them from the lander via a tether, and covering the seismometers with a WTS. Nevertheless, it is expected that local wind and pressure perturbations will influence the observed seismic signals. (See Fig. 1.)

Secondly, from the atmospheric science standpoint, InSight also opens new, interesting perspectives to complement the measurements carried out by previous landers on Mars. In addition to extending the record of atmospheric observations at the surface of Mars, the mission will enable new atmospheric science experiments. For instance, along with meteorological measurements of temperature and winds, InSight will be able to acquire continously atmospheric pressure at high frequency and unprecedented accuracy. Furthermore, the wind-induced seismic signal itself may permit original atmospheric science studies. InSight is a good prototype for a future network of geophysical-meteorological stations at the surface of Mars, similar to such networks deployed on the Earth.

The objective of this paper is neither to provide an exhaustive description of InSight's instrumentation, nor to describe in detail every scientific investigation of the mission. This paper reviews the atmospheric science investigations to be carried out with the InSight lander

Fig. 1 Artist's view of the
InSight lander in a typical
early-morning scene on Mars
with a dust devil passing nearby.
Reproduction of an original
drawing by artist Manchu, used
with permission under copyright
IPGP/Manchu/Bureau 21

when it reaches the surface of Mars. The paper does not focus on a particular InSight instrument; it underlines how synergy between instruments will be established and be helpful to advance the knowledge of atmospheric processes on Mars. Key results from meteorological modeling[1] and past surface and orbital meteorological measurements are described to provide a reference for future studies based on InSight measurements (Sect. 2). The capabilities of InSight for observations of interest for atmospheric science (Sect. 3) and the current plans for how its sensors will be operated and joint orbital / surface measurements (Sect. 4) are summarized. A particular emphasis is put in Sect. 5 to describe the atmospheric information contained in seismic measurements. Section 6 features exploratory ideas of atmospheric science with InSight that are being developed in anticipation of InSight's unique data sets. Conclusions are summarized in Sect. 7 about the impact of the InSight mission on the understanding wind regimes at all scales on Mars, on the detection of both known, and yet unknown, pressure variations, on the assessment of atmosphere-induced seismic noise (both for decorrelation with the geophysical seismic signal and for atmospheric investigations), on the monitoring of the Martian dust and water cycles, and on the possible joint observing campaigns with orbiting spacecraft.

---

[1]The assessment of atmospheric conditions, and possible hazards, during InSight's Entry, Descent, Landing (EDL) and Surface Operations is out of the scope of the present paper, and will be pusblished in a separate study, as was the case for previous missions landing on Mars (Kass et al. 2003; Vasavada et al. 2012).

2 Expected Meteorology at the InSight Landing Site

2.1 Previous Surface-Based Data

Measurements by landers and rovers provide unique information about Mars' near-surface atmosphere. These data provide accurate and high resolution spot measurements of a landing site and are complementary to global and regional measurements obtained from orbiters (see Sect. 4.3), which do not have the vertical resolution to provide information on the centimeter and meter scales.

Existing measurements of Mars' near-surface atmospheric properties are comprehensively summarized by Martínez et al. (2017), who compiled measurements from the Viking 1, Viking 2, and Phoenix landed platforms and those by the MER Spirit and Opportunity, Pathfinder, and MSL Curiosity. Meteorological measurements included surface pressure, atmospheric temperature, relative humidity, atmospheric opacity, and wind speed and direction.

These measurements display similarities between the different landing sites, unveiling the main properties of Martian weather (Read and Lewis 2004; Haberle et al. 2017): strong diurnal cycle of atmospheric temperature and winds, seasonal variations of pressure under the influence of CO_2 condensation / sublimation on polar caps, low absolute humidity but relative humidity close to (and even reaching, e.g. at the Phoenix landing site) saturation, distinctive signatures of planetary mesoscale turbulent waves, and vortices. Nevertheless, there is also a high degree of site dependence. Therefore, it is essential that each lander or rover carries its own meteorology suite, both for characterizing in greater detail the local impact of circulations at all scales, from global-scale to Planetary Boundary Layer (PBL) processes, and for supporting other science measurements, which can be strongly affected by local weather conditions. This is especially critical for InSight where the seismometer performance and noise will all depend on atmospheric conditions (see Sect. 4.2, and Mimoun et al. 2017; Murdoch et al. 2017a; Teanby et al. 2017; Kenda et al. 2017).

Pressure and temperature have been best characterized so far, with long time-series of relatively high sample rate data returned for multiple Mars years from the Viking landers (Sutton et al. 1978; Tillman et al. 1979), Pathfinder (Schofield et al. 1997; Murphy and Nelli 2002), Phoenix (Davy et al. 2010; Ellehoj et al. 2010), and MSL (Harri et al. 2014; Haberle et al. 2014; Gómez-Elvira et al. 2014). Wind speed and direction have proved to be more challenging, including measurements taken by heated wire/film wind sensors (Taylor et al. 2008; Gómez-Elvira et al. 2012) and camera imaging of wind socks (Sullivan et al. 2000), some of which have been beset by calibration problems or instrument damage (Martínez et al. 2017). Figure 2 shows sol-averaged pressure and air temperature recorded by the REMS sensor suite (Gómez-Elvira et al. 2012; Haberle et al. 2014) on MSL during the first 1648 sols of the mission (2012–2017). Both pressure and temperature seasonal cycles are clearly evident. The temperature is a probe of the local atmosphere and strongly depends on latitude; with the MSL landing site being close to the equator, the seasonal variation in temperature is a modest ∼20 K. Larger seasonal temperature amplitudes are observed by landers closer to the poles such as Viking 2 (Martínez et al. 2017). Conversely the pressure is a probe of both local and global phenomena; for example, the pressure minima around Sol 0, 650, and 1300 are due to freeze-out of atmospheric CO_2 onto the south polar ice cap during the cold and long southern winter. The lowest pressure value corresponds with late southern winter.

Pressure also undergoes variations over timescales shorter than the seasonal timescale, either on a diurnal basis or on a couple days due to atmospheric thermal tides (Wilson and

Fig. 2 Pressure and temperature recorded by the REMS instrument suite on board the Mars Science Laboratory (Curiosity Rover). Sol is relative to the landing date. Pressure and temperature data were averaged on a per-sol basis, where sols with incomplete data coverage being removed from the plot. The temperature and pressure seasonal cycles are clearly evident
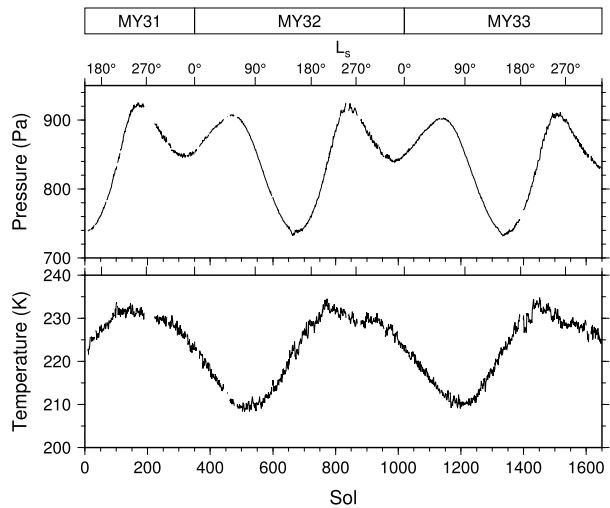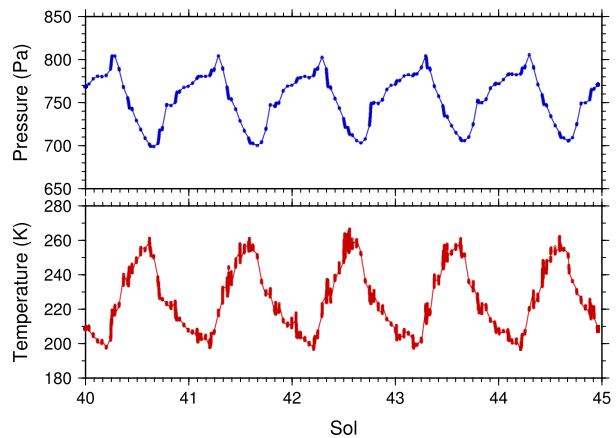
Fig. 3 Raw pressure and air temperature measurements from the REMS instruments on MSL for sol 40–45. There is a clear diurnal pressure variation, due to thermal tides, and a ∼60 K day-night temperature variation. The amplitude of pressure variation at the InSight landing site is expected to be weaker by up to a factor of two (see Fig. 7)

Hamilton 1996; Forget et al. 1999; Lewis and Barker 2005; Guzewich et al. 2016) and the motion of baroclinic eddies (Haberle et al. 2018). Figure 3 shows variations over a 5-sol period measured by MSL. The bulk of the variation can be explained by thermal tides (diurnal and higher harmonics). Due to the constructive interference of eastward and westward propagating tidal modes (Guzewich et al. 2016), as well possible contributions from topography effects (Wilson et al. 2017), the diurnal pressure variation within Gale crater is higher than that observed by other missions. There are many other shorter-period (less than an hour) pressure variations too, caused by gravity waves (Gossard and Munk 1954; Spiga et al. 2007) and turbulence (Sutton et al. 1978; Haberle et al. 2014, and see Sect. 2.3), including convective vortices (Kahanpää et al. 2016; Spiga et al. 2016; Martínez et al. 2017), which give rise to dust devils shall dust be lifted and transported within the vortex (Murphy et al. 2016). These shorter-period pressure variations are of particular relevance to InSight, as they can induce ground deformation at seismic frequencies (Sect. 5).

2.2 Predictions Using Past Orbital Observations and Global Climate Models

Insight will land near the equator at about the same longitude as Curiosity and Viking Lander 2, in the western Elysium Planitia region (about 500 km north of the Curiosity landing site in Gale Crater). The 130×27 km landing ellipse is centered at 4.5° N 135.9° E on smooth plains (complete details on the InSight landing site, and selection thereof, can be found in Golombek et al. 2018). The landing date (November 26th, 2018) corresponds[2] to solar longitude $L_s = 295°$ on Martian Year 34. The lander is designed to operate on the surface of Mars for one Martian year (two Earth years).

The expected meteorology at the Insight Landing site can be described on the basis of the data gathered remotely from orbit since 1999 by the Mars Global Surveyor (MGS), Mars Odyssey (ODY), Mars Express (MEx) and Mars Reconnaissance Orbiter (MRO). When no data are available (e.g. for pressure or winds) we can use prediction from 3D atmospheric models. In what follows, we use Global Climate Modeling (GCM) predictions performed with the up-to-date version of the Laboratoire de Météorologie Dynamique (LMD) GCM (Forget et al. 1999), and in particular the high resolution (1 degree latitude by 1 degree longitude) simulations presented by Pottier et al. (2017).

2.2.1 Atmospheric Dust Opacity

On Mars, local conditions and the meteorological day-to-day and interannual variability are controlled by the amount of dust in the atmosphere. It has been monitored for several years from orbit and *in situ*. Figure 4 presents records of the visible column dust optical depth remotely observed at the Insight landing site since 1999 (Martian years 24–33). The atmospheric dust climatology was reconstructed and carefully interpolated at all locations on the planet using observations from the MGS Thermal Emission Spectrometer (TES), the ODY THermal Emission Imaging System (THEMIS), and the MRO Mars Climate Sounder (MCS), using the methods described in Montabone et al. (2015).

The seasonal evolution of dust follows the typical low-latitude variations that are now well known on Mars (Read and Lewis 2004; Haberle et al. 2017). At the beginning of each year, during northern spring and early summer (until about $L_s = 130°$), very little dust lifting occurs on Mars and the dust opacity slowly decreases as the airborne dust sedimentates on the ground. The expected interannual variability is small. Moderate local dust activity appear in MY27 and MY28 in early northern summer. However these variations may be artifacts, since those particular years were not well observed (not by TES nor MCS, see Montabone et al. 2015). During most years (except in MY25, discussed below), after $L_s = 130°$ and until $L_s = 200°$, dust starts to reaccumulate in the atmosphere, mostly because dust lifting occurs at the southern polar cap edge (Cantor et al. 2001). The largest increase then usually occurs between $L_s = 210°$ and 240°, notably due to baroclinic activity at northern high and mid latitudes (Collins et al. 1996; Hollingsworth et al. 1996). This favors regional storms which can sometime cross the equator ("flushing storms", see e.g. Wang et al. 2003).

After $L_s = 250°$, there is usually a clear decrease of dust loading in the Martian atmosphere. There are fewer large storms, most likely because of the the decrease in the amplitude of low-altitude northern baroclinic waves around northern winter solstice (the so-called

---

[2]Solar longitude L_s characterizes the position of Mars on its orbit around the Sun, $L_s = 0°$ corresponding to northern spring equinox. Martian Years (MY) were defined by Clancy et al. (2000), to ease the intercomparison of measurements across several space missions to Mars, and ground-based telescope campaigns, with Martian Year 1 beginning on April 11th, 1955.
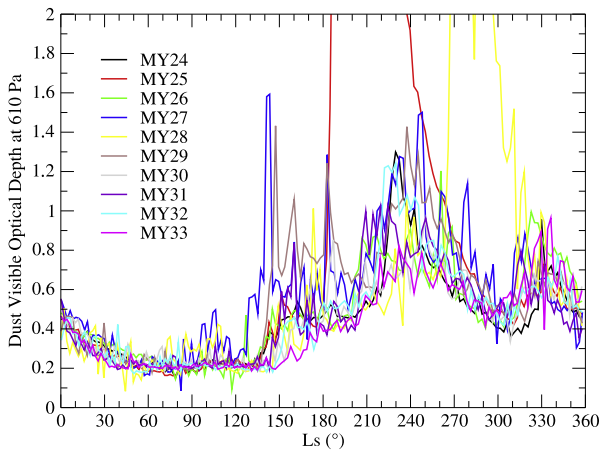
Fig. 4 Seasonal evolution of the visible dust column optical depth (normalized at pressure level 610 Pa) reconstructed at the Insight Landing site as in Montabone et al. (2015) from various remote sensing observations. This dataset originally contains infrared opacities at 1075 cm^{-1}. These opacities are multiplied by 2.6 to provide dust optical depth in the visible as will be observed by Insight. The actual visible opacity that would have been observed by Insight is obtained by multiplying the values shown here by $P_s/610$ with P_s being the surface pressure (Pa)

"solsticial pause", see Lewis et al. 2016; Mulholland et al. 2016, and references therein) Once the solsticial pause is over, around $L_s = 300°$, the baroclinic wave activity at low altitude is strong again, hence the probability of late flushing storms increases. As a consequence, every year, a third annual maximum of dust opacity occurs between $L_s = 310°$ and $L_s = 350°$.

The Martian Years 25 and 28 were different from most years since planetary encircling dust storms (i.e. global dust storms Cantor 2007) shrouded the planet during the entire northern fall of MY25 and most of the winter of MY28. Mars was then in a different meteorological regime. In both cases, the visible dust opacity was above 4 for several weeks at the Insight Landing site. No such events have occured since MY28. However, planetary-encircling storms were previously observed in Martian Years 9, 10, 12, 15, 21 and 25 (Martin and Zurek 1993; Cantor 2007). Assuming that the interranual variability of global dust storms is controlled by the redistribution of dust on Mars over a few years timescale (Mulholland et al. 2013; Vincendon et al. 2015), it seems likely that Insight will witness a planetary-encircling dust storm during its lifetime.

At the time of revising this manuscript (June 2018, Martian Year 34, $L_s \sim 185$–190°), a large dust storm started near MER Opportunity's location, moved southward along the Acidalia storm-track and expanded both along the northern hemisphere from eastern Tharsis to Elysium, at the landing sites of Curiosity and InSight, and towards the southern hemisphere (Malin et al. 2018). It appears that this large-scale dust storm is likely to become a planet-encircling dust event as in MY25 and MY28; it is unlikely however that this major storm will last until the InSight landing on MY34 $L_s = 295°$ (Martin and Zurek 1993; Montabone et al. 2015). At any event, this major storm in early fall will possibly induce a different meteorological regime in winter that will be interesting to monitor with meteorological measurements on board InSight (see Sect. 3).

The occurrence of this major storm in MY34 prior to the InSight landing does not tell anything about the probability of InSight to witness a planetary-encircling dust storm either
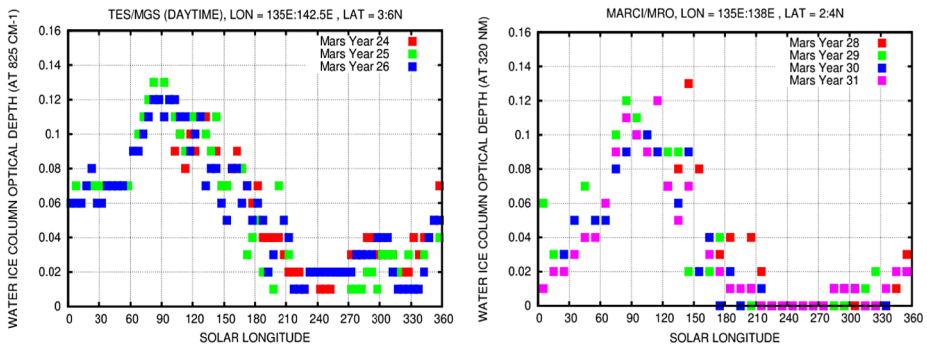
Fig. 5 Seasonal evolution of the water ice clouds observed during daytime above the Insight landing site. Top: Cloud opacity at 12.1 μm (825 cm^{-1}) at about 2pm local time as retrieved by Smith (2004) from the MGS/TES observations. Bottom: Cloud daytime UV opacity at 0.320 μm as retrieved by Wolff et al. (2014) from the MRO/MARCI observations. Assuming simple spherical shapes for water ice particles with effective radius 3 microns, the TES opacity at 12.1 μm can be converted to the MARCI opacity at 0.320 μm by multiplying by a factor ∼ 1.86 [1.37 to account for the absorption (TES) vs. extinction (MARCI) difference (Wolff and Clancy 2003) and 1.36 to account for the wavelength difference (Clancy et al. 2003)]. Note that water ice opacity has also been retrieved from several other instruments (e.g. THEMIS, PFS): only TES and MARCI results are shown here for the sake of simplicity

during landing on MY34 at $L_s = 295°$ (see Sect. 3) or during operations in MY35. Famous examples are the two planet-encircling dust events that were successively monitored by the Viking landers in 1977 at $L_s = 205°$ and $L_s = 275°$ (Ryan and Henry 1979; Zurek 1982). And one Martian Year later, Ryan and Sharman (1981) reported a major large-scale dust storm that occurred at the exact same season as the first 1977 Viking planet-encircling dust event.

2.2.2 Water Ice Clouds Coverage

Figure 5 presents the seasonal variations of daytime ice cloud opacity remotely observed above the Insight Landing site by MGS/TES in the thermal infrared (Smith 2004) and MRO Mars Color Imager (MARCI) in the UV at the Insight landing site (Wolff et al. 2014). At equatorial latitudes, the annual cycle is characterized by the presence of clouds in spring and summer with a maximum near northern summer solstice. Insight will be located in a relatively cloudy part of this "Aphelion Cloud Belt" (see Fig. 16 in Smith (2004) and Fig. 11 in Pankine et al. (2013)). Surface fog may form around the Insight Lander. This cannot be remotely characterized, but GCM simulations suggest the presence of fogs at two periods (not shown): between $L_s = 70°$ and $L_s = 150°$ (when absolute humidity is maximum) and between $L_s = 250°$ and $L_s = 310°$ (when temperatures are minimum).

2.2.3 Surface Pressure Variations

Assuming that the exact location of the Insight Lander is known, it is possible to predict the atmospheric pressure that will be observed by Insight with good accuracy, by combining information from the high resolution MOLA topography datasets, the seasonal cycle observed by Viking Lander 1, and the horizontal pressure gradient calculated with the LMD GCM (see details on the method in Sect. 4.2 of Forget et al. 2007). This tool is featured in the Mars Climate Database (MCD) version 5 (Millour et al. 2015). Sensitivity studies to key

Fig. 6 Predicted seasonal evolution of the mean surface pressure at the Insight Landing site (4.5° N, 135.9° E, −2662 m) outside global dust storm period (see text). The thick solid line corresponds to the daily mean surface pressure. The thin solid lines shows the daily maximum and minimum surface pressure and illustrate the amplitude of the effect of thermal tides
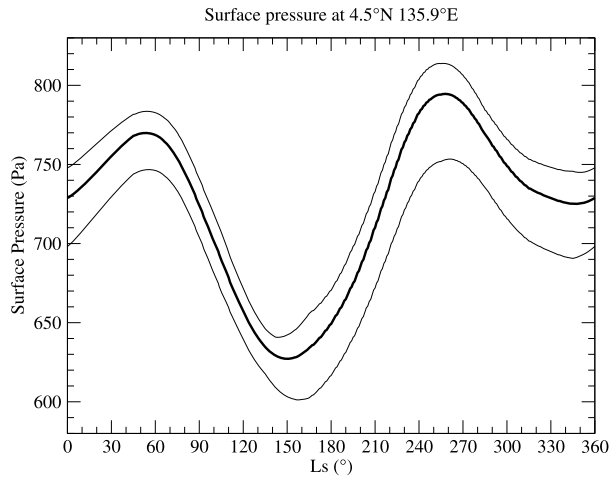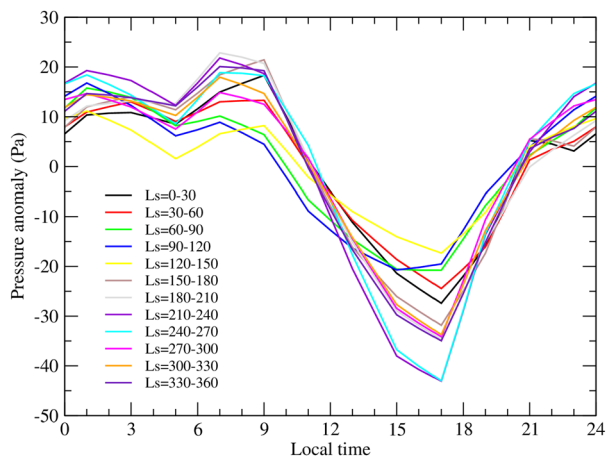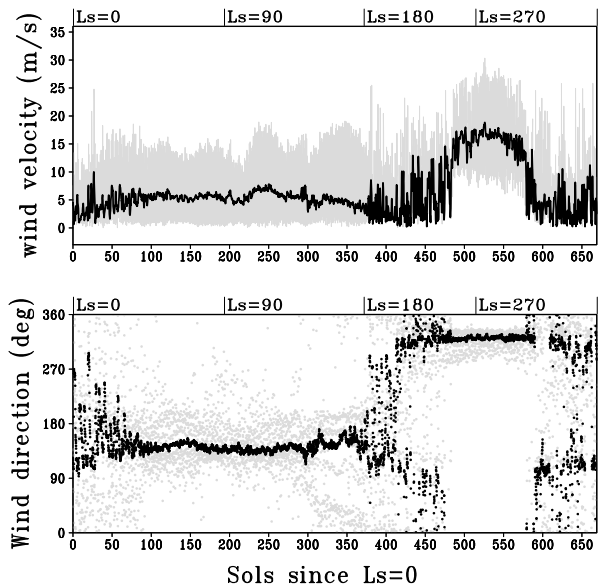

Fig. 7 The diurnal oscillation of surface pressure (difference with diurnal mean value) at the Insight landing site as predicted by the LMD Global Climate Model (twelve values per day are included). This shows the signature of the diurnal and semi-diurnal thermal tide

GCM parameters and validation with other lander measurements (e.g. see Fig. 3 in Millour et al. 2014) have demonstrated an accuracy of the order of a percent at a given season and local time at low latitudes (i.e. where baroclinic waves effects are almost negligible).

Figure 6 shows the MCD5 predictions of the pressure at 4.5° N 135.9° E (MOLA altitude: −2662 m). The pressure slowly varies on a seasonal basis as a result of both the deposition and sublimation of CO_2 in the seasonal ice caps and the seasonal changes in the atmospheric global structure and dynamics (Hourdin et al. 1993). The expected annual surface pressure cycle ranges from ∼ 600 to 800 Pa, which is well within the valid range for InSight PS measurements (see Sect. 3.2.2). In addition, every day, the surface pressure is expected to undergo large variations due to the diurnal and semi-diurnal thermal tides (Wilson and Hamilton 1996; Lewis and Barker 2005; Guzewich et al. 2016). The thin lines on Fig. 6 illustrate the daily maximum and minimum surface pressure and thus the amplitude of this variations which reaches 60 Pa during the dusty seasons (dust then absorbs solar radiation and enhances the atmospheric diurnal cycle). The variation of pressure as a function of local time and for different seasons is shown on Fig. 7. The pressure measurements should also exhibit day-to-day variations created by baroclinic waves. However, at such a low latitude

Fig. 8 Evolution of the near-surface wind (at 4 m above ground) at the Insight landing site as predicted by the LMD Global Climate Model. The black line and dots shows the diurnal-mean wind and the grey line and dots illustrate the diurnal cycle variations (8 points per day). The angle of the wind direction corresponds to: $0° =$ southward; $90° =$ westward; $180° =$ northward; $270° =$ eastward. Note that the diurnal-mean wind direction is not informative when the wind direction varies through a full $360°$ over one Martian sol, such as e.g. in the range $L_s = 0$–$25°$

the GCM predicts limited peak-to-peak amplitudes below 5 Pa during most of the year, with only a few period after $L_s = 300°$ when it can reach 10 Pa (see also the Curiosity measurements in Haberle et al. 2018).
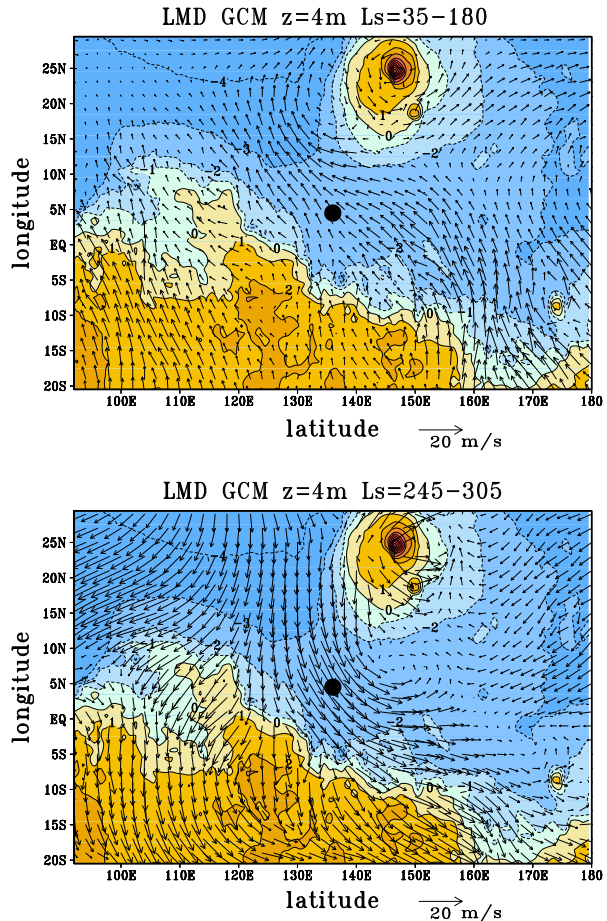
2.2.4 Near-Surface Winds

No wind observations are available in the Insight landing site region. Here again, we use the LMD Global Climate Model (Forget et al. 1999) and in particular the 1 degree latitude by 1 degree longitude simulation presented by Pottier et al. (2017) to present a prediction of the near-surface wind (at 4 m above the ground, height of the lowest model level). Those predictions correspond to a typical year without global dust storm. Figure 8 shows the evolution of the wind magnitude and direction over one year, and Figs. 9 and 10 present several maps of time-averaged winds to illustrate the different wind regimes that the GCM predicts at the Insight landing site. The wind speed measured by InSight about 1 m above the surface will be lower (typically 10–20%) than what is predicted by models 4 m above the ground, owing to the friction exerted by the surface (see Sect. 6.1).

The main wind regime $\mathcal{R}_1$ is found during Northern spring and summer between $L_s = 35°$ (sol 70) and $L_s = 180°$ (sol 372), a period characterized by stable winds towards the north-west (Fig. 9, top) which corresponds to the northward return branch of the Hadley circulation modulated by Coriolis force and the regional topography (western boundary current). The wind velocity reaches 15–20 m s^{-1} in the afternoon, when the daytime mixing by turbulence in the boundary layer (see Sect. 2.3) brings momemtum from the atmosphere above. Conversely, surface wind velocities are minimum during nightime. The diurnal cycle induces limited oscillations in the wind direction, but does not create a full rotation of the wind direction as was notably observed by Pathfinder (Schofield et al. 1997), probably because the regional slope is very flat.

The opposite wind regime to $\mathcal{R}_1$, denoted $\mathcal{R}_2$, is observed between $L_s = 245°$ (sol 475) and $L_s = 305°$ (sol 570). During this period around southern summer solstice, the return

Fig. 9 Mean near-surface winds (at 4 m above ground) in the Insight landing site area as predicted by the LMD Global Climate Model (Forget et al. 1999; Pottier et al. 2017) for two characteristic periods of the atmospheric circulation (regime $\mathcal{R}_1$ at $L_s = 35$–180° on top panel and regime $\mathcal{R}_2$ at $L_s = 245$–305° on bottom panel). During those two characteristic periods, the wind direction does not change much over the course of one Martian sol (see Fig. 8), hence showing here the diurnal average is meaningful. The black dot illustrates the location of InSight. Color shading shows the underlying topography

branch of the Hadley circulation corresponds to stable winds towards the south-east (Fig. 9, bottom). Winds are stronger during this season primarily because of the larger dust loading and insolation (near perihelion). These result in larger south-north temperature contrast and a more intense Hadley cell. Wind velocities can reach 30 m s^{-1} in the afternoon. Interestingly, the preferential north-west / south-east direction of the two main wind regimes $\mathcal{R}_1$ and $\mathcal{R}_2$ is compliant with surface erosion structures in the vicinity of the InSight landing site (see Golombek et al. 2018, and Sect. 6.2).

Between these two clear-cut regimes $\mathcal{R}_1$ and $\mathcal{R}_2$, the GCM predicts periods of transition in the landing site area which may be very interesting to monitor with Insight's instruments. The winds oscillate between distinct regimes with a period which can be as low as two sols (see Fig. 8, starting from sol 400 and sol 600). This oscillation is shown on Fig. 10 which presents maps of the diurnal-mean wind vectors on two consecutive sols around $L_s = 345°$.

Since the InSight landing site is relatively flat, the local wind is mostly controlled by the large scale circulation. As a result, the GCM runs carried out at an horizontal resolution of 60 km should be adequate to predict Insight measurements. The mesoscale modeling we performed for the InSight landing site, using the Spiga and Forget (2009) model with an horizontal resolution of about 10–20 km, yields results very similar to the GCM results presented here, with similar wind regimes. Differences in wind speeds between the LMD
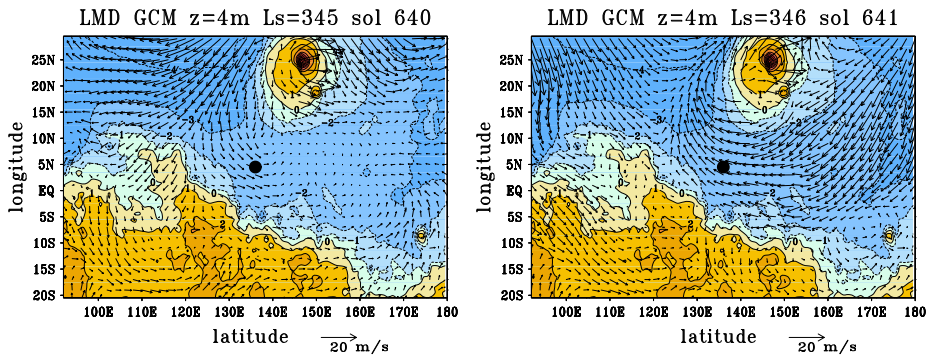
Fig. 10 Diurnally-averaged near-surface winds (at 4 m above ground) in the Insight landing site area as predicted by the LMD Global Climate Model for two consecutive sols in late northern winter, a period when the wind direction oscillates from sol to sol. The black dot illustrates the location of InSight. Color shading shows the underlying topography
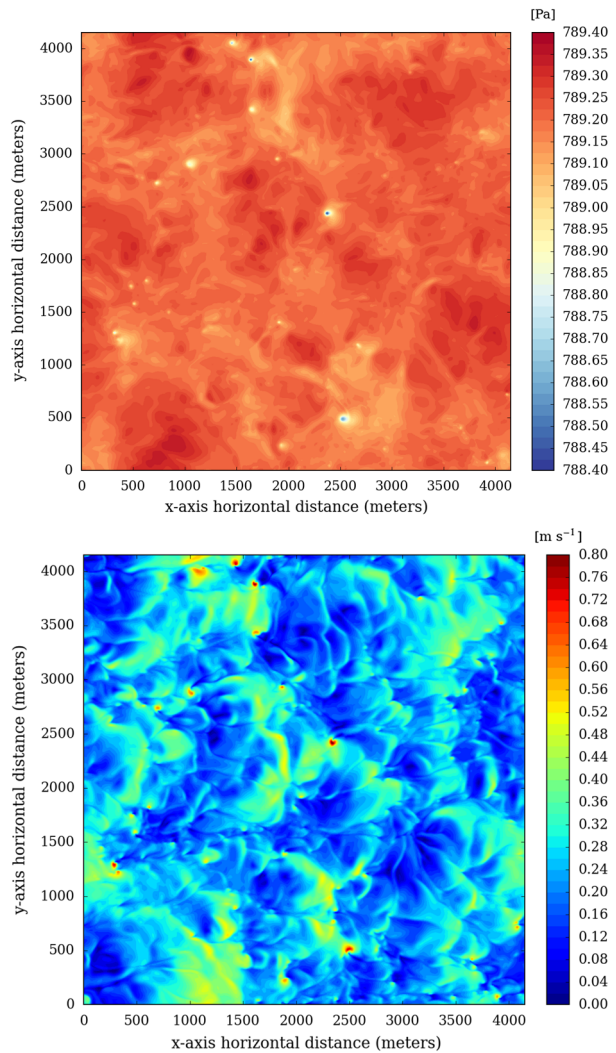
GCM and mesoscale model are of the order 10% (maximum 30%), as a result of a better resolution of both local topography and the dichotomy boundary, which cause slope winds. The situation of the InSight landing site is very different from the MSL landing site in Gale Crater, where the topography-induced circulations are a key component of the variability of the pressure, temperature, wind observed by Curiosity and require the use of high-resolution mesoscale modeling to interpret this variability (Tyler and Barnes 2015; Rafkin et al. 2016; Pla-Garcia et al. 2016; Wilson et al. 2017; Steele et al. 2017).

2.3 Local Turbulence

In contrast to the highly-stable conditions that prevails in the nighttime Martian near-surface atmosphere, near-surface gradients of atmospheric temperature in the daytime are conducive to convective instability (Sutton et al. 1978; Schofield et al. 1997; Sävijarvi 1999; Smith et al. 2006), causing the Planetary Boundary Layer (PBL) to become a mixing layer several kilometers deep (Tillman et al. 1994; Hinson et al. 2008). As is the case for the vast majority of Martian regions, the InSight landing site is prone to this convective PBL mixing in the daytime. Convective motions in the daytime PBL cause atmospheric pressure, wind, and temperature to undergo high-frequency variations in the range 0.1–1 Hz. To assess the properties of the daytime PBL dynamics, we use Large-Eddy Simulations (LES) in which are resolved the largest turbulent eddies—plumes, cells, vortices, responsible for most of the momentum and heat transport within the daytime PBL (Lilly 1962). LES have been used to study the Martian PBL for about two decades (see Petrosyan et al. 2011; Spiga et al. 2016, for a review).

LES with the model of Spiga et al. (2010) are carried out in environmental conditions corresponding to the location of the InSight landing site in Elysium Planitia at the season of landing (early northern winter). We base our discussions here on simulations similar to those used in Murdoch et al. (2017a) and Kenda et al. (2017) to assess the seismic impact of PBL turbulence (see Sect. 5 for this topic). The major difference is that we refined the spatial resolution in our LES to 10 m on a 417×417 horizontal grid, with a 301-level vertical grid from the surface to an altitude of 6 km, and an integration timestep of 1/10 s. Using this resolution allows for a better sampling of the diversity of convective vortices occurring in the Martian daytime turbulence (Nishizawa et al. 2016). A 5 m s^{-1} ambient wind is prescribed

Fig. 11 Horizontal maps of surface pressure (top) and friction velocity (bottom), as predicted by the 10-m resolution turbulence-resolving LES described in the text, based on the model by Spiga et al. (2010). Conditions are close to 9 AM local time. The impact of both convective vortices, and gusts associated with convective cells, can be noticed on those maps. Friction velocity is a proxy for near-surface winds (see Sect. 6.1) and their ability to exchange heat and material between the surface and atmosphere

in the x-direction to emulate the influence of a regional-scale circulation. The LES run is only carried out for 2 hours and half after the starting local time of 7 AM (sunrise is between 5 and 6 AM), to ensure that the horizontal extent of the convective cells is always smaller than about $2 - 3$ times the domain extent (Mason 1989; Tyler et al. 2008). The quantitative results shown below, particularly the amplitude of turbulent fluctuations, are expected to be larger in late morning / early afternoon.

In Martian LES, convective plumes (updrafts and downdrafts) are organized horizontally as polygonal convective cells with narrow updrafts and broader downdrafts, associated with horizontal wind gusts close to the surface (Michaels and Rafkin 2004; Kanak 2006; Tyler et al. 2008; Spiga et al. 2010). In convergence branches of the simulated cellular convective cells, convective vortices are naturally resolved by LES. All those phenomena are present in the simulated LES surface pressure field shown in Fig. 11 (top): convective vortices as characteristic circular pressure drops of typical amplitude 1 Pa, and convective cells
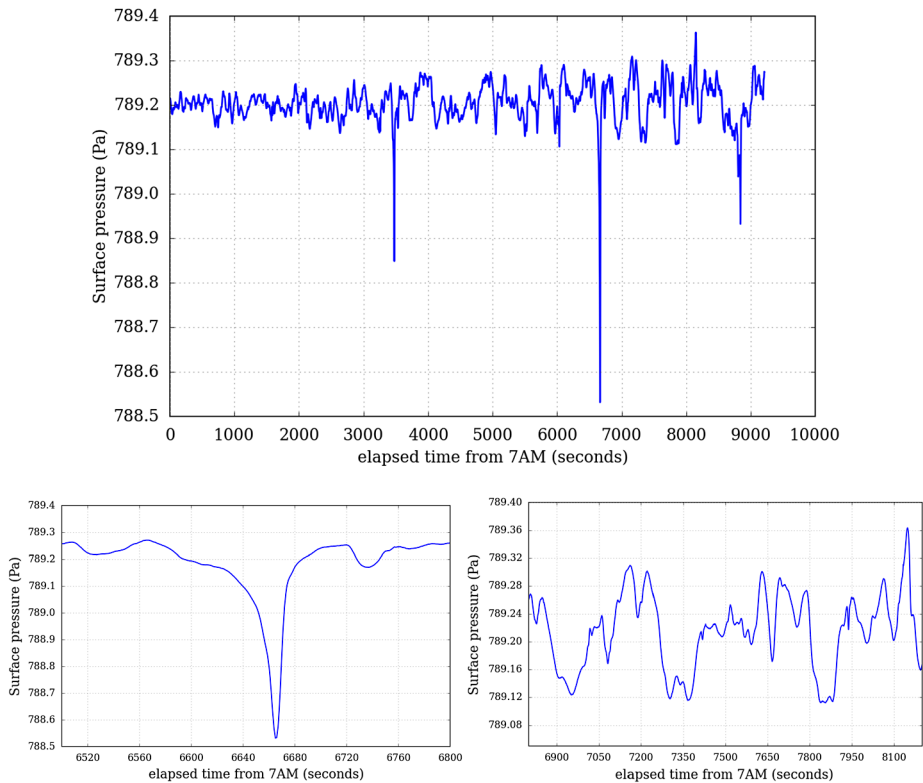
Fig. 12 Temporal 1-Hz series of surface pressure predicted by the 10-m resolution turbulence-resolving LES model. The location corresponds to the central pressure drop in Fig. 11. This figure emulates what would be observed by the InSight PS. The two bottom magnified views correspond to the two notable phenomena in the pressure temporal variations: sudden pressure drops corresponding to a passing convective vortex (a "dustless" devil, see e.g. Spiga et al. 2016) and periodic signals corresponding to convective cells advected by the background wind (Spiga 2012)

as polygonal-shaped variations of the surface pressure field of typical amplitude 0.1 Pa. Turbulent wind gusts are associated with both convective vortices and cells (Fig. 11, bottom). Convective vortices are conducive to the formation of dust devils where dust is lifted into and transported by the convective vortex.

In Fig. 12, we adopt the point of view of PS measurements on board InSight and show a typical early-morning temporal evolution of surface pressure simulated by our LES (instantaneous outputs every second, 1 Hz frequency). High-frequency variations of pressure get larger and larger towards late morning as the convective PBL grows deeper and deeper. In a similar fashion as Fig. 11, two phenomena are responsible for the most distinctive high-frequency pressure variations. Convective vortices cause abrupt drops of pressure of a few Pascal during about 100 seconds, while convective cells induce fainter, slower pressure variations of a couple tenths of Pascal, which would imply a periodic signal ("convective heartbeat") as polygonal cells are advected by the background wind (Spiga 2012).

The sampling rate and accuracy of the InSight PS in the continuous data stream (see Sect. 3 and Table 1 in Sect. 4) will ensure the detection of convective vortices passing over the InSight lander. While the sampling rate of the TWINS temperature and wind measure-

ments downlinked continuously to Earth (one every ten seconds) allow in principle to monitor convective vortices, an event-based downlink at the higher frequency of 1 Hz will enable a more in-depth study of a few remarkable convective vortices. As is detailed in Sect. 5, seismic measurements could also enable the detection of convective vortices passing hundreds meters from the InSight lander.

While pressure drops associated with convective vortices have been monitored by all landed missions to Mars equipped with a barometer (Murphy and Nelli 2002; Ringrose et al. 2003; Ellehoj et al. 2010; Kahanpää et al. 2016), the "convective heartbeat" was only observed in terrestrial deserts by high-precision barometers (Lorenz 2012). The high accuracy of the InSight PS barometer (see Sect. 3) should enable the detection of passing convective cells. The "convective heartbeat" should also be detected by InSight seismometers: indeed a quasi-periodic ($\sim$ 5 minutes) signature of the convection pattern can be seen on Mars in the Viking 2 seismometer record, where the body-mounted instrument responded to wind loads on the lander (Lorenz et al. 2017).

Interestingly, InSight's continuously operating PS will also enable to monitor, in a flat plain, the possible occurrence of nighttime pressure drops reminiscent of daytime PBL convective vortices evidenced by the Curiosity lander within Gale Crater (Kahanpää et al. 2016; Ordonez-Etxeberria et al. 2018). This possible nighttime occurrence of convective vortices has not been documented in the Martian LES literature thus far, and would require further modeling work to be accounted for.

The occurrence of convective vortices is not always associated with dust devils—the availability of dust being lifted from the surface is an important constraint. Will the InSight landing site be propitious to dust devils? Reiss and Lorenz (2016) performed a survey of dust devil tracks in the candidate InSight landing region in Elysium Planitia. They found that the detected tracks were predominantly small ($<$ 10 m width) implying small dust-devil vortices. In contrast, track widths at the Gusev site of the MER Spirit measured by Verba et al. (2010), where dust devils were observed in abundance by the MER cameras, had a mean width of some 56 m, even though the Gusev and Elysium sites have similar dust cover (Golombek et al. 2017). Crudely, then, one might expect dust devil activity at InSight to be intermediate between that at Gusev, and that at Gale crater, where no dust devil tracks were observed (and relatively few dust devils have been seen: Moores et al. 2015a; Kahanpää et al. 2016). Reiss and Lorenz (2016) estimated the mean annual formation rate of dust devil tracks to be about 0.05 tracks per square kilometer per sol, which translates in track-forming vortex encounters with a lander to have a recurrence interval of several years, longer than the couple of hundred days encountered by Spirit in Gusev crater. Reiss and Lorenz (2016) also noted that the dust devil tracks in Elysium were rather straight, suggesting that prevailing winds yield a fairly consistent migration of dust devils (akin to the one depicted in Fig. 13), rather than the curved or even cycloidal paths that dust devils in low winds typically generate.

The question of injection of dust particles by PBL turbulence is not limited to convective vortices in dust-devil occurrences; as is illustrated by Fig. 11 (bottom), convective gusts associated with convective cells also cause large departures of friction velocities, hence surface stress. Observed ripple migration in Elysium Planitia indicates a threshold friction velocity for saltation of 0.7 m s^{-1} (Golombek et al. 2018). In Fig. 13, we show the maximum values for friction velocities, as well as statistical distribution, for the whole 2.5 hours simulated in our LES. Our LES for the InSight landing site thereby suggests that, even with a moderate background wind of 5 m s^{-1}, friction velocity larger than 0.7 m s^{-1} might be widespread when the daytime PBL is turbulent from the morning to the afternoon, as a result of both convective vortices (possibly giving rise to dust devils) and convective gusts associated with
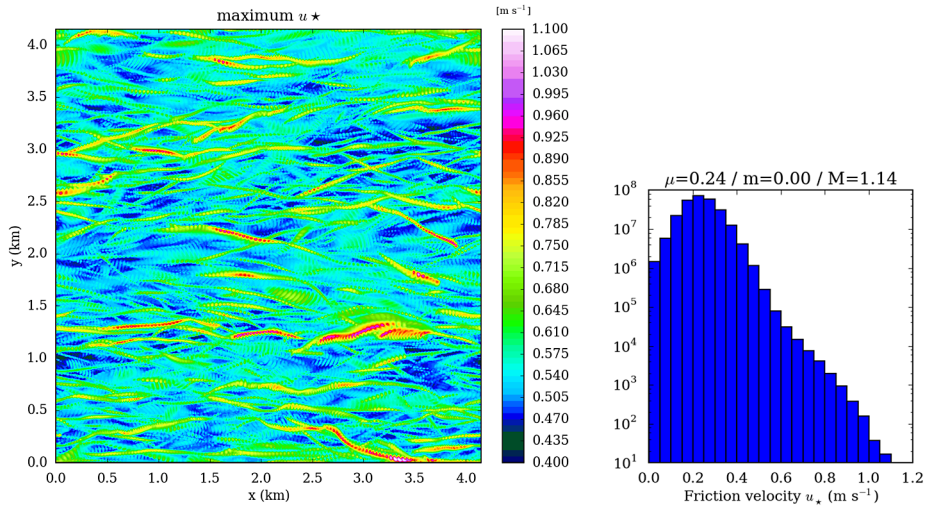
Fig. 13 Results predicted by the 10-m resolution turbulence-resolving LES model. The horizontal map corresponds to the maximum values of friction velocity for each grid point over the 2.5 hours of simulated hours. The areas of high friction velocity correspond to the passage of convective vortices, and would be representative of dust devil tracks shall dust could be mobilized from the surface of Mars in this area. Relatively large friction velocity are also noticed as a result of passing convective cells in the scene. The histogram corresponds to the mapped values: friction velocity associated with turbulence could well exceed the mean value associated with the background wind (Fenton and Michaels 2010; Mulholland et al. 2015; Nishizawa et al. 2016)

convective cells. The aeolian migration of surface structures at the InSight landing site is further discussed in Sect. 6.2.
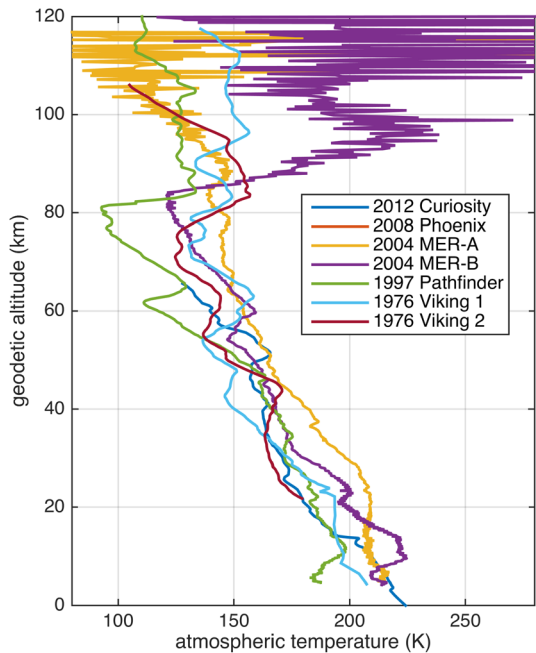
3 InSight Measurements for Atmospheric Science

In this section, we describe all the measurements of interest for carrying out atmospheric science with InSight. The seismic measurements are excluded from this section, since their description requires extended discussions that are developed in Sect. 5.

3.1 Atmospheric Science During Entry Descent Landing (EDL)

The Entry, Descent, Landing (EDL) sequence of Insight offers a rare opportunity to perform *in situ* investigations of the martian environment over a wide altitude range, seized only a few times before by the Viking (Seiff and Kirk 1976; Nier et al. 1976) Pathfinder (Magalhaes et al. 1999) MER Spirit and Opportunity (Withers and Smith 2006) Phoenix (Withers and Catling 2010) Curiosity (Holstein-Rathlou et al. 2016) and Schiaparelli (Ferri et al. 2018) missions. During the EDL, the measured deceleration through the atmosphere leads to the determination of atmospheric profiles along the trajectory as function of altitude with sub-km vertical resolutions (down to hundreds of meters or better Magalhaes et al. 1999) from the surface up to 130 km. The high-resolution sampling of atmospheric structure from surface to thermosphere during EDL complements remote sensing from orbiters, which provide global coverage at lower spatial resolution, orbiter aerobraking measurements, which carry out *in situ* measurements of density and temperature in the upper atmosphere, and lander

Fig. 14 Profiles of temperature acquired during the Entry Descent and Landing phases of previous Martian missions. References for each profile are listed in the text. Local time and season for each profile (Paton et al. 2018) are as follows: (Viking Lander 1) 16:13 $L_s = 97°$, (Viking lander 2) 09:49 $L_s = 121°$, (Pathfinder) 02:56 $L_s = 143°$, (MER A Spirit) 14:16 $L_s = 327°$, (MER B Opportunity) 13:13 $L_s = 339°$, (Phoenix) 16:00 $L_s = 77°$, (Curiosity) 15:00 $L_s = 151°$. Those profiles carry information both on the global climate (e.g. planetary waves, seasonal trends) and on regional-to-local processes (e.g. gravity waves, possibly leading to subcondensation temperatures as is the case for the Pathfinder profile)

measurements, which provide extended time series of high-accuracy measurements at one location. Past examples of such measurements are provided in Fig. 14.

The analysis of accelerations and angular rates recorded by the Inertial Measurement Units (IMU), containing accelerometers and gyroscopes, will enable the reconstruction of the InSight EDL trajectory and the associated atmospheric structure. Given that the carrier vehicle and sensors for InSight's EDL are very similar to the past Phoenix, the InSight EDL reconstruction will be performed with a similar methodology as for the previous Phoenix EDL analysis (Withers and Catling 2010; Blanchard and Desai 2011; Van Hove and Karatekin 2014). In this approach, measurements of vehicle acceleration and velocity are combined with predicted aerodynamic coefficients to reconstruct atmospheric density. Then, pressure and temperature are derived from the reconstructed density along the trajectory as a function of altitude.

The high vertical resolution provided by EDL measurements reveals the atmospheric structure at the time of landing and permits the characterization of a wide variety of atmospheric waves, from large-scale atmospheric tides to small-scale gravity waves (Magalhaes et al. 1999; Withers and Catling 2010; Verba et al. 2010), sometimes inducing atmospheric conditions cold enough to result in the formation of mesospheric CO_2 clouds (Schofield et al. 1997; Holstein-Rathlou et al. 2016), although the location and season of the InSight EDL does not appear to be propitious to the formation of those clouds, from existing observations and models (Määttänen et al. 2010; González-Galindo et al. 2011; Spiga et al. 2012; Sefton-Nash et al. 2013). The new EDL profile obtained with InSight will be a key additional dataset to the existing sparse collection of *in situ* atmospheric profiles, complementary to orbiter and lander meteorological data. Given the $L_s = 295°$ season of landing, propitious to local or global dust storm activity, the InSight EDL profile will provide an interesting complement to the existing dataset obtained at clearer seasons. Notably, the signature of thermal tides is expected to be strongly affected by the reinforcement of the semi-diurnal mode in case of

globally-enhanced dust opacity (Wilson and Hamilton 1996; Lewis and Barker 2005). This signature is expected to be clearly distinguished in the temperature profiles acquired in the upper troposphere and mesosphere during the InSight EDL (Sect. 2). The dusty conditions on Mars during the InSight EDL are also expected to alter the global interhemispheric circulation (Montabone et al. 2005; Kahre et al. 2006), which in turn will impact the temperature and density structure in subtle ways that can nonetheless be interpreted using GCM simulations (Sect. 2). Last but not least, given the emphasis of atmospheric science with InSight on boundary layer processes (Sects. 5 and 6), the assessment of the mixing depth of the convective boundary layer in the final phases of EDL will also be of interest for atmospheric investigations with InSight at the surface of Mars. Imaging of the landing scene, especially of jettisoned hardware during EDL, would also enable to estimate Martian PBL wind speed and directions at the season of landing (Paton et al. 2018).

3.2 Direct Atmospheric Measurements

In this section we describe the direct *in situ* atmospheric measurements that will be carried out by InSight at the surface of Mars. More details on the design and calibration of the described instruments may be found in the reference APSS paper by Banfield et al. (2018). Here, we only describe properties that pertain immediately to science investigations. The meteorological instrumentation on InSight was initially selected to enable the key science goals for InSight: seismic investigation of the planet. However, this does not mean that InSight meteorological investigations will be incremental rather than transformational. For instance, the continuous and high-frequency nature of the APSS observations will provide an unprecedented and more complete catalog of atmospheric phenomena on Mars than previously obtained by landers. With a nearly continuous data set of pressure, air temperature and wind speed and direction, InSight will provide one of the most complete record of meteorological conditions at a Mars landing site, although, contrary to the Curiosity rover, it will not be recording measurements of humidity and UV fluxes, and will not be imaging the sun. Furthermore, the sensitivity of its pressure sensor makes InSight more likely than its predecessors to identify anomalous events.

3.2.1 Temperature and Winds

Temperature and winds will be measured *in situ* by the two TWINS booms which are designed as a repackaged version of the REMS sensors on board the Curiosity rover (Gómez-Elvira et al. 2012). The TWINS booms are located on top of InSight's main deck, at 265 mm from the deck, and about 1.665 m from the Martian ground. The two booms are disposed horizontally, parallel to one another in diametrically opposite directions, facing away from the center of the deck and out over the solar panels. As a result, the two TWINS booms are facing outward on roughly opposite sides of the lander. This deck placement is intended to minimize the effects of wind-flow perturbations induced by the other elements on the lander top deck by ensuring that at least one of the booms will be windward of the bulk of the lander body at all times and wind azimuths (Banfield et al. 2018). TWINS will be operated continuously, using at least one wind sensor and switching between the two booms to maintain the operational boom as the (least perturbed) upwind one, based on the experience of previous sols (Sect. 4) and the expected regular variation of the wind with local time (as shown by previous lander measurements and meteorological modeling, Sect. 2).

It might be difficult to determine which boom shall be switched on at a given local time and season. Indeed, Fig. 11 suggests that, at all seasons, the daytime variability of wind

speed and direction can be very high, as a result of turbulent convection in the PBL. Furthermore, GCM shows that the large-scale and regional wind direction may undergo, at specific seasons, both a strong diurnal cycle (Fig. 8) and a large day-to-day variability, with opposite diurnally-averaged wind directions being predicted from one sol to the next (Fig. 10). Thus, whenever power and data bandwidth constraints allow, both booms shall be operated simultaneously and continuously. Operating the two TWINS booms would enable to characterize the effect of the lander's deck on the observed wind field and to monitor the diurnal cycle of winds with improved quality. The fact that the TWINS booms have a wide sensibility range, extending at an angle $\pm130°$ with respect to their longitudinal axis, mean that the overlapping ranges will make easier both to capture sudden changes in wind direction and to obtain reliable estimates of wind direction and velocity, when the two booms are on.

The two oblong TWINS booms are identical: each carries a wind speed and direction sensor, as well as an air temperature sensor.

– The wind speed and direction sensor consists of three sensor boards (2-dimensional hot film anemometers) arrayed around the tip of each boom, 120° apart from one another. Each of these sensor boards consists of 4 hot dice and 1 cold dice that sense the local wind speed and direction in the plane of the sensor—those are the raw, direct measurements: acquisitions from all the dice are sent back to Earth by InSight. Three-dimensional wind speed and direction measurements are then obtained by differencing measurements first between the hot and cold dice and secondly between the sensor boards facing in different directions. The wind sensor will be sampled at 1 Hz, matching its physical response time of roughly 1 s to wind perturbations. The wind sensor relative accuracy is $\pm15\%$ in the range $1-60$ m s^{-1}. The resolution of the wind measurements is better than 0.4 m s^{-1} in low wind speed and 2 m s^{-1} in high wind speed (details will be provided in a manuscript in preparation, dedicated to InSight / TWINS).
– The temperature sensor acquisition is more straightforward than the wind sensor acquisition. The ambient air temperature is sensed using a small low thermal conductivity rod extending below the base of each boom, which has resistance temperature detectors at its tip and midway along its length. The air temperature sensor will be sampled continuously at 1 Hz, but its physical response time depends on the near-surface turbulence: it is on the order of 30–90 s in forced convection. This sensor performs over the temperature range 167–277 K with an accuracy of about 5 K (given the thermal contamination from the boom and the effects of solar radiation) for a recorded resolution of 0.1 K.

In theory, the TWINS instrumentation will be able to provide vertical wind speed. It is however likely that this quantity will not be useful for meteorological analysis, given the low height of the TWINS sensors with respect to the deck, and the proximity of the solar panels and other surrounding elements (Banfield et al. 2018). Those factors jeopardizing the measurements of vertical wind speed also impact, albeit to a lesser extent, horizontal wind measurements. The level of uncertainty on the measurements of horizontal wind speed and direction could be mitigated by using, for turbulent conditions, Computational Fluid Dynamics (CFD) simulations of the interaction of ambient wind with InSight lander's deck elements, and, for laminar conditions, calibration in a large wind tunnel using a mock-up of the InSight lander. More details on those CFD simulations will be described in a dedicated paper.

The primary goal of the TWINS measurements is to provide a framework to assess the degradation of the SEIS signal-to-noise ratio when wind perturbations are significant (typically above 5 m s^{-1}, Mimoun et al. 2017; Murdoch et al. 2017a; Lognonné et al. 2018, see also Sect. 5). This is why TWINS will be run continuously, recording data with no gaps and

at a high enough sampling rate to assist SEIS data analysis. Wind measurements will also be used during the deployment phase of SEIS and HP³ (see Sect. 4) to establish the safest location and time of day to perform this operation.

Nonetheless, measuring wind and temperature by TWINS will be also used to address pure atmospheric science goals. As can be inferred from existing modeling mentioned in Sect. 2, wind and temperature measurements at the surface of Mars will help to characterize the properties and seasonal variability of both the local meteorology in Elysium Planitia (boundary layer turbulence—including convective vortices, mesoscale waves, slope winds, dust storms) and the global atmospheric phenomena on Mars (thermal tides, planetary waves, planet-encircling dust events). At any event, the TWINS measurements will improve over REMS measurements on board Curiosity: one of the two REMS booms was dysfunctional / damaged since landing and made the reliability of the wind measurements more difficult to obtain, requiring a careful selection of the measurements of the functional boom as a function of wind direction (Gómez-Elvira et al. 2014; Haberle et al. 2014), or dedicated campaigns in which Curiosity was oriented in multiples directions over a couple of sols to mitigate this issue (Newman et al. 2017). Furthermore, the fact that TWINS will be running continuously is a unique capability of the InSight mission. This surpasses previous landed missions on Mars which had gaps in the meteorological coverage (Chamberlain et al. 1976; Seiff et al. 1997; Davy et al. 2010; Gómez-Elvira et al. 2014). Continuous sampling of winds and temperature will enable for instance to monitor the temporal variability of atmospheric turbulence, to follow the seasonal evolution of regular atmospheric phenomena, and to quantify wind thresholds (i.e., peak winds) for dust lifting—either from the surface or from solar panels—and aeolian surface change (Sect. 6).

3.2.2 Surface Pressure

The pressure sensor (PS) is a highly-sensitive pressure transducer located within the lander, in the relative protection of the electronics box. It is a Tavis pressure sensor, an improved version of those used on the Viking and Pathfinder missions (Hess et al. 1980; Schofield et al. 1997). It communicates with the ambient atmosphere through an inlet tubing that opens to the outside air near the center of the lander deck, at the stowage point for the WTS that is to be deployed by the IDA to protect the SEIS instrumentation once it is placed on the Mars' surface.

Contrary to the pressure sensors previously sent to Mars, the pressure inlet on board In-Sight is specifically designed to minimize the effects of wind on the pressure measurements (with a design similar to the "Quad-Disc" design developed for single inlet micro-barometric (infrasound) measurements on Earth, see Banfield et al. 2018, for further details). Under terrestrial conditions, the Quad-Disc inlets reduce wind-induced "dynamic pressure" fluctuations on pressure measurements to a range of 1 to 0.01% of the measured absolute pressure, the latter (best) performance being obtained for in low Reynolds number conditions. Given that the Reynolds number is about 2 orders of magnitude smaller on Mars than on Earth (Larsen et al. 2002; Petrosyan et al. 2011), the wind-induced pressure effects should be reduced by Quad-disc to values as low as 0.0001% of the measured absolute pressure. This translates to a 0.6 mPa dynamic pressure perturbation for the mean surface pressure at the surface of Mars (610 Pa). However, this estimate has not been confirmed by experimental studies (Banfield et al. 2018). Before WTS deployment, the PS sensitivity to winds will be larger, although still useful for most meteorological measurements (typically < 1 Pa for $7 \, \text{m s}^{-1}$ winds).

The PS is designed to produce valid output between pressures of about 560 Pa and 1000 Pa, which are expected to be the extreme pressures that will be experienced at the

InSight landing site (see Sect. 2). This range might be subject to change since the actual calibration of the PS is temperature-dependent, although this is mitigated by the PS position within the body of the lander in a relatively controlled thermal environment less likely to lead to significant spurious dynamic pressure effects. This temperature dependency is also mitigated by the inclusion of a temperature sensor near the PS active elements, required to calibrate the voltage readings to the measured environmental pressure.

The pressure sensor itself is designed with the objective of low-noise performance, with baseline root-mean-square (RMS) of ~ 10 mPa on any particular reading. The InSight mission requirements for the noise spectrum $\mathcal{N}$ of the instrument is

$$\mathcal{N} = \frac{10}{(10f)^{2/3}} \text{ mPa Hz}^{-1/2}$$

at lower frequencies ($10^{-2} < f < 10^{-1}$ Hz) and $\mathcal{N} = 10$ mPa Hz$^{-1/2}$ at higher frequencies ($10^{-1} < f < 1$ Hz) (Murdoch et al. 2017a; Lognonné et al. 2018). According to calibration studies, the PS meets this requirement for the high-frequency range and is one order-of-magnitude better in the lower-frequency range (Banfield et al. 2018). The sensitivity of the PS is better by roughly a factor of 20 than previous pressure acquisitions at the surface of Mars (Chamberlain et al. 1976; Schofield et al. 1997; Taylor et al. 2008; Harri et al. 2014). The InSight PS will be sampled at continuously 20 Hz, a sampling one order of magnitude higher than its predecessors (e.g. Curiosity REMS logs pressure at only 1 Hz and Viking typically sampled pressure at 0.25 Hz with some sequences at 0.5–1 Hz), with a response time of at least several Hz—about 6 Hz due to the inlet plumbing of the pressure sensor and 3 Hz due to the first-order electrical low pass filter on the sensor output. The absolute calibration of the PS, as well as the estimate of its temporal drift, are yet to be completed at the time of writing (see Sect. 6.3 for a discussion of possible scientific applications).

Like the TWINS instrumentation, the PS instrument will enable to assess the level of seismic "noise" caused by atmospheric variations (Mimoun et al. 2017). However, contrary to TWINS, the characteristics of the PS instrument (high frequency, high accuracy) shall enable to perform "pressure decorrelation" (Murdoch et al. 2017a, see also Sect. 5), i.e. decorrelate the atmosphere-induced pressure signal from the seismic signal to improve the quality of the detection of seismic events, one of InSight's main science goals.

Moreover, the unprecedented level of precision and sampling of the InSight PS, as well as the fact that the instrument will be continuously sampling pressure contrary to previous instruments, will open many possibilities:

– on the one hand, to provide a much more complete view on the statistics of dust devil events (Kenda et al. 2017), on the seasonal behaviour of thermal tides (Guzewich et al. 2016), on the variety of planetary-scale waves (the less sensitive Curiosity pressure sensor was able to detect close to the equator the signal of mid-latitude baroclinic waves Haberle et al. 2018) or mesoscale waves such as gravity waves that can be detected by a high-precision pressure sensor (Gossard and Munk 1954, see also Sect. 5);
– on the other hand, to detect infrasound signatures from bolide impacts (Garcia et al. 2017; Stevanović et al. 2017, and see Sect. 5.2.3), from remote dust-devil-like vortices (Lorenz and Christie 2015), or other events not detected thus far (see Sect. 4 for discussions on the specific event-driven approach of the InSight mission).

3.3 Other Measurements of Interest for Atmospheric Science on Mars

3.3.1 Surface Temperature

Surface temperature is a key quantity in both weather and climate science. The knowledge of surface temperature at a given landing site is crucial to caracterize the diurnal cycle of the PBL and, more generally, the heat exchanges between the surface and the atmosphere (more details on this topic are provided in Sect. 6.1).

The HP[3] infrared radiometer RAD will acquire surface brightness temperatures (using three bandpass filters with transmission in the 8–10 μm, 8–14 μm, and 15–19 μm wavelength ranges, Spohn et al. 2018) with an uncertainty of better than 4 K in two fields of view opposite of the workspace (where SEIS and HP[3] will be deployed), continuously four times per sol for the entire duration of the mission—and hourly in the early deployment phase (see Sect. 4). In addition to the nominal RAD modes, single observations for a specific science campaign could also be envisioned: in the standard mode, the radiometer warms up to one of the calibration points, equilibrates for 1 hour, then acquires 20 samples over 5 min; adjustment of those durations and rates is available for more flexibility on the local time of acquisition. This could allow for up to 12 observations per sol.

RAD infrared measurements can provide surface temperature with an assumption on the surface emissivity. Surface emissivity of Martian regolith at the bands of the radiometer is expected to show little variability (0.97 ± 0.02) based on remote and in-situ data (Morgan et al. 2018). A bandpass filter aimed at the derivation of atmospheric temperatures (as was used by REMS GTS, Gómez-Elvira et al. 2012) was considered for the HP[3] radiometer, but was not selected because the expected optical path of about 4 m for the outlying field of view is too short to create an atmospheric contribution to the signal above the noise level. The measurements of the selected bandpasses are expected to have negligible contributions from CO_2 absorption lines and airborne dust. The Mini-TES instrument observed some variation of surface brightness temperature, which Ruff et al. (2006) interpret as a result of optically thin dust on the surface that is thermally coupled to the atmosphere, but even this effect is small compared to the instrumental uncertainty.

3.3.2 Dust Opacity

Measuring atmospheric dust opacity *in situ* is a key asset of a landing mission, of particular interest not only to the mission's operations (especially power management), but also as a crucial input for surface energy balance computations (Plesa et al. 2016) and climate modeling (Kahre et al. 2006; Montabone et al. 2015), given the key radiative forcing imposed by suspended dust in the atmosphere of Mars (Madeleine et al. 2011). The expected seasonal variations of the atmospheric dust opacity at the InSight landing site are shown in Fig. 4 in Sect. 2.

Because the InSight mission is solar powered, and thus power availability is dependent on intensity of the sunlight received on its solar panels, InSight will use its arm-mounted IDC to determine the atmospheric opacity (related to both dust and water ice particles). The IDC is a narrow-angle color camera (Maki et al. 2018), a flight spare Navcam from the MSL/Curiosity mission, similar to the model on board the MERs, and upgraded with a Bayer color filter array detector. The second camera (ICC) is a wide-angle color camera, also a flight spare from Curiosity (Hazcam) with filter upgrading, that is fixed to the lander to provide imaging during the deployment phase. The ICC could serve as a complement to IDC for monitoring dust optical depth.

Monitoring of atmospheric opacity will allow variations in solar panel output to be attributed to either atmospheric events (transient storms, seasonal variations) or some form of panel degradation (e.g., dust accumulation on the panels). The opacity record will also be available as a measurement of a key meteorological parameter: the opacity is dominated by atmospheric dust (a key control on the climate of Mars), and the variations in dust opacity represent both the effects of weather (e.g. Cantor 2007; Cantor et al. 2010) as well as the causes of variations in energy fluxes into the surface and atmosphere (Lemmon et al. 2015; Plesa et al. 2016).

While previous landed missions have used direct solar imaging to determine atmospheric opacity via the Beer-Lambert-Bougher extinction law (Colburn et al. 1989; Smith and Lemmon 1999; Lemmon et al. 2004, 2015), InSight does not possess a camera with a solar filter. Furthermore, for much of the InSight mission, there is no plan to move cameras: the ICC is fixed, and the IDC will be left *a priori* in a fixed position after deployment. Thus, atmospheric opacity must be derived from non-solar images, and the plan is to use images of the Martian sky. Both cameras can image some part of the sky. The arm-mounted IDC has a 45-degree FOV (Maki et al. 2018) and will likely be left aimed near the southern horizon after the completion of arm-related activities. The body-mounted ICC includes sky above the workspace and the horizon in its 124-degree field-of-view (the Martian sky would approximately occupy one fifth of the field-of-view, hence about 20-25 degrees elevation). Both cameras are modified from their MER and MSL counterparts by swapping the bandpass filter for red, green, and blue microfilters in a pattern over the detector pixels.

Determining atmospheric dust opacity from a sky image depends on several factors. The distribution of opacity in the sky must be relatively uniform and, in the absence of discrete cirrus clouds, has been shown to typically be uniform to 5% at MER sites (Lemmon et al. 2015). The dust scattering properties must be relatively well known; somewhat consistent measurements have been obtained from Viking (Pollack et al. 1995), Pathfinder (Tomasko et al. 1999), and Spirit and Opportunity (Lemmon et al. 2004). The sky radiance must be able to be derived from images; this is typically a function of camera calibration, but the task is hindered by dust accumulation on the camera itself (Lemmon et al. 2015). This dust deposition could be, however, estimated from atmospheric dust opacity measurements as was done for other landers and rovers at the surface of Mars (Smith et al. 2006; Golombek et al. 2018). Furthermore, the selection of the InSight landing site factored in in the dustiness of the site which would correlate with dust accumulation on solar panels (Golombek et al. 2017). Perfect knowledge of these factors would enable many successful strategies to retrieve atmospheric dust opacity from images.

Due to imperfect knowledge of these parameters, an observation campaign was implemented on the Opportunity rover over one Mars year, and is described in Wolfe (2016) and presented in summary here. In the afternoon and evening, sky imaging was obtained contemporaneously with atmospheric dust opacity via direct solar imaging. The sky brightness gradient $d \ln I / dz$, where I is radiance and z is elevation angle, was obtained from the images. A preliminary investigation had shown, via radiative transfer modeling, that if that parameter is used for a retrieval, accurate dust opacity could be retrieved without knowing the camera calibration (and by extension, even if the calibration were variable with time) with, furthermore, reasonable errors in the model of the scattering phase function of the atmospheric dust.

At the end of one Mars year of observations (sols 3579–4248, from 27 January 2014 to 15 December 2015), the data were analyzed. During this time, the Opportunity Pancams had time-varying coatings of over one half an optical depth of dust, down from a peak over one optical depth (Lemmon et al. 2015). The Navcams, adjacent to the Pancams, likely had similar coatings, and this was consistent with features in sky and terrain images. Discrete clouds

appeared on several sols, and were significant enough to jeopardize the observation in one case. The observations through Martian aphelion season likely included ice hazes with the dust (Lemmon et al. 2015; Montabone et al. 2015). Despite this, the observations achieved a RMS error with respect to Pancam of 0.124. Given an intrinsic Pancam uncertainty of 0.058 during that time frame, Wolfe (2016) estimated the dust optical depth uncertainty from the sky-imaging procedure as 0.084.

For InSight operations, the nominal procedure for optical depth imaging will be to use compressed IDC images that require a downlink volume of < 1 Mb per image and include sky at a scattering angle near 90 degrees from the Sun and at elevation angles of 20–30 degrees. The nominal downlink volume is 97.5% subscribed without imaging to give priority to SEIS and HP^3 measurements; this enables at least for one optical depth imaging per week in the nominal conditions. Should additional downlink be available, up to daily images are possible. The images will be processed as part of the standard image product pipeline, with a flag set in the image command to trigger opacity analysis. The procedure is expected to yield dust optical depths to an accuracy of about 0.1, with a likely cadence of weekly (or more infrequently). The red channels of the IDC and ICC are similar to the bandpass of the MER Navcam, in that the expected wavelength variations are smaller than the range of parameter variations considered by Wolfe (2016). The green and blue channels are expected to add constraints about the dust/ice opacity ratio, as shown by previous work e.g. Moores et al. (2010).

Dust devils have also been detected by direct imaging (Metzger et al. 1999; Ferri et al. 2003; Greeley et al. 2006; Ellehoj et al. 2010; Greeley et al. 2010). Imaging adds the ability to characterize the dust content of dust devils, and their contribution to the atmospheric dust load. In addition, imaging can also constrain the position and track of the dust devil, for validation of the inferences based on meteorological parameters (Sect. 5.2.2). Short series of images using MER and MSL Navcams and Hazcams have been used to detect dust devils, measure their position, velocity, rotation, and dust load (Greeley et al. 2010). While such images are possible, they may be rare due to downlink constraints (see previous paragraph), as an image sequence requires ~ 1 Mb per lossless, subframed image. However, lossy compression can reduce that by a factor of $2 - 4$ while still allowing detection of dust devils.

3.3.3 Atmosphere Angular Momentum

The InSight radio science experiment, RISE, is expected to significantly improve the current knowledge of Mars rotation parameters. The Doppler measurements by RISE will be used to determine both the variation of the rotation rate Ω, expressed as variations of the Length-Of-Day (LOD), and the orientation of the spin-axis of Mars in space (the long-term precession and periodic nutations). Besides providing insights on the interior structure of Mars, these data also enable the investigation of atmospheric angular momentum (AAM) variations of Mars (see Karatekin et al. 2017) to study the physical processes explaining the seasonal momentum variations of the Martian atmosphere and the sublimation/condensation cycle of atmospheric CO_2.

Angular momentum exchanges between the surface and the atmosphere alter the planetary rotation, causing variations on the order of tens of milliseconds in Martian LOD over seasonal time scales (Karatekin et al. 2011). The AAM variations of a planet are associated with the global atmospheric mass redistribution $\mathcal{M}_m$ and the wind variability $\mathcal{M}_w$

$$\mathcal{M} = \mathcal{M}_m + \mathcal{M}_w = \int_V \Omega a^2 \cos^2 \varphi \, dm + \int_V u a \cos \varphi \, dm,$$

where a is the radius of the planet, u is the zonal wind (i.e. in the east-west direction), dm is an element of atmospheric mass, φ is latitude, and $\int_V$ integration over the volume of the atmosphere. On the Earth, the largest contribution to the AAM variability comes from the annual excitation caused by the monsoon regime and the seasonal variations of zonal winds (Karatekin et al. 2011). Conversely, AAM variability of Mars is mainly due to the surface mass redistribution over seasonal time scales caused by the CO_2 condensation / sublimation cycle at the polar caps. For both the Earth and Mars, the diurnal angular momentum variations are much smaller compared to the seasonal variation scales.

Current knowledge on the dynamics of the Martian atmosphere is limited by the lack of continuous global observations of dynamical variables with a good temporal and spatial resolution. LOD variations predicted by GCM show differences at the 0.05 milli-second (msec) level, mainly due to differences in their implemented physical models (Konopliv et al. 2011; Karatekin et al. 2017). Although the changes in the rotation of Mars have been observed since the Viking era by the radio tracking of surface landers (Folkner et al. 1997; Kuchynka et al. 2014) and orbiting spacecraft (e.g., Konopliv et al. 2011), the present knowledge of LOD is not sufficient to go further than the current discrepancy between GCMs and to constrain Mars' CO_2 cycle or winds (Karatekin and Montabone 2014). Furthermore, the accuracy of observations is not high enough to enable the determination of the inter-annual LOD variability.

Folkner et al. (2018, this issue) have predicted the precision with which the amplitudes of the rotation angle variation of Mars will be determined by RISE on board InSight. RISE will estimate ΔLOD within 0.012 msec of uncertainty. This is more than one order of magnitude better than the estimates from Viking and Pathfinder landers, and better than the 0.05 msec precision required to distinguish among competing GCMs simulating the dynamics of the Martian atmosphere. Moreover, assuming an extension of the InSight mission, or relying on the arrival of LaRa (a similar radio-science instrument onboard ExoMars 2020 with similar sensitivity to ΔLOD, see Dehant et al. 2009, 2011; Le Maistre et al. 2012), ΔLOD would be estimated with an uncertainty reduced by a factor of two (down to 0.005 msec). Such long-standing operations from the surface might also reveal the inter-annual variations of the global-scale CO_2 cycle that could arise from the dust storm inter-annual variability (Montabone et al. 2015, see also Fig. 4). The fact that the InSight mission features an unprecedented high-precision pressure sensor, also capable to monitor the surface pressure variations induced by Mars' CO_2 cycle, makes RISE on board InSight all the more promising.

4 Operational Aspects

4.1 Operations and Event Classification

Following launch in May 2018, and a 7-month cruise before landing in November 26th 2018 (Banerdt et al. 2018), the operations of the Insight mission are split into two major phases:

1. In the 60-sol "deployment" phase, the InSight mission system is deployed on the surface of Mars by the IDA (especially the SEIS/WTS and HP^3 systems) and calibrated. The tactical timeline of the deployment phase is built according to engineering constraints, and could be modified from one day to the other. During this phase, the east X-band antenna will be used directly for uplink from Earth to lander. Most of the InSight system will not be operational, but APSS measurements will start shortly after landing (close to

sol 4). Notably, the two TWINS booms will be operating during this phase to characterize the diurnal wind cycle and to support the activities to place SEIS/WTS and HP[3] at the surface of Mars; this early acquisition will also help to reflect on the boom-switching strategy (see Sect. 3, and below).

2. In the "science monitoring" phase, starting after SEIS and HP[3] have been deployed on the surface, the science measurements and operations are carried out on the basis of a weekly timeline cycle, with planning from one week to the other to allow for the recovering of the most interesting science acquisitions given the limited bandwidth. This means that, contrary to the rapid strategic turnaround time during the deployment phase, the strategic sequences for the lander, comprising a set of sequences to be executed at predefined moments at least twice per sol, are uplinked from Earth to the lander only once per week. Uplink is performed via relay orbiters; downlink from the lander to Earth is performed via relay[3] through either MRO or ODY with two passes a day (typically twice per day at 3 AM and 6 PM local mean solar time), with an expected average downlink rate > 90 Mbits per sol. The expected average downlink rate considered for planning purposes for SEIS / APSS measurements is 38 Mbits per sol.

Science operations planning is less complex for InSight than for previous Mars landers: most of the InSight payload is not interactive. Being solar-powered, hence prone to energy limitations, the lander spends the majority of the science monitoring operations asleep, with only the payload continuously powered to collect data. The InSight lander only wakes up every three hours for battery, safety, housekeeping diagnostics. Data are collected, processed from the instruments, and sent to Earth through relay orbiters during two of those daily wake cycles. During the science monitoring operations, SEIS, HP[3], and APSS/TWINS are in nominal data collection mode, i.e. data are automatically and continuously stored at high sampling rate (see Table 1) in the lander mass memory for about 6 weeks. Two notable exceptions are

– The active TWINS' boom is planned to be swapped, at least twice per sol, to account for changing wind direction based on the measurements carried out on previous sols and meteorological modeling (see Sect. 2.2)—unless power and data bandwidth constraints allow for the continuous operation of the two TWINS booms at the same time, which will highly improve the quality of wind measurements (Sect. 3).

– The radiometer in HP[3] (Spohn et al. 2018) will take routinely four measurements during each sol for five minutes duration each (approximate planned local times: 2 AM+PM and 5 AM+PM), and every 15° L_s (29 sols), possibly complemented by measurement campaigns during an entire sol with one measurement per hour, each on a five-minute duration.

In case of low power availability—e.g. in high dust loading in the atmosphere during a dust storm or when heater consumption is larger in the cold season, individual instruments could be powered off to give priority to the operations essential for the survival of the lander. The worst-case upper limit for reduced instrument activity is 180 sols (Banerdt et al. 2018).

The limited available bandwidth for the InSight mission implies that the full high-frequency measurements cannot be retrieved on Earth: SEIS and APSS data will generate about 600 Mbits per sol, while the nominal downlink rate is 38 Mbits per sol. Combined to the seismology-driven focus of the InSight mission, this entails an operational approach where science teams perform data selection based on notable events. "Continuous data" at

---

[3]The X-band antenna can still be used in case the relay with orbiters is not functional, but the rate is much slower.

Table 1 List of the sampling rates for each instrument of the InSight SEIS and APSS instrumental suites. Additional details can be found in the papers in this special issue discussing the InSight mission (Banerdt et al. 2018), SEIS (Lognonné et al. 2018) and APSS (Banfield et al. 2018). While the down-sampled data is continuously sent to Earth, the raw data is only downlinked based on event requests (see text). The down-sampling rates are based on a nominal downlink rate of 38 Mbits per sol for SEIS and APSS. Note that, assuming no improvement on the nominal data rate, the value of the TWINS down-sampling rate might be lowered in cases where the two booms are switched on continuously to improve the quality of wind measurements (Sect. 3). The available downlink rate for SEIS and APSS event data is still to be determined at the time of writing; it will be typically about 5 Mbits per sol of SEIS + APSS event data, with an additional 2–3 Mbits per sol for APSS-only events

Instrument	Full sampling rate *Raw "event" data*	Down-sampling rate *Continuous data*
SEIS SP	100 Hz	10 Hz (hybrid with VBB)
SEIS VBB (velocity)	20 Hz	2 Hz
APSS PS	20 Hz	2 Hz
APSS IFG	20 Hz	0.2 Hz
APSS TWINS	1 Hz	0.1 Hz

lower sampling rate are being recovered and continuously sent back to Earth, in order to detect the events of interest for which the complete high-frequency data ("event data") shall be downlinked to Earth (see Table 1). The event data are prioritized in seven buffers of increasing levels of priority and retrieved accordingly given their priority determined by the science teams. A typical example of an event of prior interest is the occurrence of seismic signals associated with marsquakes (selected by the so-called Mars Quake Service Clinton et al. 2017; Panning et al. 2017). In this case, high-frequency wind data will also be downlinked to Earth to discriminate unambiguously this signal from a wind-induced effect, as well as pressure data to enable some level of pressure decorrelation (see Sect. 5). Data prioritization activities, and the associated building of the set of event requests for the downlink of related high-frequency data, will be made weekly, following the above-mentioned uplink strategy.

It shall be emphasized that an event request is not intended to be necessarily related to a quake or any other event associated with the activity in the interior of Mars. This is especially true for atmospheric phenomena that, as is detailed in Sect. 5, are likely to resemble seismic events since they induce a seismic signature likely to be detected by SEIS: convective vortices, gravity waves, wind gusts. With this potential goal of atmospheric science in mind, InSight on-board processing will not only downsample the pressure records to a lower sampling rate (2 Hz) for the continuous data stream, but it will also provide in this stream the energy in the pressure signal at frequencies above the continuously downlinked sampling rate, namely the RMS of a high-pass version of the pressure signal above 1 Hz (downsampled to 0.5 Hz) as a rough indication of high-frequency pressure variations. TWINS' air temperature continuous dataset will also include, in addition to temperature data downsampled to 0.1 Hz, the standard deviation over the averaging time for downsampling; however, wind measurements will not feature this complex filtering process.

In some situations, particularly so at the beginning of the InSight mission, anomalous signals detected in the pressure or seismic or wind or magnetic records will be enough to justify an event request for downlink high-frequency data—with potential interest for atmospheric science in case the event turns out to be of atmospheric origin. In this case, if the duration of this anomalous signal is short, e.g. the full 20-Hz PS dataset can be downlinked only for a brief amount of time, for instance during half a Martian hour. We cannot fully anticipate what the meteorological investigations on InSight will reveal. The continuous data

set may turn up new (rare) phenomena, or characterize expected ones in greater detail. The much greater sensitivity of the pressure sensor may reveal a wealth of infrasound sources. The observational strategy for meteorological data acquisition on InSight is thus designed with the possibility of serendipity and the unexpected in mind.

How to classify events and distinguish between seismic events? Making the distinction between a real seismic event and vibration generated by the impact of the wind on a seismic instrument is more than a theoretical issue. As a matter of fact, the seismometer experiment on-board the Viking lander recorded wind-induced noise (Anderson et al. 1977; Nakamura and Anderson 1979; Lorenz et al. 2017). The Viking lander platform, where the seismometer was located, was moved by the lift and drag forces resulting from the wind (Lognonné and Mosser 1993) and, as a result of this, most of the signal recorded was dominated by the wind-induced lander vibration (Goins and Lazarewicz 1979). Insight SEIS will not be directly moved by the platform motion under the wind, as it will be deployed on the Martian ground by a robotic arm, and protected from the wind by the WTS. Once a candidate seismic signal is detected, a potential wind event counterpart is looked for. Contrarily to other auxiliary sensors on-board Insight, such as the PS or IFG data, the TWINS wind data are not used to be de-correlated from the seismic data, but rather act as an indicator of the existence of a wind perturbation. Microbarometer PS data will be also be investigated to detect possible passage of dust devils or other wind vortices's during the candidate seismic event.

Last but not least, a difficulty that is specific to the atmospheric science part of the InSight mission is the fact that not all meteorological phenomena can be classified as events in the seismic sense. This is typically the case for any diurnally- and seasonally-varying atmospheric phenomena developing on a regional-to-global scale such as dust storms, planetary waves (e.g., thermal tides, baroclinic waves), cloud activity. This is why the original event-driven approach, entailed by the main geophysical goals of the InSight mission—and the seismic measurements of possible marsquakes—will be complemented with Non-Event Meteorological Observations (NEMOs) to provide the community with meteorological datasets as extended as possible. NEMOs are meant to be obtained by analyzing the continuous data (which is the obvious dataset to study NEMOs), but also by submitting event request not related to any specific seismic signature. For instance, a request for the high-frequency pressure, wind and temperature data during a couple hundreds of seconds could be justified by the need to explore e.g. daytime turbulent convection, or an episode of very windy nighttime conditions. This is also why the Mars Quake Service (Clinton et al. 2018) will be complemented by a Mars Weather Service analyzing the APSS observations in a broader sense than the approach driven by seismic events. To further reach this goal to monitor NEMOs, opacity measurements will be carried out with cameras and the use of InSight's arm, as is described in Sect. 3.3.2.

4.2 InSight Performance Related to Atmospheric Parameters

The purpose of the SEIS instrument is to measure the surface ground velocity by a set of 3-axis seismometers covering the 0.01–10 Hz frequency bandwidth for the Very Broad Band (VBB) sensors and 0.1–50 Hz for the Short Period (SP) sensors (see Lognonné et al. 2018, for more details). To fulfill the InSight major science goals to characterize Mars' internal activity, given the two strong constraints of single-station geophysical measurements and putatively low seismic activity on Mars, the SEIS instrument must comply with a very low instrument noise level: $\sim 10^{-9}$ m s^{-2} Hz$^{-1/2}$ in the bandwidth 0.01 to 1 Hz and $\sim 10^{-8}$ m s^{-2} Hz$^{-1/2}$ in the bandwidth 1 to 10 Hz.

As a consequence of the high level of performance required from the Insight seismometer, most of the environmental parameters have an impact on the seismic performance. A major point that has to be acknowledged is the fact that the Insight seismometer is deployed on the ground (with an expected low rigidity of the Martian upper subsurface) and not protected in a vault as for terrestrial sensors. Atmospheric parameters may have therefore a dominant contribution in the noise budget of the deployed seismometer. Although considerably smaller than those reported by the Viking experiment (Anderson et al. 1977; Nakamura and Anderson 1979), noise variations will likely be observed in the range comparable with the instrument noise level.

The complete identification and evaluation of the noise model for SEIS is detailed in Mimoun et al. (2017) (see also Murdoch et al. 2017a,b; Kenda et al. 2017; Murdoch et al. 2018, and Sect. 5). To summarize, the InSight noise contributors can be categorized along the following items: parameters affecting the instrument self-noise, environmental effects generating noise in the instrument, and environmental effects generating ground acceleration. According to this classification, we can identify respectively the atmospheric temperature, wind and pressure variations as environmental parameters with an impact on the seismic experiment performance.

1. *Temperature* Mars' atmospheric temperature is probably one of the key sizing parameters of the seismometer. Although partially filtered by the SEIS thermal protection (WTS), the expected 80-K daily variation of air temperature impacts the instrument self-noise, though thermal sensitivity and thermoelastic, but also the dynamics of the output of the instrument (Mimoun et al. 2017). Typical diurnal temperature variations are expected to be about 10 K in winter and 22 K in summer at the VBBs sensor location, with larger temperature variations on the SPs (Lognonné et al. 2018).
2. *Winds* The wind was the main contributor to the seismic signal recorded by the Viking experiment (Anderson et al. 1977; Lorenz et al. 2017). It will impact the instrument through the WTS (even if SEIS is mechanically decoupled from the lander), and through vibrational motion of the lander that can be felt by the seismometer (Murdoch et al. 2017b).
3. *Pressure* The idea that pressure-induced tilt noise (ground acceleration) may be the main source of Martian seismic noise has been first proposed by Lognonné and Mosser (1993). To do so, they relied on the Sorrells (1971) theory which assumes that the atmospheric pressure field can be decomposed as sinusoidal pressure waves (see Sect. 5 for a more detailed discussion on atmosphere-induced seismic noise). A similar framework was used in Murdoch et al. (2017a) and Kenda et al. (2017) to estimate the pressure tilt noise—which is the sizing noise in terms of amplitude.

These environmental contributors change continuously. During the night, the wind and pressure variations as well as the turbulence, will be weaker (Sect. 2). At night, lower environment noise is thus expected, and small events may be more easily detected. Conversely, during the day, or in case strong dust storms occur, a more vigorous turbulence or large winds could dwarf small signals (Mimoun et al. 2017). Although part of this noise is expected to be decorrelated by the APSS sensors, the non-seismic origin of that part of the recorded noise will have to be considered in all noise analysis. At the same time, the seismic "noise" induced by atmospheric phenomena could be regarded as a signal for atmospheric science, which could provide a diagnostic for atmospheric activity (see Sect. 5).

4.3 Coordinated Campaigns with Orbiters

InSight is planning a coordinated campaign with various orbiting cameras to accomplish synergistic science combining orbital images and InSight data from the ground (see Daubar et al. 2018, for more details). Specifically, the High Resolution Imaging Science Experiment (HiRISE) on NASA's MRO (McEwen et al. 2007) has 25 cm/pixel color imaging capability with excellent signal-to-noise ratio.

Firstly, this has made HiRISE very helpful in monitoring dust devil tracks and their variability with season (Verba et al. 2010; Statella et al. 2012). HiRISE images show dust devil tracks throughout the InSight landing site (Golombek et al. 2017). Although the odds of imaging a dust devil itself are low, multiple periodic HiRISE images are expected to be requested for monitoring of the landing site (Golombek et al. 2018), increasing the chances of catching one. If an image captures a dust devil, HiRISE might have the unique capability to measure dust devil tangential speeds (Choi and Dundas 2011) and translation velocity (Reiss et al. 2014), some of which could also be inferred from InSight measurements (Sect. 5.2.2), in addition to the pressure perturbations and seismic signals caused by the convective vortex creating the dust devil.

Secondly, HiRISE images will allow the monitoring of decameter-scale aeolian surface processes such as the formation / modification of wind streaks, superficial dust motions as evidenced by albedo changes, or possible bedform motions (Bridges et al. 2012, and see Sect. 6). Other possible atmospheric-related investigations that would benefit from orbital images include the very high resolution Digital Terrain Model available around the InSight landing site, that, for instance, could be used in LES modeling of atmospheric turbulence (Sect. 2.3).

The Context camera (CTX) on MRO (6 m/pixel) (Malin et al. 2007) and the Colour and Stereo Surface Imaging System (CaSSIS) on the European Space Agency (ESA) ExoMars Trace Gas Orbiter (TGO) (Thomas et al. 2017) will also be valuable for regional context imaging. CTX support images will be requested for each HiRISE image, giving a contextual view to any phenomena seen in the high-resolution images. CaSSIS returns color and stereo images of Mars at 5 m per pixel, but its limited ability to point off-nadir (Thomas et al. 2017) will make it difficult to acquire targeted observations of any particular spot, such as the location of the InSight lander. Both of these could monitor regional atmospheric dust opacity and cloud activity for comparison with InSight's ground-based local observations. The use of the OMEGA imaging spectrometer (Bibring et al. 2004; Bellucci et al. 2006) and the High-Resolution Stereo Camera (HRSC Jaumann et al. 2007) on board the still-operating MEx spacecraft could also provide further constraints on the dust storm activity (Määttänen et al. 2009) and the variability of cloud cover (Madeleine et al. 2012) in the Elysium region. Imaging by the MRO / MARCI (Malin et al. 2008) will also prove useful for monitoring atmospheric activity in the InSight region (with a particular emphasis on dust storms, Wang and Richardson 2015; Guzewich et al. 2017) and placing InSight's measurements in a more global meteorological context.

The perspective of surveying cloud activity is particularly interesting, because imaging clouds from the surface will be possible by IDC and ICC on board InSight. Notably, to image both the surface and the atmosphere, the IDC will be possibly used to acquire a 360-degree panorama of the landing site. Cloud observations from the surface can be used to understand small-scale (compared to orbital images) morphology of clouds; repeat imaging can be used to determine the rate of angular motion, which may be compared to models. This approach has been particularly fruitful during the Phoenix and the Curiosity mission (Moores et al. 2010, 2015b). As part of the campaign to monitor atmospheric opacity (see

Sect. 3.3.2), approximately 100 sky images will be obtained over the nominal InSight mission. Additional images may be acquired with the opacity images, to allow use of pairs or sets to determine motion, or to search for clouds at other times of sol. At a minimum, the opacity-related images acquired by the InSight cameras will be inspected for discrete clouds to prevent spatial variation in clouds from being interpreted as a brightness gradient in a compositionally uniform sky. This cloud survey from the surface will complement the cloud monitoring from orbit at larger spatial scales.

Joint orbital / ground-based measurements could also be a fruitful source of information for the meteorological analysis. A recent example had been provided by Guzewich et al. (2017) who created a vertical profile of dust mixing ratio from the surface to the upper atmosphere over Gale Crater by using observations by the Curiosity rover and by the MCS on board MRO (which have an altitude resolution of 4–6 km, Kleinböhl et al. 2009). This enables a seasonal monitoring of the Martian dust cycle in the whole troposphere, from the dust loading in the PBL to the high-altitude dust layers (Heavens et al. 2011, 2014). Such a joint observational campaign to study the dust cycle will be possible using the InSight measurements (Sect. 3.3.2) along with the MRO / MCS profiles, the TGO Atmospheric Chemistry Suite (ACS) infrared spectrometers (Korablev et al. 2018), and the MEx / Planetary Fourier Spectrometer (PFS, Giuranna et al. 2005; Wolkenberg et al. 2011). The scope of such joint measurements is not limited to the dust cycle: studying from orbit the variability of temperature and clouds in the Elysium region hosting the landing site of InSight will be key to place InSight imaging, meteorological and seismic measurements in a regional-to-global climatic context, enabling to use numerical modeling (Sect. 2.2) as an additional means to understand the atmosphere of Mars and interpret the orbital and *in situ* observations in an unified framework. The TGO orbital setting is particularly interesting in that respect: for instance, the TIRVIM Fourier-spectrometer, part of ACS on TGO, will sample the diurnal cycle of temperature, dust opacity, and possibly cloud opacity, in all regions of Mars (outside polar latitudes) within 30 Earth days of operation (Korablev et al. 2018).

4.4 Coordinated Campaigns with Rovers

Simultaneous atmospheric measurements on board Curiosity (REMS) and InSight (TWINS) with similar instruments will be useful to broaden the knowledge of the Martian atmosphere. In particular, joint REMS / TWINS measurements could help to better interpret the meteorological phenomena recently attributed to the specific location of Curiosity within a crater and the influence of topography-induced circulations (Haberle et al. 2014; Harri et al. 2014; Pla-Garcia et al. 2016; Ullán et al. 2017; Newman et al. 2017). For instance, it will be interesting to compare the turbulent convective activity in daytime between the InSight landing site in Elysium Planitia and the Curiosity site in Gale Crater, where the growth and activity in the daytime PBL is adversely affected by slope circulations (Tyler and Barnes 2015). Another example mentioned in Sect. 2.3 is to take advantage of the continuous PS acquisition to search for the nighttime convective vortices discovered by Curiosity (Kahanpää et al. 2016) in the flat InSight landing site, in order to confirm the proposed topographical origin for those events (Rafkin et al. 2016; Ordonez-Etxeberria et al. 2018).

An extension of the InSight mission would have the benefit to extend the temporal coverage of the meteorological acquisitions by InSight towards the planned operations of atmospheric measurements on board the rovers to be launched in 2020 by NASA (Mars 2020) and ESA/Roscosmos (ExoMars)—as well as, potentially, by both the China National Space Administration (CNSA) and the Indian Space Research Organisation (ISRO, Magalayaan 2). The synergy between the measurements of those *in situ* spacecraft could set the path for future meteorological networks at the surface of Mars.

5 Atmospheric Science with Seismometers

The goal of this section is to illustrate and quantify what will be learned about the atmosphere from the seismic signals acquired by InSight. Part of the discussions also focuses on describing how the knowledge on atmospheric activity can be employed to estimate the atmosphere-induced seismic noise (following the discussions in Sect. 4.2), although a complete description of the so-called "decorrelation" methods is out of the scope of this paper. In other words, we discuss both how meteorological measurements can be used to interpret seismic data and how the seismometer data can be used to learn about the atmosphere, from turbulent motions to large-scale circulations.

5.1 General Background on Atmospheric Sources of Seismicity

On Earth and on Mars, the impedance contrast at the surface is such that internal motions are hardly generating any motion in the atmosphere. However, pressure fluctuations in the atmosphere produce easily detectable seismic signals in the solid part of the planet.

Consider that the planet's surface is elastic and, as such, responds to a changing atmospheric load. Three effects arise and produce an observable acceleration signal on a seismometer. Assume that the pressure in the atmosphere above a vertical component accelerometer is increasing, the sensor will experience three forms of acceleration:

$\mathcal{V}_1$) an upward acceleration due to the Newtonian attraction of the increasing mass of the atmosphere;

$\mathcal{V}_2$) a downward acceleration due to the elastic compression of the crust (inertial effect);

$\mathcal{V}_3$) a downward acceleration due to the downward displacement in a gravity gradient field (free-air effect).

While the first and the third effects are independent of frequency, the second one is not. Similarly, there are three physical effects to which a horizontal accelerometer responds: Newtonian attraction from the redistributed mass $\mathcal{H}_1$, inertial acceleration $\mathcal{H}_2$, and ground tilt $\mathcal{H}_3$.

Usually, the impact of atmospheric motions on the seismic signal is split between two classes: low-frequency and high-frequency signals. Low frequencies are frequencies for which simple models (horizontal layering or plane waves) provide an adequate description of the atmosphere to treat the interactions between the atmosphere and the solid planet. On Earth, these simplistic models work approximately below 2 mHz for the vertical components and below 6 mHz for the horizontal components (e.g., Zürn and Widmer 1995). We retain a similar distinction (although admittedly not as well-constrained as in the terrestrial case) between frequencies here: the two following subsections are dedicated to seismic noise associated with atmospheric fluctuations

- at high frequency, i.e. timescales less than an hour (frequencies approximately above 1 mHz): turbulence, dust devils, fastest gravity waves (Sect. 5.2)
- at low frequency, from hourly to annual timescales: inertio-gravity waves, thermal tides, planetary waves, seasonal cycles (Sect. 5.3)

At high frequency, the Newtonian ($\mathcal{V}_1$) and the free-air ($\mathcal{V}_3$) accelerations are overwhelmed by the inertial acceleration ($\mathcal{V}_2$). As a result, simple correlation between ground velocity and atmospheric pressure is expected at high frequency, in contrast with the low-frequency atmospheric-induced noise in which a correlation between ground acceleration and atmospheric pressure is anticipated.

5.2 High-Frequency Atmosphere-Induced Seismic Signals

5.2.1 Turbulence

Studying the energy, or amplitude spectral density, of the wind speed can provide important information about atmospheric turbulence. Both daytime LES results (Murdoch et al. 2017b) and observations (see e.g. Phoenix measurements by Davy et al. 2010) indicate that most of the atmospheric kinetic energy is contained in large-scale and slowly-evolving structures and, as a result, the spectrum at low frequencies ($f \lesssim 1$ mHz, as is defined above) should be both relatively flat and higher in amplitude than at higher frequencies.

In the intermediate (inertial) regime, energy begins to cascade from large-scale structures to smaller and smaller scale structures by the well-known Kolmogorov cascade (e.g., Garratt 1992; Vallis 2006). The size of the smallest structures is determined by when the inertial forces of an eddy are approximately equal to the viscous forces. At this point, at the highest frequencies, the inertial regime moves into the dissipation regime and the spectrum should fall off very steeply because the viscosity strongly damps out the eddies.

The high-frequency fluctuations of atmospheric pressure are particularly prominent during daytime convective motions associated with PBL turbulence (see Sect. 2.3). Significant differences are also expected between the high frequency turbulence observed in the atmospheres of Mars and of the Earth. For example, the high-frequency end of the inertial regime is set by the Kolmogorov length (Garratt 1992), corresponding to when the turbulent structures are so small that molecular diffusion starts to become important (this part of the inertial regime is left unresolved by LES). Due to the very low atmospheric density on Mars, this length scale is much larger on Mars than on Earth (Larsen et al. 2002; Petrosyan et al. 2011). As a consequence, the extent of the inertial regime is anticipated to be greatly reduced on Mars.

The transition from large scales to the inertial regime has previously been estimated to be in the range of 10 and 100 mHz using Mars Pathfinder temperature fluctuation data (Schofield et al. 1997), and to be at ~ 10 mHz using Phoenix data (Davy et al. 2010). However, there are currently no *in situ* measurements at high enough frequency on the surface of Mars that can provide information about where the transition from the inertial to the dissipation regimes occurs on Mars. Indirect diagnostics based on scaling arguments indicate that the Kolmogorov length would range from 7 mm to 2 cm on Mars (Petrosyan et al. 2011), but this transition from inertial to dissipation regimes has never been constrained directly from measurements.

Assessing this transition of turbulent regimes on Mars will be possible with the InSight / TWINS measurements that could allow to obtain the shape of the temperature and wind spectrum on Mars across a large bandwidth, up to the high frequency of 1 Hz. The lowest frequencies accessible by the InSight APSS (wind and pressure) sensors will be set by the wind speed and the measurement height, which determines the typical dominant eddy size. The highest frequencies will be several Hz—limited by the response times of the instruments; see Sect. 3. The seismic sensors, however, will measure to higher frequencies (up to 100 Hz, depending on the operational mode in use, see Sect. 4), and are known to be sensitive to atmospheric turbulence, as is explained in Sect. 5.1. In fact, the ground tilt due to atmospheric pressure fluctuations is expected to be one of the major contributors to the seismic noise recorded by the SEIS instrument (Mimoun et al. 2017). Up to what frequencies is the seismic data likely to prove useful as a proxy for atmospheric turbulence is, however, yet to be determined by future studies using InSight measurements. A preliminary study that could be carried out during deployment is to analyze the SEIS VBB and SP measurements

before the WTS is covering the seismometers, when the direct wind-induced noise will be particularly strong.

Another topic related to atmospheric turbulence is the possibility to use high-frequency pressure measurements to perform pressure decorrelation of the seismic signal. Murdoch et al. (2017a) investigated the elastic response of the ground as a result of three-dimensional atmospheric pressure fluctuations associated with PBL turbulence. They couple a Green's function ground deformation model (which is shown to yield results close to the formalism in Sorrells 1971, see also Sect. 4.2), to the results of atmospheric LES modeling (Sect. 2.3). The dominant seismic signal caused by atmospheric fluctuations is the horizontal acceleration $\mathcal{H}_3$ associated with the ground tilt. The vertical inertial acceleration $\mathcal{V}_2$ is about an order of magnitude smaller and the inertial horizontal acceleration $\mathcal{H}_2$ about two orders of magnitude smaller. The ground is modeled as an elastic half-space with properties of a Martian regolith but this seismic noise would be reduced in the presence of a harder layer at some shallow depth. More detailed information about the regolith compressibility will actually be obtained by InSight from the seismic signal after pressure decorrelation, which will in turn enables a better assessment of the seismic signatures (ground tilt) associated with the turbulent variability of pressure.

The correlation between the seismic signal (as measured by SEIS) and the pressure signal (as measured by APSS) is found to be higher in the windiest, more turbulent period because the seismic pressure noise reflects the atmospheric structure close to the InSight seismometer. The main source of pressure noise during such daytime periods is the turbulence excited by the convective cells (see Sect. 2.3) which dominate at scales below 1 km. Using the synthetic seismic noise derived from Large Eddy Simulations, Murdoch et al. (2017a) demonstrate that it is possible to decorrelate the atmospheric noise from the seismic signal measured by SEIS by using the pressure measurements of APSS. The decorrelation technique they tested with the synthetic data results in a factor of 5 reduction in the horizontal tilt noise (in the direction of the mean wind; on the orthogonal component, decorrelation is less efficient) and the vertical noise caused by atmospheric circulations in the 1–100 mHz bandwidth.

This decorrelation process is key to ensure InSight's accurate measurements of seismic activity in the interior of the planet, one of the major science objectives of the mission. It is likely that the decorrelation envisioned in Murdoch et al. (2017a) will be less efficient for real data when noise from multiple sources are superposed. This might be mitigated to some extent by comparing APSS high-frequency pressure measurements to predictions obtained by LES, carried out with regional wind conditions actually observed by TWINS (which is not intended for decorrelation, but to indicate wind conditions). At any event, the experience gained on the pressure decorrelation all along the InSight mission will be helpful for operations, to guide the choice of the best atmospheric conditions—local time, season, wind velocity—to prioritize the analysis of interior-related seismic signal.

Furthermore, as the seismic pressure noise will often dominate the SEIS signal before decorrelation, this offers a unique opportunity for studying the wind spectra and thus the atmospheric turbulence. Combined measurements made by the APSS instruments and SEIS will allow investigations to be made of key characteristics of the Martian atmosphere and properties of daily cycles; the wind spectrum will change dramatically with time of day (from the daytime super-adiabatic convective conditions to the nighttime ultra-stable conditions) and wind speed (shifting the frequencies up and down for a given eddy scale, and emphasizing the importance of shear-driven vs. buoyancy-driven turbulence). The SEIS and APSS measurements will be particularly complementary as the seismometer is sensitive to atmospheric fluctuations in a region much larger than the local APSS measurements.

Finally, the mechanical noise of the lander, transmitted through the ground to the seismometer (Murdoch et al. 2017b), may provide an additional method for studying the wind properties (Murdoch et al. 2018). The shape of the mechanical noise closely follows that of the wind spectrum, giving direct access to wind spectrum shape should this signal be clearly identified in the seismic data. This mechanical noise would have to be distinguished from the pressure noise: this might be achieved by pressure decorrelation, by characterizing the spectral dependence of the two kinds of seismic noise, and possibly by decoupling their distinct impact on the different axes of motion. Joint measurements with TWINS will also be necessary to relate the lander-induced mechanical noise to reliable information about winds close to the surface of Mars.

5.2.2 Dust Devils and Convective Vortices

Dust devils (and their dustless instances, convective vortices, see Sect. 2.3 and e.g. Murphy et al. 2016; Spiga et al. 2016, for a review) are part of the PBL turbulence described in Sect. 5.2.1. Nevertheless, compared to other convective motions in the daytime PBL, they cause distinctive signatures in the seismic signal, which requires a dedicated discussion. With the combination of pressure, wind speed and direction information from InSight, it should be possible to reconstruct with only modest uncertainty and ambiguity a model for each major dust devil encounter wherein a vortex is described by a diameter, core pressure drop, migration velocity and miss distance (Lorenz 2016). Such a model can also be used to generate surface tilt histories due to the negative pressure load applied by a vortex to the elastic surface, as indicated in terrestrial field experiments (Lorenz et al. 2015).

For Mars, Kenda et al. (2017) show, by combining a Sorrell formalism with atmospheric Large-Eddy Simulations (Sect. 2.3), that convective vortices (giving rise to dust devils when dust is lifted and transported in the vortex) cause high-frequency pressure fluctuations leading to, through quasi-static surface deformation, detectable ground-tilt effects by the InSight SEIS VBB seismometers. High-frequency records exhibit a significant excitation corresponding to dust devil episodes: not only because of direct wind noise associated with the dust devil, but also because shallow surface waves arise from atmosphere-surface coupling. Kenda et al. 2017 showed that at higher frequency (above 1 Hz) dust devils generate, in addition to infrasounds (Lorenz and Christie 2015), seismic waves propagating in the shallow layers of the subsurface. The latter phenomenon would allow for using dust devils as a passive source for seismic profiling down to a 50 m depth.

Furthermore, there are indications from fieldwork and modeling (Lorenz et al. 2015; Kenda et al. 2017) that the seismometer may record dust devil or convective vortices passing hundreds of meters away from the spacecraft and which may not lead to fluctuations detectable by the wind and pressure sensors (see modeling results in Fig. 11). This means that the seismometer will sense a larger region around the landing site: modeling by Kenda et al. (2017) indicates that InSight / SEIS should be able to detect the signal from a convective vortex up to a distance of a few hundred meters from the vortex. Therefore the statistics of vortex encounters derived from InSight will be more reliable compared to existing datasets, based only on single-station meteorological experiments on board previous landers and rovers on the surface of Mars (Ellehoj et al. 2010; Kahanpää et al. 2016).

Seismic measurements by InSight give additional constraints on the characteristics of dust devils and convective vortices. Shallow surface waves triggered by convective vortices in the high-frequency data (seismic and pressure) may be used to characterize the distance and the intensity of the episodes (Kenda et al. 2017). Additionally, the direction of the tilt directly gives the back azimuth, that is the direction of the vortex center with respect to the

station, as a function of time. Coupled with wind measurements with TWINS, the back azimuth permits to reconstruct the distance and trajectory of the vortex, without the need for additional modeling. The trajectory of the vortex would be a fair indication of the regional and large-scale winds in the Elysium region, as was shown by Reiss et al. (2014) who compared remote-sensing estimates with global climate modeling. Moreover, the amplitude of the tilt signal depends on the distance and pressure drop of the dust devil (Lorenz 2016), and on the elastic properties of the subsurface; the latter will be determined from active and passive experiments (see Kedar et al. 2017; Knapmeyer-Endrun et al. 2016; Golombek et al. 2018), hence it will be possible to estimate the core-pressure drop from the amplitude of the seismic disturbance, even for vortices not passing right over the station.

Even without the added dimension of seismic signatures of dust devils, the InSight instrumentation (see Sect. 3) promises to yield a dataset that will surpass previous missions in several ways in characterizing a Martian dust devil population. First, a full Mars year of quasi-continuous observations of pressure at high frequency of 2 Hz (and 20 Hz for selected events, see Sect. 4) is unprecedented; Curiosity and Viking have been longer but at lower cadence; Phoenix and Pathfinder observed for less than an Earth year. Second, the instrumentation is superior—microbarometer has exceptional sensitivity (unlike Viking), but is augmented by wind speed and direction sensing (the capabilities in which have been compromised to one extent or another in landers since Viking). Furthermore, the context for dust devil occurrence will be documented in more detail on InSight, owing e.g. to the radiometer used to sense ground temperatures in support of the interior heat flow investigation (see Sect. 6.1 for details on studying the surface layer with InSight instruments).

5.2.3 Gravity Waves

Gravity waves propagate as perturbations of the stratified atmospheric fluid, with the buoyancy force being the restoring mechanism (see Gossard and Hooke 1975; Fritts and Alexander 2003, for a review). Gravity waves are ubiquitous in the Martian atmosphere and were actually one of the first Martian atmospheric phenomena to be witnessed by orbiting spacecraft (Pickersgill and Hunt 1979). Those waves can be triggered in the Martian lower atmosphere by different sources: topography, convection, or jet-streams and fronts in ageostrophic evolution. Given their typical periods ranging from several minutes to several hours (Fritts and Alexander 2003), gravity waves may be classified either in the above-defined high-frequency range (> 1 mHz, fastest gravity waves) or in the low-frequency domain (inertio-gravity waves).

Using low-frequency seismic noise observed at a quiet terrestrial observatory, i.e. not overwhelmed by the seismic activity of the planetary interior, Zürn et al. (2007) considered a traveling wave model (TWM). In this model, a plane acoustic-gravity wave propagates by the seismometer, and the latter rests on a homogeneous elastic layer over a rigid half space. The TWM predicts that all three horizontal acceleration effects $\mathcal{H}_{1,2,3}$ (Newtonian attraction from the redistributed mass, inertial acceleration, and ground tilt, which may be of comparable amplitude at low frequency) are in phase, and produce accelerations which are 90 degrees out of phase with the forcing pressure variation. This 90-degree phase shift is non-intuitive, because it may lead to seemingly acausal signals. However, it is explained by the fact that the barometer will detect the pressure front only at the moment that it passes overhead, while the seismometer will start to tilt well before the pressure front has arrived, due to the deformation of the surface region near the sensors. This model also predicts that vertical accelerations $\mathcal{V}_{1,2,3}$ are in phase with pressure variations.

The model described above (TWM) is for plane waves. We present here numerical simulations of realistic high-frequency gravity wave effects on the ground velocity and tilt,
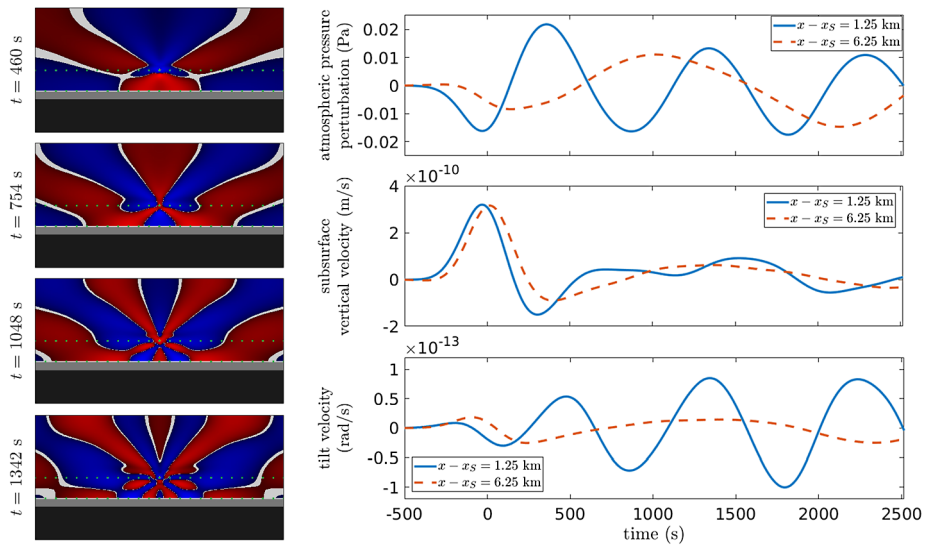
Fig. 15 On the left, from top to bottom, snapshots of pressure perturbations (satured at 1% of maximum amplitude) at various times during the simulation. Green dots indicate the positions of simulated seismic/infrasounds recording stations, with a separation of 1.25 km in between stations. Bottom part of the snapshots represents the solid viscoelastic model layering. On the right, from top to bottom, pressure variations at the surface (in Pa), ground vertical velocity (in m/s) and rotation speed (in rad/s), along an axis perpendicular to simulated plane, at two stations with horizontal distances from the source of 1.25 km (continuous line) and 6.25 km (dashed line). Note that the snapshots does not show the vibrations in the ground due to their very low amplitude, but they are computed in the simulation

by using a recently published numerical tool (Brissaud et al. 2017). This tool solves the mechanical coupling between a viscoelastic solid and the atmosphere (described by integrating the Navier-Stokes equations). Consequently, this simulation is able to predict inertial effects ($\mathcal{V}_2$ and $\mathcal{H}_2$) which are dominant at high frequencies. The computation domain is two-dimensional, with an isothermal 5-km-thick Mars atmosphere on top of a subsurface model described in Delage et al. (2017). A gravity wave source of dominant frequency 1.5×10^{-3} Hz is inserted at an altitude of 2.5 km above the surface, to mimic the gravity waves triggered by either convection in the daytime PBL (see Sect. 2), or wind impinging on a mountain (Pickersgill and Hunt 1979; Spiga et al. 2012), or convection within dust storms (Spiga et al. 2013; Imamura et al. 2016). The gravity wave frequency is chosen to be typical of Martian conditions.

Figure 15 describes the results of the simulation. The snapshots presented on the left clearly shows the gravity wave perturbations propagating from the source region. The simulated atmospheric surface pressure perturbations, ground vertical velocity and rotation speed, i.e. time derivative of tilt, at the surface are presented as a function of time for two different stations. The amplitude ratio between pressure and ground vertical velocity signals agrees with the relations presented in Sorrells (1971) and Murdoch et al. (2017a), when used with the measured horizontal speed of the gravity wave and the ground properties of the first layer. At the beginning of the simulation ($t < 800$ s) the station close to the source (continuous line) presents ground movements in phase with pressure, whereas the station far from the source (dashed line) is mainly sensitive to the ground tilt generated by the first and most energetic pressure variations just below the source, and not to the pressure wave measured

at the station itself. At the end of the simulation (t>800s) plane gravity waves are propagating and both stations present vertical velocity variations shifted by 90 degrees relative to local pressure variations. The direct numerical simulation described here confirms that the pressure and seismic velocity signals are not in phase, as is discussed above and in previous studies (Zürn et al. 2007; Murdoch et al. 2017a). The ground rotation speed is in phase with pressure variations, consistent with the prediction that ground tilt is 90 degrees out of phase relative to local pressure variations for plane wave.

The amplitude of the pressure wave in the considered simulation case is about 0.02 Pa, whereas typical perturbations induced by gravity waves are about a thousandth of the ambient surface pressure, according to terrestrial measurements (e.g., Gossard and Munk 1954). This would translate to a range of about two tenths to a couple Pascal on Mars, given typical ambient surface pressure on this planet. Our simulations can be linearly scaled up to these values by multiplying all the simulated quantities by ten. Consequently, the magnitude of vertical ground velocities induced by gravity waves is predicted to be $\sim 2 \times 10^{-9}$ m s^{-1}. Even if this result is strongly dependent of the sub-surface model, it suggests that gravity waves signal is at the limit of what could be measured by SEIS at the surface of Mars, and may generate significant low frequency atmospheric noise due to tilt effects. In other words, in addition to the direct pressure signal detected by the meteorological package, gravity waves could induce vertical ground velocities detectable by InSight / SEIS.

The discussions thus far focused on gravity waves emitted by atmospheric motions ("endogenic" sources). Meteor impacts ("exogenic" sources) could also cause acoustic-gravity waves detectable by the InSight instrumentation, either through direct excitation (Garcia et al. 2017), or by indirect excitation due to (seismic) Rayleigh surface waves resulting from an impact (Lognonné et al. 2016).

Garcia et al. (2017) applied a two-dimensional finite-difference model, simulating the propagation of acoustic and gravity waves in planetary atmospheres, to the case of surface explosions analogous to meteor impacts on Mars in various conditions of ambient wind and attenuation by CO2. They show that acoustic waves directly generated by meteor impacts can refract back to the surface on wind duct at high altitude. Furthermore, the strong nighttime near-surface temperature gradient, associated with radiative cooling on Mars, cause a trapping of the acoustic waves in a waveguide close to the surface. This will allow for the night-side detection of impacts by InSight at large distances in Martian plains.

Lognonné et al. (2016) have shown through modeling how Rayleigh surface waves excited by the airburst from impacts might be detected by the seismometer, and conversely, how the coupled acoustic wave forced by those low-frequency Rayleigh waves (acoustic cut-off frequency 2.2 mHz) could be detected with the pressure sensor. The Insight atmospheric package will possibly allow the direct measurement and characterization of this kind of seismically-induced acoustic waves regulary measured on Earth after large teleseismic earthquakes or large volcano eruptions. Their attenuation in the Martian atmosphere dominated by CO_2 gas, as theorized by Petculescu and Lueptow (2007), still needs to be quantified.

5.3 Low-Frequency Atmosphere-Induced Seismic Signals

5.3.1 Typical Vertical and Horizontal Noise

In the fields of terrestrial tidal gravimetry (Warburton and Goodkind 1977) and low-frequency seismology (Zürn and Widmer 1995), it is well established that the locally

recorded atmospheric pressure is correlated with the output of a vertical component inertial accelerometer. A fit of the pressure signal to the acceleration typically yields regression coefficients on Earth in the range of 3–4.5 nm s^{-2} hPa^{-1}. The magnitude of this coefficient is compatible with a simple physical model involving the Newtonian attraction of the atmosphere above the sensor (acceleration term $\mathcal{V}_1$). What is the magnitude of the pressure admittance for Mars and what are the typical acceleration signal expected for daily and annual atmospheric pressure fluctuations?

In its simplest form we model the atmosphere as a homogeneous layer of height H and constant density ρ. The Newtonian attraction of this atmospheric layer (considered as a Bouguer plate) results in an upward acceleration of $a_B = -2\pi\rho\mathcal{G}H$ where $\mathcal{G}$ is Newton's constant of gravity. The pressure at the bottom of this atmospheric plate is $p_B = \rho g H$ where g is the acceleration of gravity. It follows that variations in the air density $\Delta\rho$ lead to a change in both atmospheric pressure and gravity acceleration, with a constant admittance K connecting the two variations:

$$K = \frac{\Delta a_B}{\Delta p_B} = -\frac{2\pi\mathcal{G}}{g}.$$

This simple form of the admittance actually holds approximately for any horizontally stratified atmosphere. At the surface of Mars, gravity g is 3.72 m s^{-2}, about 3/8 times the value on Earth, hence the admittance value is $K_M \sim 11$–12 nm s^{-2} hPa^{-1}.

The two Viking missions established the annual surface pressure variations at about 2.5 hPa (Hess et al. 1980), as is caused by the seasonal cycle of CO_2 condensation on the Martian caps. A similar range holds for the InSight landing site according to the estimates presented in Fig. 6 in Sect. 2.2. Atmospheric thermal tides in subtropical latitudes induce a typical diurnal cycle of pressure of amplitude 0.4–0.5 hPa peak-to-peak (Wilson and Hamilton 1996; Read and Lewis 2004, and Fig. 7). The Curiosity rover measured peak-to-peak amplitudes in the diurnal cycle of pressure of 0.85 hPa on average (Haberle et al. 2014, and see Fig. 3), owing to constructive interference of the eastward and westward tidal modes, as well as amplification by crater circulations. According to GCM results in the MCD (see Sect. 2.2 for further details), at InSight's landing season ($L_s = 295°$) and location, this tidal peak-to-peak amplitude might reach 1 hPa in a Martian year with sustained dust storm activity (e.g. MY28), resulting from an enhanced semi-diurnal tidal mode. For these two principal harmonic pressure fluctuations, we thus predict atmosphere-induced vertical accelerations of $a_d = 11$ nm s^{-2} at a frequency of 1 cycle per Martian sol and $a_a = 55$ nm s^{-2} at a frequency of 1 cycle per Martian year. While the latter would drown in instrumental drift and in the thermal signal, the former (thermal tides) may be observed by InSight since thermal fluctuations near the SEIS instrument package are less of an issue at periods close to the Martian sol. Let us assume InSight will obtain an undisturbed $\delta t = 10$-day-long record of the vertical acceleration (undisturbed meaning the thermal environment around InSight is similar from day to day, which is usually the case outside the dust storm season). The variance of the daily pressure signal is $\sigma^2 = 1/2 p_d^2$ so that the power spectral density δ of this harmonic becomes $\delta = \sigma^2 \delta t \simeq 7 \times 10^{-6}$ m s^{-2} Hz$^{-0.5}$. Given that InSight SEIS' VBB has a noise floor of 1×10^{-9} m s^{-2} Hz$^{-0.5}$ at a frequency of 10 mHz, there is a good chance we will be able to observe a signal of 7×10^{-6} m s^{-2} Hz$^{-0.5}$ at 10 µHz (= one sol).

We can further assess the possible seismic detection of the thermal tide signal by using the MSL / Curiosity surface pressure measurements (Harri et al. 2014). Should the amplitude spectral density (ASD) of the surface pressure variations be known, the seismic noise caused by pressure variations through the free-air and Newtonian effects can be calculated. The highest sample rate and most precise pressure measurements to date are from the MSL
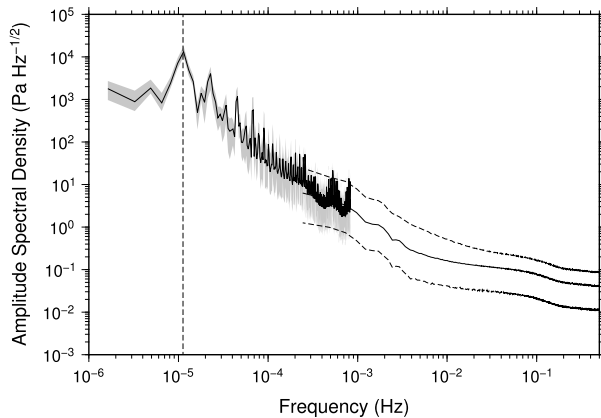
Fig. 16 Surface pressure amplitude spectral density (ASD) in Gale crater derived from 1648 sols of MSL REMS measurements. High frequency ASD (from 2×10^{-4}–0.5 Hz) is derived from 9333 1hr data segments with a continuous sampling rate of 1 Hz. Low frequency ASD (from 2×10^{-6}–8×10^{-4} Hz) is derived from 277 data segments, each with a length of 5 sols and selected to have data gaps less than 1 hr. Grey envelope and dashed lines show 90% confidence limits derived from the spread of the ASD of individual segments. Vertical dashed lines shows the diurnal frequency

rover REMS instrument, where measurements are acquired with sample rates of 1 Hz at regular and extended intervals during the mission (Gómez-Elvira et al. 2012). To estimate the pressure ASD, we use the entire current Planetary Data System (PDS) archive of pressure measurements, which covers mission sols 1–1648; we used a different approach for the computations of high-frequency and low-frequency variations. For high frequencies, we selected all segments of 1 hr duration with the full sample rate of 1 Hz, and calculated the ASD for each segment using the definition in McNamara and Buland (2004), then computed the median and 90% confidence interval from the resulting population of 9333 independent segments. For the low frequencies, continuous 1 Hz sampling was not available for long enough periods to get an accurate estimate. Therefore, we binned the pressure record for the entire mission into 10 minute bins, and selected all segments of length 5 sols that had at least one bin per hour, thus ensuring full diurnal coverage of the main pressure variation. This gave 277 segments with a 5-sol length that were used to calculate the low frequency ASD.

Figure 16 shows the resulting pressure ASD estimate. The low- and high-frequency analysis overlaps at intermediate frequencies, giving confidence to the estimates. The largest amplitude component is the diurnal variation, due to the atmospheric thermal tides (Haberle et al. 2014; Martínez et al. 2017) (and also the higher-frequency harmonics, which are discussed in Sect. 5.2). The pressure ASD has a "red" spectral shape, so becomes more important at long periods. The admittance K_M (defined above) can be used to calculate the equivalent acceleration ASD, which can be compared to the SEIS performance: we conclude that the pressure variations associated with Newtonian and Bouguer effects are likely to be well below the noise level in the seismic band. Nevertheless, at long periods, InSight seismometers may capture pressure variations associated with global thermal tides in the atmosphere, and provide information complementary to the APSS pressure sensor. We note, however, that the pressure ASD shown in Fig. 16 is expected to be at the upper end of the variability expected at the InSight landing site, since pressure variations within Gale crater

are expected to be about twice as much as those on the surrounding plains (Haberle et al. 2014).

The models presented here are quite simple, if not simplistic. We described the vertical component of the acceleration with a simple model consisting of a horizontally layered atmosphere over a horizontally layered solid planet. In the case of InSight seismometers, sensitive to both horizontal inertial accelerations and to ground tilt, we consider instead a horizontally layered atmosphere, in which pressure above the seismometer varies with time, located over a laterally heterogeneous subsoil (a local deformation model, as in the terrestrial study of Zürn et al. 2007). A tilting of the seismometer in phase with the pressure variations is expected and the direction of the tilt is entirely controlled by the heterogeneity underneath the seismometer. The amplitude of the generated acceleration cannot be easily predicted. Estimating the signal from ground deformation, that will create both vertical displacements and horizontal tilts, requires simultaneous knowledge of the wind speed and regolith properties, which are currently unknown. However, these simple models allow us to implement a simple preliminary strategy for pressure decorrelation of horizontal seismometer data, consisting of a simultaneous fit of the pressure and its Hilbert transform to the acceleration.

5.3.2 Atmospheric Hum

The global atmospheric variability on timescales ranging from hundreds to thousands of seconds (thermal tides, planetary waves, Hadley cells) can act as a continuous global excitation force for planetary free oscillations (Suda et al. 1998; Kobayashi and Nishida 1998) which periods correspond to the eigenfrequency of Martian normal modes. Those free oscillations can be detected through an ambient seismic "hum" at about 5–20 mHz (see e.g. Haned et al. 2016, and references therein). These normal modes are described by the equation governing the adiabatic oscillations of a self-gravitating sphere (Lognonné et al. 1998). Those modes are particularly interesting in the perspective of the InSight mission because they could constrain the internal structure of Mars (core and mantle), should they cause signatures that can be detected by SEIS—which remains an open question.

At low frequencies, spatial scales of atmospheric phenomena get so large that the use of very simplistic models (see Sect. 5.3.1) may become sufficient to describe their influence on the InSight seismometer package. Nevertheless, more sophisticated models are required to reach a correct quantitative estimate of the atmospheric "hum" on Mars. Based on $1° \times 1°$ GCM simulations similar to those presented in Sect. 2.2, normal modes for angular order 2 to 39 can be calculated and cause a signal of several nanoGals i.e. 10^{-11} m s^{-2} (Nishikawa et al. 2018). As is mentionned in Sect. 5.3.1, given the typical temperature fluctuations that SEIS would experience, it will be challenging to detect this signal given typical thermal noise (Lognonné et al. 2018). Specific strategies to reduce this noise in the dataset, e.g. emphasis on calmer nighttime conditions, and possible stacking of measurements over a long period of observation (taking advantage of the repeatable diurnal cycle on specific seasons at the InSight landing site, see Sect. 2.1), might enable to detect the Martian atmosphere-induced seismic hum.

5.3.3 Atmospheric Impact on the Seismic Signal Between High- and Low-Frequency Domains

The period range between 1 and 30 s of the Earth continuous seismic signal is largely dominated by the so-called "microseismic noise" caused by gravity waves in the oceans (e.g.

Schimmel et al. 2011; Ebeling 2012). As a consequence, the specific contribution of the wind on the seismograms is difficult to quantify. Few studies report that the wind affects both horizontal and vertical components between 0.1 and 10 Hz (Cara et al. 2003; Mucciarelli et al. 2005), and higher frequencies are mostly transmitted through the human constructions and trees. Atmospheric sources do not seem to modify the H/V ratio, the ratio between energy in the horizontal components versus energy in the vertical components. At larger periods (beyond 20 s), there is a strong correlation between wind and seismic energies mostly on the horizontal components.

InSight is a unique opportunity to quantify the effect of the atmospheric motions on the seismic signal with hardly no other contributions (compared to terrestrial conditions) other than the eigen-oscillations of the InSight lander (Mimoun et al. 2017; Murdoch et al. 2017b). Furthermore, the *in situ* conditions (SEIS instrument will not be buried and covered only by the WTS) will be met to characterize for the first time the record of the wind by a seismometer over a large frequency range.

Considering the sampling rate of the continuous signal transmitted to the Earth by InSight (see Sect. 4), it will be possible to statistically characterize the seismic signal for periods between 4 and 150 s. With this aim in mind, the instantaneous phase redundancy (Gaudot et al. 2016) is a valuable method to discriminate distinct sources (in terms of polarization angle and frequency) and the background signature of the signal. Using cross-correlation between the three different possible pair of components (one vertical and two horizontal: the three north-south, east-west and vertical components are obtained by applying a rotation matrix to the 120-degree-apart three components measured by SEIS, Lognonné et al. 2018), it is straightforward to compute C_i, the ith instantaneous phase coherence (Schimmel 1999). As is described in Gaudot et al. (2016), at a given lag time, the condition

$$\forall i \in \{1, 2, 3\}, \quad \mathcal{P}(C_i) = \frac{2}{\pi \sqrt{2 - C_i^2}}, \tag{1}$$

proves that the polarization of the continuous seismic signal is purely random (i.e. follows a Gaussian distribution of the seismic instantaneous phases). $\mathcal{P}(C_i)$ is the probability density function for the coherence of the ith component pair: any redundant contribution (lander oscillation for instance) leads to not satisfy Eq. (1) at particular lag times. Most of all, the overall mean average value of all individual C_i enables to define the polarization reference state and any weak-amplitude transient signal can therefore be detected as outlier samples.

This approach combined with classical seismic event detection, based on amplitude ratio, will allow to characterize atmospheric and internal sources. Since the instantaneous phase coherence is dominated by the carrying signal, a comprehensive frequency analysis using narrow band filters will be necessary to fully describe the atmosphere interactions with "solid Mars" (surface and interior) in the vicinity of the InSight landing site. As is previously mentioned in Sect. 3.2.1, TWINS will run continuously, which would provide the necessary information. The instantaneous phase coherence can be computed for two different components of the same instrument (such as SEIS), but also for two different instruments using normalized cross-correlations. The statistical redundancy can therefore be computed for the signal recorded simultaneously by SEIS and TWINS. The mixed instantaneous coherences will then, on the one hand, confirm the statistics inferred for SEIS only and, on the other hand, allow to quantify the wind effect on the different components.

6 Exploratory Science

In this section, we discuss in details three exploratory studies of unprecedented Martian atmospheric science with the InSight instrumentation. Interestingly, all three ideas relate to surface-atmosphere interactions and exchanges of heat, momentum, aerosols (dust) and molecular species (CO_2). It remains entirely possible that, once the InSight lander is at the surface of Mars, those studies would be challenging to perform for unexpected reasons. At any event, on the worst-case scenario, the tentative approach on the following topics would be a source of inspiration for future missions to Mars.

6.1 Surface Layer

Characterizing the near-surface climate of Mars has always been a high-priority goal of the Mars exploration program (Petrosyan et al. 2011; Martínez et al. 2017). On a planet like Mars, which possesses an atmosphere that is not optically thick in the infrared, there exists dramatic vertical changes between the surface temperature and the atmospheric temperature right above the surface. A crucial question is thus: how does the atmospheric temperature a couple meters above the surface (measured by landers and rovers) relate to the surface temperature?

This question relates to the transport of heat within a couple meters above the Martian surface, the so-called surface layer (Garratt 1992; Larsen et al. 2002; Martínez et al. 2009). The surface layer is defined as the lowermost part of the PBL, where surface-atmosphere interactions are most active. A complex interplay between conduction and convection takes place in the surface layer in which turbulence is produced by both shear and buoyancy. Terrestrial observations of the surface layer show that in this layer vertical fluxes of heat and momentum are almost independent of height and vary by less than 10% of their mean magnitudes—this is often how the surface layer is defined (Garratt 1992). Turbulent eddies that take place in the surface layer are of much smaller size than the ones developing in the mixing layer above during daytime (see Sect. 2.3), hence are left unresolved by LES.

Despite—or because of—its simplicity, the theoretical framework developed by Monin and Obukhov (1954) is still being used as a powerful and helpful means to describe averaged atmospheric fields in the surface layer (for a more detailed perspective, see Högström 1996; Foken 2006; Petrosyan et al. 2011). The so-called Monin-Obukhov "similarity theory" consists of a dimensional analysis in a stationary and homogeneous surface layer. Assuming that heat and momentum fluxes are independent of height in the surface layer, four independent variables can be defined:

– height above ground z,
– friction velocity $u_* = \sqrt{\sigma_0/\rho_0}$ where σ_0 is the wind stress on the surface and ρ_0 the atmospheric density,
– temperature scale θ_* such that $H_0 = -\rho_0 c_p u_* \theta_*$ where H_0 is the sensible heat flux (i.e. exchanges of heat between the surface and the atmosphere caused by small-scale turbulence in the surface layer) and c_p the specific heat capacity of the atmosphere,
– buoyancy parameter $\mathcal{B} = g/T_s$ where g is the acceleration of gravity and T_s surface temperature.

Those four variables can be combined to define the Monin-Obukhov length scale L

$$L = \frac{-u_*^2}{\kappa \mathcal{B} \theta_*},$$

where $\kappa \simeq 0.35 - 0.42$ is the von Kármán constant. The surface layer is limited to altitudes $z < |L|$ (Garratt 1992).

It follows from the Vaschy-Buckingham π theorem of dimensional analysis that the dimensionless coordinate z/L defines the scaling structure of the surface layer via the flux-gradient relationships for averaged velocity u and surface-atmosphere temperature difference $\mathcal{T} = T - T_s$

$$\Phi_m\left(\frac{z}{L}\right) = \kappa \frac{z}{u_*} \frac{d\bar{u}}{dz}, \qquad \Phi_h\left(\frac{z}{L}\right) = \kappa \mathcal{P}_t \frac{z}{\theta_*} \frac{d\bar{\mathcal{T}}}{dz}, \tag{2}$$

where $\bar{}$ denotes statistically-significant (with respect to turbulent structures) temporal or spatial averaging, and $\mathcal{P}_t$ is the turbulent Prandtl number.[4] The universal functions Φ_m for momentum and Φ_h for heat are named the (dimensionless) Monin-Obukhov fluxes and can be developed as power series with distinct formulations for a unstable or stable atmosphere. Empirical formulae for Φ have been derived from terrestrial measurements (e.g. Businger et al. 1971) and are assumed to be universal enough to be applied to Mars. Deriving Martian functions would require collocated *in-situ xz* measurements to get shear stress $\sigma_0 = -\rho_0 \overline{u'w'}$ where u' and w' are the turbulent component of horizontal and vertical velocity. This is beyond the past and current instrumentation sent to Mars, including InSight. The vertical velocity measured by TWINS will not be reliable (Sect. 3.2.1) and the available bandwidth would limit the ability to downlink to Earth extended series of high-frequency wind measurements for the two TWINS boom (Sect. 4).

The determination of the Monin-Obukhov fluxes (especially Φ_h) is a means to address the initial question considered in this section, namely how to compute the near-surface atmospheric temperature from the surface temperature (and, more generally, how to compute the atmospheric wind and temperature profiles in the surface layer). To illustrate this, let us choose the simplest Monin-Obuhov model for the surface layer by setting $\Phi_m(z/L) = 1$ and $\Phi_h(z/L) = 1$. This so-called "bulk" formulation, where Monin-Obukhov fluxes are constant with height, entails the well-known logarithmic surface layer formulation

$$\bar{u}(z) = \frac{u_*}{\kappa} \ln\left(\frac{z}{z_0}\right), \tag{3}$$

$$\bar{T}(z) = T_s + \frac{\theta_*}{\kappa \mathcal{P}_t} \ln\left(\frac{z}{z_{0T}}\right), \tag{4}$$

where z_0 is the roughness length (such that $\bar{u}(z_0) = 0$, representative of surface inhomogeneity for momentum transfer) and z_{0T} is the conduction/convection transition[5] (such that $\bar{T}(z_{0T}) = T_s$). More elaborate empirical functions than $\Phi_{m,h}\left(\frac{z}{L}\right) = 1$ must be used (Garratt 1992; Davy et al. 2010; Colaïtis et al. 2013) when strong variations of stability are expected on a diurnal basis, as is the case on Mars (Sutton et al. 1978).

The properties of the surface layer on Mars, including estimates of the Monin-Obukhov length, have been tentatively obtained from past lander measurements with some success

---

[4]$\mathcal{P}_t \sim 1$ is often assumed in the so-called "Reynolds analogy", although experimental values range from 0.73 to 0.92 and observations in the surface layer exhibit an even larger scatter (Businger et al. 1971; Li et al. 2015)

[5]A common assumption is $z_{0T} = z_0$. The difference between z_0 and z_{0T} is taken into account through the inclusion of a molecular sublayer in which the transfer of momentum and heat is dominated by molecular processes (Tillman et al. 1994; Martínez et al. 2009). The Martian surface flux is characterized as being in a somewhat smoother, more laminar regime than on Earth and z_{0T} will therefore be larger on Mars than on Earth, i.e. closer to z_0 (Larsen et al. 2002).

(Sutton et al. 1978; Tillman et al. 1994; Larsen et al. 2002; Määttänen and Savijärvi 2004; Martínez et al. 2009; Davy et al. 2010). It appears that the limitations of the Monin-Obukhov similarity theory (namely: neglecting Coriolis forces, not accounting for complex topography, assuming horizontal homogeneity e.g. by neglecting meteorological fronts on a regional scale) could be mitigated to first order with the *in situ* measurements considered for the analysis. One major limitation on Mars, however, could jeopardize the underlying assumption of constant fluxes in the Monin-Obuhov surface layer model:[6] owing to the presence of CO_2 as a major atmospheric component, the Martian atmosphere undergoes a strong near-surface radiative forcing (Savijärvi 1991), furthermore with significant seasonal variability of incoming sunlight and dust loading.

The instrumentation of InSight could help to assess the validity of the Monin-Obukhov theory on Mars. The objectives are twofold: on the operational side, this will permit to evaluate the near-surface stability conditions and to relate it to turbulent activity; on the scientific side, this will allow us to use Martian measurements to challenge the Monin-Obukhov theory, and might also provide constraints to Monin-Obukhov fluxes Φ_h through Eqs. (2) and (4). The key element is to get simultaneous measurements of both near-surface atmospheric, and surface, temperatures. This will be possible by combining near-surface air temperature measured by APSS / TWINS (Sect. 3.2.1) with surface temperature measured by HP^3 / RAD (Sect. 3.3.1).

Measuring the surface-atmosphere temperature gradients in the surface layer with InSight is a unique opportunity, not permitted by previous measurements. No ground temperature measurements were carried out before the Mars Exploration Rovers (see review by Martínez et al. 2017). The Mini-TES instrument on board Spirit and Opportunity did offer the interesting perspective to measure both air and surface temperatures with the same sensor (Spanovich et al. 2006), but it lacked coverage in nighttime conditions and the atmospheric temperature could only be retrieved down to 15 m above the surface (Smith et al. 2006), which greatly limits the perspective to conduct surface layer science. The Phoenix lander TECP instrument (Zent et al. 2010) was only able to measure surface temperature during less than 20 sols without systematic diurnal coverage, with the additional problem that temperature measurements are subsurface measurements over a 15-mm depth rather than true surface (regolith) measurements. The Curiosity rover is equipped with similar atmospheric and surface temperature sensors as InSight, but the presence of the Radioisotope Thermoelectric Generator (RTG) affects both air and surface temperature measurements (Hamilton et al. 2014; Martínez et al. 2017), making it difficult to combine both quantities in a surface layer analysis—InSight will avoid this problem because energy is provided by solar panels and not RTG. In addition to the possibility to measure both air and surface temperature, the InSight lander will also permit to assess high-frequency wind and pressure fluctuations, permitting to link the gradients of temperature in the surface layer to the near-surface turbulence at an unprecedented level.

Carrying out a similar campaign on the momentum flux Φ_m will be more difficult, for it requires the knowledge of u_* to compare it to the wind measured by TWINS about one meter above the surface. Aeolian studies presented in Sect. 6.2 could help to estimate u_*, albeit with neither the accuracy nor the temporal coverage that would be suitable for determining the shape of the Monin-Obukhov scaling Φ_m.

---

[6]This effect was also recently evidenced on Earth (Gentine et al. 2018).

6.2 Aeolian Erosion and Saltation Studies

Surface-atmosphere interactions are discussed both herein and in the paper dedicated to Geology investigations (Golombek et al. 2018). The description of surface features carved by eolian erosion on Mars pertains to the latter paper; in this paper, we describe in greater detail the atmospheric part of surface-atmosphere interactions. Of particular importance on Mars is the process of dust lifting and transport, which has implications for Mars' dust storms and global climate (Kahre et al. 2006; Madeleine et al. 2011; Guzewich et al. 2013).

The formation of aeolian features critically depends on the ability of the wind to lift small particles from the surface (Bridges et al. 2012). In the simplest model of particle lifting from the surface, this shall occur for friction velocity u_* above a saltation threshold velocity $u_{*,t}$ for particle lifting, where u_* is related to the wind $u(z)$ at an altitude z through the simple "bulk" formulation for the surface layer (see Eq. (3) in Sect. 6.1) in which the roughness length z_0 plays a central role. The InSight landing site scene is considerably smoother than the Pathfinder scene where a value of $z_0 \simeq 3$ cm was retrieved (Sullivan et al. 2000). In the aerodynamic roughness length map inferred from orbital measurements by Hébrard et al. (2012), the InSight landing site region is characterized by values of $z_0 \sim 0.1$–0.25 cm. This value of z_0 will be cross-checked with images acquired with InSight's IDC (Maki et al. 2018).

Imaging on board the InSight lander offers the opportunity to study aeolian transport: grain size distribution, velocity threshold, seasonal variations of sediment flux at the landing site (see Golombek et al. 2018). The lifting threshold can be estimated by comparing the measured movement of dune field ripples to predictions using GCM-derived winds (see Sect. 2.2). Estimates in Golombek et al. (2018) using recent observations of ripple migration from orbit indicate a typical threshold of $u_{*,t} \simeq 0.7$ m s^{-1}, which would correspond to a wind velocity of 10 m s^{-1} measured at APSS height. Multiscale modeling described in Sect. 2 shows that, as a result of global, regional and turbulent wind variability, this situation will occur quite frequently at the InSight landing site during science operations. Prior to landing and science operations, we may thus assess the expected direction of aeolian transport from wind fields predicted by meteorological models for Mars. In turn, combining surface wind measurements, saltation threshold estimates, and bedform observations from a long-lived surface station such as InSight will be a means to improve the predictions of those atmospheric models. As is mentioned in Sects. 3 and 4, since TWINS will be recording wind data continuously, the InSight instrumentation will be uniquely valuable in quantifying wind thresholds for aeolian surface changes (as well as solar panel dust removal events).

For a uniform unidirectional wind direction regime and for large sediment availability, the most likely bedform is a transverse dune or ripple, with a bedform strike perpendicular to the wind vector (barchan dunes in the case of limited sediment supply). Climate models show, however, that at the equatorial InSight landing site the diurnal and seasonal variations of Martian winds are significant (see Sect. 2.2; see also previous lander observations in Sect. 2.1). Recent laboratory experiments, numerical simulations and field measurements have demonstrated that multidirectional wind regimes can produce two dune trends according to sand availability (du Courrech et al. 2014). To determine the predicted bedform directions for the InSight landing site using GCM simulations described in Sect. 2, we thus adopt two distinct approaches corresponding to two competing dune growth mechanisms:

1. *Bed instability mode* Where there is no limit in sand availability, in transport-limited situations, dunes grow in height selecting the bedform orientation for which the gross bedform-normal transport (GBNT) is maximum. A modified version of the GBNT method of Rubin and Hunter (1987) is described in Sefton-Nash et al. (2014) who found

Fig. 17 Rose diagram of predicted wind vectors from GCM predictions over a martian year for the InSight landing site. Dashed lines give the predicted beform orientations under different GBNT assumptions. Wind vectors have been binned into 5° intervals. Rose bar lengths are area normalised

that their modifications gave an improved match between GCM predicted winds and observed bedform orientations.

2. *Fingering mode* Where the bed is partially starved of mobilizable sediment, dunes elongate in the direction of the mean sediment flux at their crest—where dunes grow from fixed sources of sediment, this is the orientation for which the normal-to-crest components of transport cancel each other (Lucas et al. 2015; Gao et al. 2015).

We consider GCM simulations with the LMD model (see Sect. 2.2) using the "average climatology" dust scenario that forms the basis of the MCD v5.3 (Millour et al. 2015). Values of zonal wind (u, west → east), meridional wind (v, south → north), and atmospheric density ρ were extracted from the model layer closest to the surface (5–6 m above local surface) four times a Martian sol throughout the Martian year. The value of u_* was calculated using the bulk surface layer formulation in Eq. (3), with $\kappa = 0.4$.

Simple GBNT predictions can be obtained through the general wind regime method of Rubin and Hunter (1987) modified by Sefton-Nash et al. (2014). The transport flux vector $\vec{T}$ is given by (Fryberger and Dean 1979):

$$\vec{T} \propto \rho u_*^2 (u_* - u_{*t}) \vec{x} \quad \text{if } u_* > u_{*t},$$
$$\vec{T} = 0 \quad \text{otherwise,} \tag{5}$$

where $\vec{x}$ is the unit direction vector of the wind. The predicted bedform orientation θ is found by maximizing the function:

$$\Phi(\theta) = \sum_{i=1}^{n} \rho_i u_{*i}^2 (u_{*i} - u_{*t}) \left| \frac{u_i \cos\theta - v_i \sin\theta}{\sqrt{u_i^2 + v_i^2}} \right| \quad \forall i \text{ where } u_{*i} > u_{*t} \tag{6}$$

for a wind time series with n wind horizontal wind vectors (u_i, v_i), $i = 1 \ldots n$. To be representative, the time series of n wind predictions must cover an entire Mars year. Following Sefton-Nash et al. (2014), we assumed two values for threshold lifting stresses, $\sigma = \rho u_{*t}^2$, of 0 N m^{-2} and 0.008 N m^{-2}. Results are shown in Fig. 17: assuming a Pathfinder-like surface roughness $z_0 = 1$ cm, predicted bedform orientations are respectively 38.3 and 49.6° (clockwise from North). The prediction for $\sigma = 0.008$ N m^{-2} becomes 51.6°, 56.6°, 59.5° for surface roughnesses of $z_0 = 5, 1, 0.1$ mm respectively.
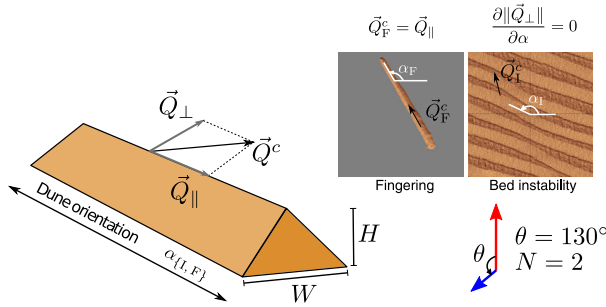
Fig. 18 Dune orientations associated with the bed instability and the fingering modes. The resultant sediment flux $\vec{Q}^c$ at the crest of a dune can be decomposed into two components ($\vec{Q}_\perp$ and $\vec{Q}_\parallel$) with respect to the the dune orientation α. The bed instability orientation corresponds to $\partial \|\vec{Q}_\perp\|/\partial\alpha = 0$. The fingering mode orientation corresponds to $\vec{Q}^c = \vec{Q}_\parallel$ and $\|\vec{Q}_\perp\| = 0$). Numerical examples are shown for a divergence angle $\theta = 130°$ and a transport ratio $N = 2$ between the two winds Gao et al. (2015). The dominant and secondary winds are shown using red and blue arrows, respectively. Note that, given the speed-up effect in multi-directional wind regimes, the resultant sand flux at the crest of dunes in the bed instability and fingering modes ($\vec{Q}^c_I$ and $\vec{Q}^c_F$) may differ not only in intensity but also in orientation (du Courrech et al. 2014)

The above simple method does not take into account the speed-up effect due to the feedback of the dune topography on the flow. Without the speed-up effect, GBNT computations are only valid for a flat sand bed. This can be revisited by developing a framework in which both the bed instability and the fingering modes are accounted for. In both cases, the sediment flux depends on the dune shape as a positive topography accelerates the wind. In case of a 2D turbulent flow over a gentle topographic relief, this increase of the wind velocity (the so-called speed-up effect) scales the bump aspect ratio (Jackson and Hunt 1975). Hence, considering the first order of the dune aspect ratio, and neglecting the transport threshold, the sediment flux at the crest of a linear dune is

$$\vec{Q}^c(\theta) = \vec{Q}(\theta)\big(1 + \gamma\big|\sin(\theta_i - \alpha)\big|\big), \tag{7}$$

where θ is the "divergence" angle between the two dominant directions of the wind field, and γ is the speed-up coefficient. For all possible crest orientations $\alpha \in [0; 2\pi]$, this sediment flux $\vec{Q}^c(\alpha)$ is calculated from $Q_\perp(\alpha)$ and $Q_\parallel(\alpha)$, the total sediment flux respectively parallel and perpendicular to the crest (see Fig. 18). The orientation for finger dunes α_F is obtained when $Q_\perp(\alpha) = 0$ and $Q_\parallel(\alpha) > 0$. If multiple solutions exist, we take the angle which maximizes $Q_\parallel$-value. Note that when the effect of the topography on the flow is not included (i.e., $\gamma = 0$ in Eq. (7)), this orientation is equal to the resultant sediment transport direction on a flat bed (Fig. 19).

All sediment fluxes perpendicular to the crest contribute to dune growth. Considering the dune orientations $\alpha_{\{I,F\}}$, we use the normal-to-crest component of transport to compute the characteristic growth rate $\sigma_{\{I,F\}}$ of a linear dune in either the bed instability or the fingering mode (du Courrech et al. 2014; Gao et al. 2015):

$$\sigma_{\{I,F\}} = \frac{1}{2\pi H W} \int_0^{2\pi} \big\|\vec{Q}(\theta)\big\|\big(1 + \gamma\big|\sin(\theta_i - \alpha_{\{I,F\}})\big|\big)\big|\sin(\theta_i - \alpha_{\{I,F\}})\big| \, d\theta. \tag{8}$$
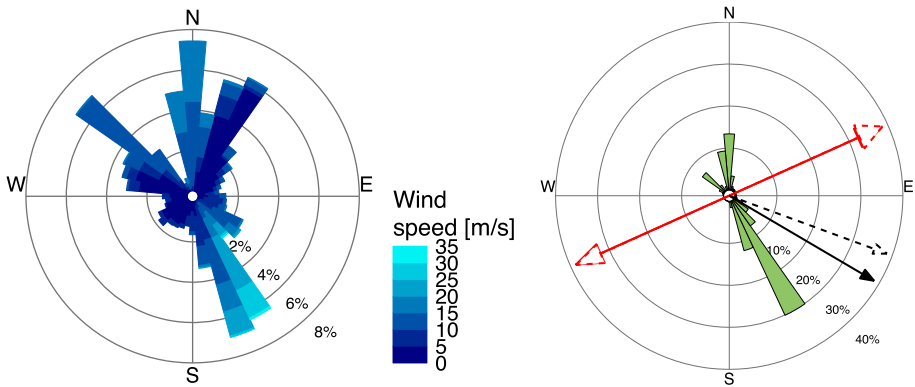
Fig. 19 Wind rose from GCM predictions at all seasons for the InSight landing site, and associated sediment fluxes distribution. Dune orientations for the two growth mechanisms are shown in red (bed instability) and black (fingering). Dashed is obtained for when speed-up effect is taken into account (i.e., $\gamma \neq 0$ (see main text)). Note that the wind roses differ slightly from Fig. 17 because both different binning and different scaling with wind velocity are employed here

Essentially, this quantity is the inverse of the time required to build up a linear dune of height H and width W. Using the GCM results, we obtained the orientations[7] shown in Fig. 19. The direction of the bed instability mode is compliant (as expected) with the GBNT estimates in Fig. 17, except for about ten degree difference caused by accounting for the speed-up effect in the bed instability case. This direction also appears consistent to first order to the orientation derived from eolian bedforms inside craters, and in the vicinity of fresh rocky ejecta craters, as well as dust devil tracks (Golombek et al. 2018).

Both the wind directions and bedform orientations can be verified during the deployment checkout stage, by measuring small ripples, small dunes, or modifications to regolith piles created by the scoop and rock wind shadow deposits. Throughout the science phase of the mission, surface changes induced by aeolian processes will be detectable using the arm-mounted camera IDC, and can be correlated to the continuously observed winds to yield a good understanding of the wind environment during the time when aeolian changes may occur. In the close vicinity of the lander site, aeolian processes inaccessible from the lander cameras, such as wind streaks and small dunes in craters close to the lander site, can also be monitored from orbit with orbital cameras (see Sect. 4.3) and compared with APSS wind measurements and GCM, mesoscale and/or LES modeling predictions (see Sect. 2).

Additional information on the aeolian transport on Mars (with specific emphasis on dust devils) may also be obtained through magnetic data. Indeed, the InSight mission will place, for the first time, a magnetometer at the surface of Mars (IFG, Russell et al. 2018). The main scope of the instrument is to correct seismic data for the effect of magnetic fields (Mimoun et al. 2017), however it may also measure magnetic signals generated by dust devils. Earth data (Farrell et al. 2004) and modeling (Kurgansky et al. 2007; Schmitter 2010) show indeed how atmospheric vortices carrying charged dust particles generate Ultra-Low-Frequency (ULF) magnetic fields. Should those ULF signatures be measured by the InSight magnetometer (whose measurements will be continously downlinked at frequency 0.2 Hz and available at frequency 20 Hz in event-based mode, see Sect. 4), it will be possible to

---

[7]Note that in case of the fingering mode, we can predict the direction of elongation as well as growth rate and resultant sediment flux (Lucas et al. 2015).

distinguish between dust devils and non-dust laden vortices. This has been previously done on the basis of images and solar-panel power records (Murphy et al. 2016, for a review), but these measurements are not always available or sensitive to dust devils. The proposed technique, aiming to establish whether a vortex is carrying dust or not, could be used to determine a threshold (in terms of pressure drop and wind velocity) for dust lifting: this is still an open problem, despite measurements from Mars landers, theoretical studies and analog laboratory experiments (Neakrase et al. 2016, for a review).

6.3 Secular Measurements of Pressure

The seasonal pressure cycle corresponding to the cycle of condensation / sublimation of CO_2 on polar caps (Figs. 2 and 6 in Sect. 2) will undoubtedly be measured by the InSight PS and most probably by the AAM estimates using RISE (Sect. 3). A last option, much more challenging, may be explored with the InSight PS.

Observations of inter-annual variations in polar cap coverage (Malin et al. 2001; Thomas et al. 2009; Blackburn et al. 2010) sparked suggestions that there might be long-term trends in the atmospheric pressure at Mars, in addition to the significant diurnal and seasonal pressure oscillations. This opens the possibility of secular climate change on Mars, related to the fact that the south polar residual cap (SPRC) of CO_2 ice may be eroding, losing mass year after year, thereby raising the global-mean surface pressure on Mars. Haberle and Kahre (2010) found a possible 10-Pa rise of surface pressure, potentially associated with the eroding SPRC, by comparing measurements by Phoenix with those by Viking 17 Mars years earlier, and correcting for both topography differences and atmospheric dynamics simulated by a GCM (see also Hourdin et al. 1993). Haberle et al. (2014) carried out the same analysis using MSL Curiosity surface pressure measurements within Gale Crater, but found little change compared to Viking, hence negligible net erosion of the SPRC. Nevertheless, the hydrostatic adjustment of surface pressure is very sensitive to the assumed temperature profile, especially when large topographical differences have to be corrected (which is the case for Gale crater), with the additional difficulty that high-resolution GCM has to be used to correct for the impact of atmospheric dynamics on surface pressure. Even Haberle and Kahre (2010), considering the more favorable Phoenix case, acknowledged that the combined uncertainties in both the measurements and the modeling methodology are enough to possibly jeopardize the signal of secular climate change.

The InSight PS is well suited to address the question of long-term, secular trends in Mars atmospheric pressure, with potential implications on the understanding of the stability of the SPRC. Because the InSight platform is fixed, no altitude changes in observed pressure need be accounted for (unlike that from MSL Curiosity), and only the instrument drift, noise and seasonal and diurnal variations confound the ability to identify secular trends in atmospheric pressure. Furthermore, the InSight measurements can be compared with Viking Lander 2 measurements in the same hemisphere also on a relatively flat surface, with limited hydrostatic adjustments between both locations. Following InSight's delay from a 2016 launch to a 2018 launch, a second pressure sensor calibration process was required,[8] using the Mars atmosphere simulation test chamber at Jet Propulsion Laboratory (JPL), after a delay of roughly two years from the initial calibration (Banfield et al. 2018). This enabled an assessment to be made of the long-term drift of the calibration of the flight model sensor.

---

[8]There are no means of calibrating the InSight PS during cruise (Banfield et al. 2018), given the pressure of deep space vacuum much lower than the PS lower limit of about 560 Pa (Sect. 3). No calibration is possible either once InSight has landed at the surface of Mars.

This long-term drift of order 1.5 Pa will be the main source of uncertainty in estimating secular change in Mars atmospheric pressure from the InSight pressure measurements. Nevertheless, this precision exceeds that identified in Haberle and Kahre (2010) to be of value in addressing this question.

7 Conclusion

The InSight mission shall be considered as a unique opportunity for both strengthening and broadening our knowledge of Martian atmospheric phenomena.

1. Two main large-scale wind regimes are expected at the Insight landing site during a typical year: towards the northwest in northern spring and summer, then in the opposite direction in southern summer. The transition between those two seasons exhibit a strong day-to-day variability in wind regime that will be interesting to follow with InSight. Both the large-scale and turbulent components of the wind are expected to cause aeolian change at the surface of Mars, that will be monitored by InSight's cameras—and the continuous acquisition of near-surface winds by InSight will enable to constrain the threshold velocity for particle lifting. A study of bedform migration and comparison with measured winds will also permit to discriminate between two possible dynamical regimes for dune and ripple migration. Besides, the exchanges of heat between the surface and the atmosphere in the surface layer will be quantified by simultaneous measurements of temperature by the meteorological package and surface brightness temperature by the InSight radiometer, with possibilities to explore the validity of the Monin-Obukhov scaling.

2. Surface pressure measurements record global-to-local atmospheric phenomena: CO_2 condensation (annual), dust cycle and storms (seasonal), baroclinic waves (weekly), thermal tides (daily), gravity waves (thousands of seconds), convective cells (hundreds of seconds), convective vortices (tens of seconds). Measurements of this atmospheric parameter by InSight will be carried out continuously at an unprecedentedly high frequency and sensitivity: this should enable not only the removal of atmosphere-induced noise from the seismic signal (as much as possible), but also the detection of new events not detected thus far at the surface of Mars. Provided absolute calibration is stable, surface pressure measurements on board InSight might also yield new elements on the possibility of secular pressure change on Mars caused by the interannual sublimation of the south polar residual cap. Moreover, the InSight radio-science experiment shall enable to measure variations in the length-of-day which are associated with the CO_2 sublimation / condensation cycle, and interannual variability thereof.

3. Variations of atmospheric temperature, wind and pressure on Mars have an impact on seismometers' performance and noise. On the one hand, atmosphere-induced noise will have to be filtered out (using decorrelation technique with pressure measurements) from the seismic signal related to processes and events in the Mars' interior and crust. On the other hand, seismic measurements by InSight will carry information on

   – high-frequency turbulent fluctuations, maybe permitting to reach the dissipation regime, beyond the inertial range;
   – convective cells and vortices, with an emphasis on the latter for which distant detection and retrieval of main properties will be possible, with the additional idea to use magnetic data to detect actual dust devils;

- gravity waves, for which a specific phasing between seismic and meteorological measurements is expected;
- and large-scale circulations (including thermal tides) through their impact on the seismic "hum" at low frequencies.

The seismology-driven focus of the InSight mission, as well as the limited available bandwidth to downlink data, leads to adopt an event-based data selection. To allow for atmospheric science to be studied outside events, e.g. to follow a dust storm or seasonal variations, those can be defined and monitored as Non-Event Meteorological Occurrences (NEMOs).

4. InSight will experience typical seasonal variations of dust loading in the Martian atmosphere. This will start during Entry, Descent and Landing when atmospheric profiling from 130 km altitude to the surface will be obtained at a dustier season than the other missions did. Dust opacity will be regularly measured by InSight cameras, using non-solar images of the Martian sky. Images acquired by the InSight cameras will also enable the monitoring of cloud activity, with an expected seasonal peak during the aphelion cloud belt.

5. Science campaigns with InSight will include joint studies with imagery and spectroscopy on board current operating spacecraft orbiting Mars: Mars Express, Mars Reconnaissance Orbiter, ExoMars Trace Gas Orbiter. Simultaneous measurements with the same temperature and wind sensors on board both Curiosity within Gale Crater and InSight in Elysium Planitia will help to confirm (or not) the topographical origin proposed for several unprecedented signatures detected by Curiosity.

It is our greatest hope that parts of this paper will be challenged by actual measurements carried out on board InSight. In other words, we cannot fully anticipate what the meteorological investigations on InSight will reveal (which is, admittedly, the goal of a Discovery mission). Insight will undoubtedly bring a new vision for Martian atmospheric science, that will have to be complemented in future missions by dedicated sophisticated atmospheric packages going beyond the current instruments sent to Mars.

References

D.L. Anderson, W.F. Miller, G.V. Latham, Y. Nakamura, M.N. Toksoz, A.M. Dainty, F.K. Duennebier, A.R. Lazarewicz, R.L. Kovach, T.C.D. Knight, Seismology on Mars. J. Geophys. Lett. **82**, 4524–4546 (1977)

W.B. Banerdt, S. Smrekar et al., The InSight mission. Space Sci. Rev. (2018 this issue)

D. Banfield, J.-A. Rodriguez Manfredi, C. Russell et al., The InSight auxiliary payload sensor suiteapss apss. Space Sci. Rev. (2018 this issue)

G. Bellucci, F. Altieri, J.P. Bibring, G. Bonello, Y. Langevin, B. Gondet, F. Poulet, OMEGA/Mars Express: visual channel performances and data reduction techniques. Planet. Space Sci. **54**, 675–684 (2006)

J.-P. Bibring, A. Soufflot, M. Berthé, Y. Langevin, B. Gondet, P. Drossart, M. Bouyé, M. Combes, P. Puget, A. Semery, G. Bellucci, V. Formisano, V. Moroz, V. Kottsov, G. Bonello, S. Erard, O. Forni, A. Gendrin, N. Manaud, F. Poulet, G. Poulleau, T. Encrenaz, T. Fouchet, R. Melchiori, F. Altieri, N. Ignatiev, D. Titov, L. Zasova, A. Coradini, F. Capacionni, P. Cerroni, S. Fonti, N. Mangold, P. Pinet, B. Schmitt, C. Sotin, E. Hauber, H. Hoffmann, R. Jaumann, U. Keller, R. Arvidson, J. Mustard, F. Forget, OMEGA: Observatoire pour la Minéralogie, l'Eau, les Glaces et l'Activité, in *ESA SP-1240: Mars Express: the Scientific Payload* (2004), pp. 37–49

D.G. Blackburn, K.L. Bryson, V.F. Chevrier, L.A. Roe, K.F. White, Sublimation kinetics of CO_2 ice on Mars. Planet. Space Sci. **58**, 780–791 (2010)

R.C. Blanchard, P.N. Desai, Mars Phoenix entry, descent, and landing trajectory and atmosphere reconstruction. J. Spacecr. Rockets **48**, 809–821 (2011)

N.T. Bridges, F. Ayoub, J.-P. Avouac, S. Leprince, A. Lucas, S. Mattson, Earth-like sand fluxes on Mars. Nature **485**, 339–342 (2012)

Q. Brissaud, R. Martin, R.F. Garcia, D. Komatitsch, Hybrid galerkin numerical modelling of elastodynamics and compressible Navier–Stokes couplings: applications to seismo-gravito acoustic waves. Geophys. J. Int. **210**(2), 1047–1069 (2017)

J. Businger, J. Wyngaard, Y. Izumi, E. Bradley, Flux-profile relationships in the atmospheric surface layer. J. Atmos. Sci. **28**(2), 181–189 (1971)

B.A. Cantor, MOC observations of the 2001 Mars planet-encircling dust storm. Icarus **186**, 60–96 (2007)

B.A. Cantor, P.B. James, M. Caplinger, M.J. Wolff, Martian dust storms: 1999 Mars Orbiter Camera observations. J. Geophys. Res. **106**, 23653–23688 (2001)

B.A. Cantor, P.B. James, W.M. Calvin, MARCI and MOC observations of the atmosphere and surface cap in the north polar region of Mars. Icarus **208**, 61–81 (2010)

F. Cara, G. Di Giulio, A. Rovelli, A study on seismic noise variations at Colfiorito, Central Italy: implications for the use of h/v spectral ratios. Geophys. Res. Lett. **30**(18) (2003)

T.E. Chamberlain, H.L. Cole, R.G. Dutton, G.C. Greene, J.E. Tillman, Atmospheric measurements on Mars—the Viking meteorology experiment. Bull. Am. Meteorol. Soc. **57**, 1094–1104 (1976)

D. Choi, C. Dundas, Measurements of martian dust devil winds with HiRISE. Geophys. Res. Lett. **38** (2011)

R.T. Clancy, B.J. Sandor, M.J. Woff, P.R. Christensen, M.D. Smith, J.C. Pearl, B.J. Conrath, R.J. Wilson, An intercomparison of ground-based millimeter, MGS TES, and Viking atmospheric temperature measurements: seasonal and interannual variability of temperatures and dust loading in the global Mars atmosphere. J. Geophys. Res. **105**, 9553–9571 (2000)

R.T. Clancy, M.J. Wolff, P.R. Christensen, Mars aerosol studies with the MGS TES emission phase function observations: optical depths, particle sizes, and ice cloud types versus latitude and solar longitude. J. Geophys. Res., Planets **108**(E9), 1–2 (2003)

J.F. Clinton, D. Giardini, P. Lognonné, B. Banerdt, M. van Driel, M. Drilleau, N. Murdoch, M. Panning, R. Garcia, D. Mimoun, M. Golombek, J. Tromp, R. Weber, M. Böse, S. Ceylan, I. Daubar, B. Kenda, A. Khan, L. Perrin, A. Spiga, Preparing for InSight: an invitation to participate in a blind test for martian seismicity. Seismol. Res. Lett. **88**, 1290–1302 (2017)

J. Clinton et al., Marsquake service—building a martian seismicity catalogue for InSight. Space Sci. Rev. (2018 this issue)

A. Colaïtis, A. Spiga, F. Hourdin, C. Rio, F. Forget, E. Millour, A thermal plume model for the Martian convective boundary layer. J. Geophys. Res., Planets **118**, 1468–1487 (2013)

D.S. Colburn, J.B. Pollack, R.M. Haberle, Diurnal variations in optical depth at Mars. Icarus **79**, 159–189 (1989)

M. Collins, S.R. Lewis, P.L. Read, F. Hourdin, Baroclinic wave transitions in the Martian atmosphere. Icarus **120**, 344–357 (1996)

I. Daubar, M. Golombek, S. Smrekar, W. Banerdt et al., Impact studies with InSight. Space Sci. Rev. (2018 this issue)

R. Davy, J.A. Davis, P.A. Taylor, C.F. Lange, W. Weng, J. Whiteway, H.P. Gunnlaugson, Initial analysis of air temperature and related data from the phoenix met station and their use in estimating turbulent heat fluxes. J. Geophys. Res., Planets **115**(E3), E00E13 (2010)

V. Dehant, W. Folkner, E. Renotte, D. Orban, S. Asmar, G. Balmino, J. Barriot, J. Benoist, R. Biancale, J. Biele, F. Budnik, S. Burger, O. de Viron, B. Häusler, Ö. Karatekin, S. Le Maistre, P. Lognonné, M. Menvielle, M. Mitrovic, M. Pätzold, A. Rivoldini, P. Rosenblatt, G. Schubert, T. Spohn, P. Tortora, T. van Hoolst, O. Witasse, M. Yseboodt, Lander radioscience for obtaining the rotation and orientation of Mars. Planet. Space Sci. **57**, 1050–1067 (2009)

V. Dehant, S. Le Maistre, A. Rivoldini, M. Yseboodt, P. Rosenblatt, T. Van Hoolst, M. Mitrovic, Ö. Karatekin, J. Marty, A. Chicarro, Revealing mars' deep interior: future geodesy missions using radio links between landers, orbiters, and the Earth. Planet. Space Sci. **59**, 1069–1081 (2011)

P. Delage, F. Karakostas, A. Dhemaied, M. Belmokhtar, P. Lognonné, M. Golombek, E. De Laure, K. Hurst, J.-C. Dupla, S. Kedar, Y.J. Cui, B. Banerdt, An Investigation of the mechanical properties of some Martian regolith simulants with respect to the surface properties at the InSight mission landing site. Space Sci. Rev. **211**, 191–213 (2017)

P.S. du Courrech, C. Narteau, X. Gao, Two modes for dune orientation. Geology **42**, 743–746 (2014)

C.W. Ebeling, Inferring ocean storm characteristics from ambient seismic noise: a historical perspective, in *Advances in Geophysics*, ed. by R. Dmowska. Advances in Geophysics, vol. 53 (Elsevier, Amsterdam, 2012), pp. 1–33

M.D. Ellehoj, H.P. Gunnlaugsson, P.A. Taylor, H. Kahanpää, K.M. Bean, B.A. Cantor, B.T. Gheynani, L. Drube, D. Fisher, A.-M. Harri, C. Holstein-Rathlou, M.T. Lemmon, M.B. Madsen, M.C. Malin, J. Polkko, P.H. Smith, L.K. Tamppari, W. Weng, J. Whiteway, Convective vortices and dust devils at the Phoenix Mars mission landing site. J. Geophys. Res., Planets **115**(E14), E00E16 (2010)

M. Farrell, P.H. Smith, G.T. Delory, G. Hillard, J.R. Marshall, D. Catling, M. Hecht, D.M. Tratt, N. Renno, M.D. Desch, S. Cummer, J.G. Houser, B. Johnson, Electric and magnetic signatures of dust devils from the 2000–2001 matador desert tests. J. Geophys. Res. **109** (2004)

L. Fenton, T.I. Michaels, Characterizing the sensitivity of daytime turbulent activity on Mars with the MRAMS LES: early results. Mars Int. J. Mars Sci. Explor. **5**, 159–171 (2010)

F. Ferri, P.H. Smith, M. Lemmon, N.O. Rennó, Dust devils as observed by Mars Pathfinder. J. Geophys. Res., Planets **108**, 5133 (2003)

F. Ferri, O. Karatekin, S. Lewis et al., Exomars atmospheric mars entry and landing investigations and analysis (amelia). Space Sci. Rev. (2018 this issue)

T. Foken, 50 years of the Monin–Obukhov similarity theory. Bound.-Layer Meteorol. **119**(3), 431–447 (2006)

W.M. Folkner, C.F. Yoder, D.N. Yuan, E.M. Standish, R.A. Preston, Interior structure and seasonal mass redistribution of Mars from radio tracking of Mars Pathfinder. Science **278**, 1749–1751 (1997)

W.M. Folkner, V. Dehant, S. Le Maistre, M. Yseboodt, A. Rivoldini, T. Van Hoolst, S.W. Asmar, M.P. Golombek, The rotation and interior structure experiment on the InSight mission to Mars. Space Sci. Res. **214**(5), 100 (2018). https://doi.org/10.1007/s11214-018-0530-5

F. Forget, F. Hourdin, R. Fournier, C. Hourdin, O. Talagrand, M. Collins, S.R. Lewis, P.L. Read, J.-P. Huot, Improved general circulation models of the Martian atmosphere from the surface to above 80 km. J. Geophys. Res. **104**, 24155–24176 (1999)

F. Forget, A. Spiga, B. Dolla, S. Vinatier, R. Melchiorri, P. Drossart, A. Gendrin, J.-P. Bibring, Y. Langevin, B. Gondet, Remote sensing of surface pressure on Mars with the Mars Express/OMEGA spectrometer, 1: retrieval method. J. Geophys. Res., Planets **112**(E11), 8 (2007)

D. Fritts, M. Alexander, Gravity wave dynamics and effects in the middle atmosphere. Rev. Geophys. **41**(1), 1003 (2003)

S.G. Fryberger, G. Dean, Dune forms and wind regime, in *A Study of Global Sand Seas*, ed. by E.D. McKee. Geological Survey Professional Paper, vol. 1052 (United States Government Printing Office, New York, 1979), pp. 137–169

X. Gao, C. Narteau, O. Rozier, P.S. du Courrech, Phase diagrams of dune shape and orientation depending on sand availability. Sci. Rep. **5**, 14677 (2015)

R.F. Garcia, Q. Brissaud, L. Rolland, R. Martin, D. Komatitsch, A. Spiga, P. Lognonné, B. Banerdt, Finite-difference modeling of acoustic and gravity wave propagation in Mars atmosphere: application to infra-sounds emitted by meteor impacts. Space Sci. Rev. **211**, 547–570 (2017)

J.R. Garratt, *The Atmospheric Boundary Layer* (Cambridge Univ. Press, New York, 1992)

I. Gaudot, E. Beucler, A. Mocquet, M. Schimmel, M. Le Feuvre, Statistical redundancy of instantaneous phases: theory and application to the seismic ambient wavefield. Geophys. J. Int. **204**(2), 1159–1163 (2016)

P. Gentine, G.-J. Steeneveld, B.G. Heusinkveld, A.A. Holtslag, Coupling between radiative flux divergence and turbulence near the surface. Q. J. R. Meteorol. Soc. (2018)

M. Giuranna, V. Formisano, D. Biondi, A. Ekonomov, S. Fonti, D. Grassi, H. Hirsch, I. Khatuntsev, N. Ignatiev, M. Malgoska, A. Mattana, A. Maturilli, E. Mencarelli, F. Nespoli, R. Orfei, P. Orleanski, G. Piccioni, M. Rataj, B. Saggin, L. Zasova, Calibration of the Planetary Fourier Spectrometer long wavelength channel. Planet. Space Sci. **53**, 993–1007 (2005)

N.R. Goins, A.R. Lazarewicz, Martian seismicity. Geophys. Res. Lett. **6**, 368–370 (1979)

M. Golombek, D. Kipp, N. Warner, I.J. Daubar, R. Fergason, R.L. Kirk, R. Beyer, A. Huertas, S. Piqueux, N.E. Putzig, B.A. Campbell, G.A. Morgan, C. Charalambous, W.T. Pike, K. Gwinner, F. Calef, D. Kass, M. Mischna, J. Ashley, C. Bloom, N. Wigton, T. Hare, C. Schwartz, H. Gengl, L. Redmond, M.

Trautman, J. Sweeney, C. Grima, I.B. Smith, E. Sklyanskiy, M. Lisano, J. Benardini, S. Smrekar, P. Lognonné, W.B. Banerdt, Selection of the InSight landing site. Space Sci. Rev. **211**, 5–95 (2017)

M. Golombek, M. Grott, G. Kargl, J. Andrade, J. Marshall, N. Warner, N.A. Teanby, V. Ansan, E. Hauber, J. Voigt, R. Lichtenheldt, B. Knapmeyer-Endrun, I.J. Daubar, D. Kipp, N. Muller, P. Lognonné, C. Schmelzbach, D. Banfield, A. Trebi-Ollennu, J. Maki, S. Kedar, D. Mimoun, N. Murdoch, S. Piqueux, P. Delage, W.T. Pike, C. Charalambous, R. Lorenz, L. Fayon, A. Lucas, S. Rodriguez, P. Morgan, A. Spiga, M. Panning, T. Spohn, S. Smrekar, T. Gudkova, R. Garcia, D. Giardini, U. Christensen, T. Nicollier, D. Sollberger, J. Robertsson, K. Ali, B. Kenda, W.B. Banerdt, Geology and physical properties investigations by the InSight lander. Space Sci. Rev. **214**(5), 84 (2018). https://doi.org/10.1007/s11214-018-0512-7

J. Gómez-Elvira, C. Armiens, L. Castañer, M. Domínguez, M. Genzer, F. Gómez, R. Haberle, A.-M. Harri, V. Jiménez, H. Kahanpää, L. Kowalski, A. Lepinette, J. Martín, J. Martínez-Frías, I. McEwan, L. Mora, J. Moreno, S. Navarro, M.A. de Pablo, V. Peinado, A. Peña, J. Polkko, M. Ramos, N.O. Renno, J. Ricart, M. Richardson, J. Rodríguez-Manfredi, J. Romeral, E. Sebastián, J. Serrano, M. de la Torre Juárez, J. Torres, F. Torrero, R. Urquí, L. Vázquez, T. Velasco, J. Verdasca, M.-P. Zorzano, J. Martín-Torres, REMS: the Environmental Sensor Suite for the Mars Science Laboratory Rover. Space Sci. Rev. **170**, 583–640 (2012)

J. Gómez-Elvira, C. Armiens, I. Carrasco, M. Genzer, F. Gómez, R. Haberle, V.E. Hamilton, A.-M. Harri, H. Kahanpää, O. Kemppinen, A. Lepinette, J. Martín Soler, J. Martín-Torres, J. Martínez-Frías, M. Mischna, L. Mora, S. Navarro, C. Newman, M.A. de Pablo, V. Peinado, J. Polkko, S.C.R. Rafkin, M. Ramos, N.O. Rennó, M. Richardson, J.A. Rodríguez-Manfredi, J.J. Romeral Planelló, E. Sebastián, M. de la Torre Juárez, J. Torres, R. Urquí, A.R. Vasavada, J. Verdasca, M.-P. Zorzano, Curiosity's rover environmental monitoring station: overview of the first 100 sols. J. Geophys. Res., Planets **119**(7), 1680–1688 (2014). 2013JE004576

F. González-Galindo, A. Määttänen, F. Forget, A. Spiga, The martian mesosphere as revealed by CO_2 clouds observations and general circulation modeling. Icarus **216**, 10–22 (2011)

E.E. Gossard, W.H. Hooke, *Waves in the Atmosphere: Atmospheric Infrasound and Gravity Waves—Their Generation and Propagation*, 1st edn. Developments in Atmospheric Science, vol. 2 (Elsevier, Amsterdam, 1975)

E. Gossard, W. Munk, On gravity waves in the atmosphere. J. Meteorol. **11**(4), 259–269 (1954)

R. Greeley, P.L. Whelley, R.E. Arvidson, N.A. Cabrol, D.J. Foley, B.J. Franklin, P.G. Geissler, M.P. Golombek, R.O. Kuzmin, G.A. Landis, M.T. Lemmon, L.D.V. Neakrase, S.W. Squyres, S.D. Thompson, Active dust devils in Gusev crater, Mars: observations from the Mars Exploration Rover Spirit. J. Geophys. Res., Planets **111**(E10), 12 (2006)

R. Greeley, D.A. Waller, N.A. Cabrol, G.A. Landis, M.T. Lemmon, L.D.V. Neakrase, M. Pendleton Hoffer, S.D. Thompson, P.L. Whelley, Gusev Crater, Mars: observations of three dust devil seasons. J. Geophys. Res., Planets **115**, E00F02 (2010)

S.D. Guzewich, A.D. Toigo, M.I. Richardson, C.E. Newman, E.R. Talaat, D.W. Waugh, T.H. McConnochie, The impact of a realistic vertical dust distribution on the simulation of the Martian general circulation. J. Geophys. Res., Planets **118**, 980–993 (2013)

S.D. Guzewich, C.E. Newman, M. de la Torre Juárez, R.J. Wilson, M. Lemmon, M.D. Smith, H. Kahanpää, A.-M. Harri, Atmospheric tides in Gale Crater, Mars. Icarus **268**, 37–49 (2016)

S.D. Guzewich, C.E. Newman, M.D. Smith, J.E. Moores, C.L. Smith, C. Moore, M.I. Richardson, D. Kass, A. Kleinböhl, M. Mischna, F.J. Martín-Torres, M.-P. Zorzano-Mier, M. Battalio, The vertical dust profile over Gale crater, Mars. J. Geophys. Res., Planets **122**(12), 2779–2792 (2017)

S.D. Guzewich, A.D. Toigo, H. Wang, An investigation of dust storms observed with the Mars Color Imager. Icarus **289**, 199–213 (2017)

R.M. Haberle, M.A. Kahre, Detecting secular climate change on Mars. Mars Int. J. Mars Sci. Explor. **5**, 68–75 (2010)

R.M. Haberle, J. Gómez-Elvira, M. Torre Juárez, A.-M. Harri, J.L. Hollingsworth, H. Kahanpää, M.A. Kahre, M. Lemmon, F.J. Martín-Torres, M. Mischna, J.E. Moores, C. Newman, S.C.R. Rafkin, N. Rennó, M.I. Richardson, J.A. Rodríguez-Manfredi, A.R. Vasavada, M.-P. Zorzano-Mier, Preliminary interpretation of the REMS pressure data from the first 100 sols of the MSL mission. J. Geophys. Res., Planets **119**, 440–453 (2014)

R.M. Haberle, R.T. Clancy, F. Forget, M.D. Smith, R.W. Zurek, *The Atmosphere and Climate of Mars*, vol. 18 (Cambridge Univ. Press, London, 2017)

R.M. Haberle, M.D.L.T.Juárez, M.A. Kahre, D.M. Kass, J.R. Barnes, J.L. Hollingsworth, A.-M. Harri, H. Kahanpää, Detection of northern hemisphere transient eddies at Gale crater Mars. Icarus **307**, 150–160 (2018)

V.E. Hamilton, A.R. Vasavada, E. Sebastián, M. Torre Juárez, M. Ramos, C. Armiens, R.E. Arvidson, I. Carrasco, P.R. Christensen, M.A. De Pablo, W. Goetz, J. Gómez-Elvira, M.T. Lemmon, M.B. Madsen, F.J.

Martín-Torres, J. Martínez-Frías, A. Molina, M.C. Palucis, S.C.R. Rafkin, M.I. Richardson, R.A. Yingst, M.-P. Zorzano, Observations and preliminary science results from the first 100 sols of MSL Rover Environmental Monitoring Station ground temperature sensor measurements at Gale Crater. J. Geophys. Res., Planets **119**, 745–770 (2014)

A. Haned, E. Stutzmann, M. Schimmel, S. Kiselev, A. Davaille, A. Yelles-Chaouche, Global tomography using seismic hum. Geophys. J. Int. **204**(2), 1222–1236 (2016)

A.-M. Harri, M. Genzer, O. Kemppinen, H. Kahanpää, J. Gomez-Elvira, J.A. Rodriguez-Manfredi, R. Haberle, J. Polkko, W. Schmidt, H. Savijärvi, J. Kauhanen, E. Atlaskin, M. Richardson, T. Siili, M. Paton, M. de la Torre Juarez, C. Newman, S. Rafkin, M.T. Lemmon, M. Mischna, S. Merikallio, H. Haukka, J. Martin-Torres, M.-P. Zorzano, V. Peinado, R. Urqui, A. Lapinette, A. Scodary, T. Mäkinen, L. Vazquez, N. Rennó (The REMS/MSL Science Team), Pressure observations by the curiosity rover: initial results. J. Geophys. Res., Planets **119**(1), 82–92 (2014)

N.G. Heavens, M.I. Richardson, A. Kleinböhl, D.M. Kass, D.J. McCleese, W. Abdou, J.L. Benson, J.T. Schofield, J.H. Shirley, P.M. Wolkenberg, Vertical distribution of dust in the Martian atmosphere during northern spring and summer: high-altitude tropical dust maximum at northern summer solstice. J. Geophys. Res., Planets **116**(E15), E01007 (2011)

N.G. Heavens, M.S. Johnson, W.A. Abdou, D.M. Kass, A. Kleinböhl, D.J. McCleese, J.H. Shirley, R.J. Wilson, Seasonal and diurnal variability of detached dust layers in the tropical Martian atmosphere. J. Geophys. Res., Planets **119**, 1748–1774 (2014)

E. Hébrard, C. Listowski, P. Coll, B. Marticorena, G. Bergametti, A. Määttänen, F. Montmessin, F. Forget, An aerodynamic roughness length map derived from extended martian rock abundance data. J. Geophys. Res. **117**(E4), E04008 (2012)

S.L. Hess, J.A. Ryan, J.E. Tillman, R.M. Henry, C.B. Leovy, The annual cycle of pressure on Mars measured by Viking landers 1 and 2. Geophys. Res. Lett. **7**, 197–200 (1980)

D.P. Hinson, M. Pätzold, S. Tellmann, B. Häusler, G.L. Tyler, The depth of the convective boundary layer on Mars. Icarus **198**, 57–66 (2008)

U. Högström, Review of some basic characteristics of the atmospheric surface layer. Bound.-Layer Meteorol. **78**(3), 215–246 (1996)

J.L. Hollingsworth, R.M. Haberle, J. Barnes, A.F.C. Bridger, J.B. Pollack, H. Lee, J. Schaeffer, Orographic control of storm zones on Mars. Nature **380**, 413–416 (1996)

C. Holstein-Rathlou, A. Maue, P. Withers, Atmospheric studies from the Mars Science Laboratory entry, descent and landing atmospheric structure reconstruction. Planet. Space Sci. **120**, 15–23 (2016)

F. Hourdin, P. Le Van, F. Forget, O. Talagrand, Meteorological variability and the annual surface pressure cycle on Mars. J. Atmos. Sci. **50**, 3625–3640 (1993)

T. Imamura, A. Watanabe, Y. Maejima, Convective generation and vertical propagation of fast gravity waves on Mars: one- and two-dimensional modeling. Icarus **267**, 51–63 (2016)

P.S. Jackson, J.C.R. Hunt, Turbulent wind flow over a low hill. Q. J. R. Meteorol. Soc. **101**, 929–955 (1975)

R. Jaumann, G. Neukum, T. Behnke, T.C. Duxbury, K. Eichentopf, J. Flohrer, S.V. Gasselt, B. Giese, K. Gwinner, E. Hauber, H. Hoffmann, A. Hoffmeister, U. Köhler, K.-D. Matz, T.B. McCord, V. Mertens, J. Oberst, R. Pischel, D. Reiss, E. Ress, T. Roatsch, P. Saiger, F. Scholten, G. Schwarz, K. Stephan, M. Wählisch (the HRSC Co-Investigator Team), The high-resolution stereo camera (HRSC) experiment on Mars Express: instrument aspects and experiment conduct from interplanetary cruise through the nominal mission. Planet. Space Sci. **55**, 928–952 (2007)

H. Kahanpää, C. Newman, J. Moores, M.-P. Zorzano, J. Martín-Torres, S. Navarro, A. Lepinette, B. Cantor, M.T. Lemmon, P. Valentín-Serrano, A. Ullán, W. Schmidt, Convective vortices and dust devils at the MSL landing site: annual variability. J. Geophys. Res., Planets **121**, 1514–1549 (2016)

M.A. Kahre, J.R. Murphy, R.M. Haberle, Modeling the Martian dust cycle and surface dust reservoirs with the NASA Ames general circulation model. J. Geophys. Res., Planets **111**(E10), 6008 (2006)

K.M. Kanak, On the numerical simulation of dust devil-like vortices in terrestrial and Martian convective boundary layers. Geophys. Res. Lett. **33**, 19 (2006)

ö. Karatekin, L. Montabone, Atmospheric angular momentum and rotation variations of Mars between Martian years 24 and 27, in *Mars Atmosphere: Modelling and Observation, 5th International Workshop*, ed. by F. Forget, M. Millour (2014)

Ö. Karatekin, O. de Viron, S. Lambert, V. Dehant, P. Rosenblatt, T. van Hoolst, S. Le Maistre, Atmospheric angular momentum variations of Earth, Mars and Venus at seasonal time scales. Planet. Space Sci. **59**, 923–933 (2011)

ö. Karatekin, V. Dehant, W.M. Folkner, S. Le Maistre, S. Asmar, A. Konopliv, Radioscience experiment to monitor atmospheric angular momentum variations onboard the forthcoming 2018 InSight and 2020 ExoMars Rovers, in *Mars Atmosphere: Modelling and Observation, 6th International Workshop*, ed. by F. Forget, M. Millour (2017)

D.M. Kass, J.T. Schofield, T.I. Michaels, S.C.R. Rafkin, M.I. Richardson, A.D. Toigo, Analysis of atmospheric mesoscale models for entry, descent, and landing. J. Geophys. Res., Planets **108**, 8090 (2003)

S. Kedar, J. Andrade, W. Banerdt, P. Delage, M. Golombek, M. Grott, T. Hudson, A. Kiely, M. Knapmeyer, B. Knapmeyer-Endrun, C. Krause, T. Kawamura, P. Lognonné, T. Pike, Y. Ruan, T. Spohn, N. Teanby, J. Tromp, J. Wookey, Analysis of regolith properties using seismic signals generated by InSight's hp3 penetrator. Space Sci. Rev. (2017)

B. Kenda, P. Lognonné, A. Spiga, T. Kawamura, S. Kedar, W.B. Banerdt, R. Lorenz, D. Banfield, M. Golombek, Modeling of ground deformation and shallow surface waves generated by martian dust devils and perspectives for near-surface structure inversion. Space Sci. Rev. (2017)

A. Kleinböhl, J.T. Schofield, D.M. Kass, W.A. Abdou, C.R. Backus, B. Sen, J.H. Shirley, W.G. Lawson, M.I. Richardson, F.W. Taylor, N.A. Teanby, D.J. McCleese, Mars Climate Sounder limb profile retrieval of atmospheric temperature, pressure, and dust and water ice opacity. J. Geophys. Res., Planets **114**, 10006 (2009)

B. Knapmeyer-Endrun, P. Golombek M, M. Ohrnberger, Rayleigh wave ellipticity modeling and inversion for shallow structure at the proposed insight landing site in Elysium planitia, Mars. Space Sci. Rev. (2016)

N. Kobayashi, K. Nishida, Continuous excitation of planetary free oscillations by atmospheric disturbances. Nature **395**, 357–360 (1998)

A.S. Konopliv, S.W. Asmar, W.M. Folkner, Ö. Karatekin, D.C. Nunes, S.E. Smrekar, C.F. Yoder, M.T. Zuber, Mars high resolution gravity fields from MRO, Mars seasonal gravity, and other dynamical parameters. Icarus **211**, 401–428 (2011)

O. Korablev, F. Montmessin, A. Trokhimovskiy, A.A. Fedorova, A.V. Shakun, A.V. Grigoriev, B.E. Moshkin, N.I. Ignatiev, F. Forget, F. Lefèvre, K. Anufreychik, I. Dzuban, Y.S. Ivanov, Y.K. Kalinnikov, T.O. Kozlova, A. Kungurov, V. Makarov, F. Martynovich, I. Maslov, D. Merzlyakov, P.P. Moiseev, Y. Nikolskiy, A. Patrakeev, D. Patsaev, A. Santos-Skripko, O. Sazonov, N. Semena, A. Semenov, V. Shashkin, A. Sidorov, A.V. Stepanov, I. Stupin, D. Timonin, A.Y. Titov, A. Viktorov, A. Zharkov, F. Altieri, G. Arnold, D.A. Belyaev, J.L. Bertaux, D.S. Betsis, N. Duxbury, T. Encrenaz, T. Fouchet, J.-C. Gérard, D. Grassi, S. Guerlet, P. Hartogh, Y. Kasaba, I. Khatuntsev, V.A. Krasnopolsky, R.O. Kuzmin, E. Lellouch, M.A. Lopez-Valverde, M. Luginin, E. Marcq, J. Martin Torres, A.S. Medvedev, E. Millour, K.S. Olsen, M.R. Patel, C. Quantin-Nataf, A.V. Rodin, V.I. Shematovich, I. Thomas, N. Thomas, L. Vazquez, M. Vincendon, V. Wilquet, C.F. Wilson, L.V. Zasova, L.M. Zelenyi, M.P. Zorzano, The Atmospheric Chemistry Suite (ACS) of three spectrometers for the ExoMars 2016 Trace Gas Orbiter. Space Sci. Rev. **214**(7) (2018)

P. Kuchynka, W.M. Folkner, A.S. Konopliv, R.S. Park, S. Le Maistre, V. Dehant, New constraints on Mars rotation determined from radiometric tracking of the Opportunity Mars Exploration Rover. Icarus **229**, 340–347 (2014)

M.V. Kurgansky, L. Baez, E.M. Ovalle, A simple model of the magnetic emission from a dust devil. J. Geophys. Res., Planets **112**(E11), E11008 (2007)

S.E. Larsen, H.E. Jørgensen, L. Landberg, e. al, Aspects of the atmospheric surface layers on Mars and Earth. Bound.-Layer Meteorol. **105**, 451–470 (2002)

S. Le Maistre, P. Rosenblatt, A. Rivoldini, V. Dehant, J.-C. Marty, Ö. Karatekin, Lander radio science experiment with a direct link between Mars and the Earth. Planet. Space Sci. **68**(1), 105–122 (2012)

M.T. Lemmon, M.J. Wolff, M.D. Smith, R.T. Clancy, D. Banfield, G.A. Landis, A. Ghosh, P.H. Smith, N. Spanovich, B. Whitney, P. Whelley, R. Greeley, S. Thompson, J.F. Bell, S.W. Squyres, Atmospheric imaging results from the Mars Exploration Rovers: spirit and opportunity. Science **306**, 1753–1756 (2004)

M.T. Lemmon, M.J. Wolff, J.F. Bell III., M.D. Smith, B.A. Cantor, P.H. Smith, Dust aerosol, clouds, and the atmospheric optical depth record over 5 Mars years of the Mars Exploration Rover mission. Icarus **251**, 96–111 (2015)

S.R. Lewis, P.R. Barker, Atmospheric tides in a Mars general circulation model with data assimilation. Adv. Space Res. **36**, 2162–2168 (2005)

S.R. Lewis, D.P. Mulholland, P.L. Read, L. Montabone, R.J. Wilson, M.D. Smith, The solstitial pause on Mars, 1: a planetary wave reanalysis. Icarus **264**, 456–464 (2016)

D. Li, G.G. Katul, S.S. Zilitinkevich, Revisiting the turbulent prandtl number in an idealized atmospheric surface layer. J. Atmos. Sci. **72**(6), 2394–2410 (2015)

D.K. Lilly, On the numerical simulation of buoyant convection. Tellus **14**(2), 148–172 (1962)

P. Lognonné, B. Mosser, Planetary seismology. Surv. Geophys. **14**, 239–302 (1993)

P. Lognonné, E. Clévédé, H. Kanamori, Computation of seismograms and atmospheric oscillations by normal-mode summation for a spherical earth model with realistic atmosphere. Geophys. J. Int. **135**, 388–406 (1998)

P. Lognonné, F. Karakostas, L. Rolland, Y. Nishikawa, Modeling of atmospheric-coupled Rayleigh waves on planets with atmosphere: from Earth observation to Mars and Venus perspectives. J. Acoust. Soc. Am. **140**(2) (2016)

P. Lognonné, W.B. Banerdt, D. Giardini, W.T. Pike et al., SEIS: the seismic experiment for internal structure of InSight. Space Sci. Rev. (2018 this issue)

R.D. Lorenz, Observing desert dust devils with a pressure logger. Geosci. Instrum. Methods Data Syst. **2**(2), 477–505 (2012)

R.D. Lorenz, Heuristic estimation of dust devil vortex parameters and trajectories from single-station meteorological observations: application to insight at Mars. Icarus **271**, 326–337 (2016)

R.D. Lorenz, D. Christie, Dust devil signatures in infrasound records of the international monitoring system. Geophys. Res. Lett. **42**(6), 2009–2014 (2015)

R.D. Lorenz, S. Kedar, N. Murdoch, P. Lognonné, T. Kawamura, D. Mimoun, W.B. Banerdt, Seismometer detection of dust devil vortices by ground tilt. Bull. Seismol. Soc. Am. (2015)

R.D. Lorenz, Y. Nakamura, J.R. Murphy, Viking-2 seismometer measurements on mars: Pds data archive and meteorological applications. Earth Space Sci. **4**(11), 681–688 (2017)

A. Lucas, C. Narteau, S. Rodriguez, O. Rozier, Y. Callot, A. Garcia, P.S. du Courrech, Sediment flux from the morphodynamics of elongating linear dunes. Geology **43**, 1027–1030 (2015)

A. Määttänen, H. Savijärvi, Sensitivity tests with a one-dimensional boundary-layer Mars model. Bound.-Layer Meteorol. **113**(3), 305–320 (2004)

A. Määttänen, T. Fouchet, O. Forni, R. Melchiorri, F. Forget, H. Savijarvi, J.P. Bibring, Y. Langevin, B. Gondet, V. Formisano, M. Giuranna, A study of the properties of a local dust storm with Mars Express OMEGA and PFS data. Icarus **201**(2), 504–516 (2009)

A. Määttänen, F. Montmessin, B. Gondet, F. Scholten, H. Hoffmann, F. González-Galindo, A. Spiga, F. Forget, E. Hauber, G. Neukum, J. Bibring, J. Bertaux, Mapping the mesospheric CO_2 clouds on Mars: MEx/OMEGA and MEx/HRSC observations and challenges for atmospheric models. Icarus **209**, 452–469 (2010)

J.-B. Madeleine, F. Forget, E. Millour, L. Montabone, M.J. Wolff, Revisiting the radiative impact of dust on Mars using the LMD global climate model. J. Geophys. Res., Planets **116**, 11010 (2011)

J.-B. Madeleine, F. Forget, A. Spiga, M.J. Wolff, F. Montmessin, M. Vincendon, D. Jouglet, B. Gondet, J.-P. Bibring, Y. Langevin, B. Schmitt, Aphelion water-ice cloud mapping and property retrieval using the OMEGA imaging spectrometer onboard Mars Express. J. Geophys. Res., Planets **117**(E16) (2012)

J.A. Magalhaes, J.T. Schofield, A. Seiff, Results of the Mars Pathfinder atmospheric structure investigation. J. Geophys. Res. **104**, 8943–8956 (1999)

J.N. Maki, M. Golombek, R. Deen, H. Abarca, C. Sorice, T. Goodsall, M. Schwochert, M. Lemmon, A. Trebi-Ollennu, W.B. Banerdt, The color cameras on the InSight lander. Space sci. Rev. **214**(6), 105 (2018). https://doi.org/10.1007/s11214-018-0536-z

M.C. Malin, A. Caplinger, S.D. Davis, Observational evidence for an active surface reservoir of solid carbon dioxide on mars. Science **294**(5549), 2146–2148 (2001)

M. Malin, J. Bell, B. Cantor, M.A. Caplinger, W. Calvin, R. Clancy, K. Edgett, L. Edwards, R. Haberle, P. James, S. Lee, M. Ravine, P. Thomas, M. Wolff, Context Camera Investigation on board the Mars Reconnaissance Orbiter. J. Geophys. Res. **112** (2007)

M.C. Malin, W.M. Calvin, B.A. Cantor, R.T. Clancy, R.M. Haberle, P.B. James, P.C. Thomas, M.J. Wolff, J.F. Bell, S.W. Lee, Climate, weather, and north polar observations from the Mars Reconnaissance Orbiter Mars Color Imager. Icarus **194**, 501–512 (2008)

M.C. Malin, B.A. Cantor, A.W. Britton, Mro marci weather report for the week of 4 June 2018–10 June 2018. Malin Space Science Systems Captioned Image Release, MSSS-534 (2018). http://www.msss.com/msss_images/2018/06/13/

L.J. Martin, R.W. Zurek, An analysis of the history of dust activity on Mars. J. Geophys. Res. **98**(E2), 3221–3246 (1993)

G. Martínez, F. Valero, L. Vázquez, Characterization of the Martian Surface Layer. J. Atmos. Sci. **66**, 187–198 (2009)

G.M. Martínez, C.N. Newman, A. De Vicente-Retortillo, E. Fischer, N.O. Renno, M.I. Richardson, A.G. Fairén, M. Genzer, S.D. Guzewich, R.M. Haberle, A.-M. Harri, O. Kemppinen, M.T. Lemmon, M.D. Smith, M. de la Torre-Juárez, A.R. Vasavada, The modern near-surface martian climate: a review of in-situ meteorological data from Viking to curiosity. Space Sci. Rev. **212**(1), 295–338 (2017)

P. Mason, Large-eddy simulation of the convective atmospheric boundary layer. J. Atmos. Sci. **46**(11), 1492–1516 (1989)

A. McEwen, L. Tornabene, H. Team, E. Eliason, J. Bergstrom, N. Bridges, C. Hansen, W. Delamere, J. Grant, V. Gulick, K. Herkenhoff, L. Keszthelyi, R. Kirk, M. Mellon, S.W. Squyres, N. Thomas, C. Weitz, Mars Reconnaissance Orbiter's High Resolution Imaging Science Experiment (HiRISE). J. Geophys. Res. **112** (2007)

D. McNamara, R. Buland, Ambient noise levels in the continental United States. Bull. Seismol. Soc. Am. **94**, 1517–1527 (2004)

S.M. Metzger, J.R. Carr, J.R. Johnson, T.J. Parker, M.T. Lemmon, Dust devil vortices seen by the Mars Pathfinder camera. Geophys. Res. Lett. **26**, 2781–2784 (1999)

T.I. Michaels, S.C.R. Rafkin, Large eddy simulation of atmospheric convection on Mars. Q. J. R. Meteorol. Soc. **130**, 1251–1274 (2004)

E. Millour, F. Forget, A. Spiga, T. Navarro, J.-B. Madeleine, L. Montabone, F. Lefevre, J.-Y. Chaufray, M.A. Lopez-Valverde, F. Gonzalez-Galindo, S.R. Lewis, P.L. Read, M.-C. Desjean, J.-P. Huot (MCD/GCM Development Team), The Mars climate database (MCD version 5.1), in *Eighth International Conference on Mars*. LPI Contributions, vol. 1791 (2014), p. 1184

E. Millour, F. Forget, A. Spiga, T. Navarro, J.-B. Madeleine, L. Montabone, A. Pottier, F. Lefevre, F. Montmessin, J.-Y. Chaufray, M.A. Lopez-Valverde, F. Gonzalez-Galindo, S.R. Lewis, P.L. Read, J.-P. Huot, M.-C. Desjean (MCD/GCM Development Team), The Mars climate database (MCD version 5.2), in *European Planetary Science Congress* (2015), p. 10

D. Mimoun, N. Murdoch, P. Lognonné, K. Hurst, W.T. Pike, J. Hurley, T. Nébut, W.B. Banerdt, S. Team, The noise model of the seis seismometer of the insight mission to Mars. Space Sci. Rev. (2017)

A.S. Monin, A.M. Obukhov, Osnovnye zakonomernosti turbulentnogo peremeshivanija v prizemnom sloe atmosfery (Basic laws of turbulent mixing in the atmosphere near the ground). Trudy Geofiz. Inst. AN SSSR **24**, 163–187 (1954)

L. Montabone, S.R. Lewis, P.L. Read, Interannual variability of Martian dust storms in assimilation of several years of Mars global surveyor observations. Adv. Space Res. **36**, 2146–2155 (2005)

L. Montabone, F. Forget, E. Millour, R.J. Wilson, S.R. Lewis, B. Cantor, D. Kass, A. Kleinböhl, M.T. Lemmon, M.D. Smith, M.J. Wolff, Eight-year climatology of dust optical depth on Mars. Icarus **251**, 65–95 (2015)

J.E. Moores, M.T. Lemmon, P.H. Smith, L. Komguem, J.A. Whiteway, Atmospheric dynamics at the Phoenix landing site as seen by the Surface Stereo Imager. J. Geophys. Res., Planets **115**, E00E08 (2010)

J.E. Moores, M.T. Lemmon, H. Kahanpää, S.C.R. Rafkin, R. Francis, J. Pla-Garcia, K. Bean, R. Haberle, C. Newman, M. Mischna, A.R. Vasavada, M. de la Torre Juárez, N. Rennó, J. Bell, F. Calef, B. Cantor, T.H. Mcconnochie, A.-M. Harri, M. Genzer, M.H. Wong, M.D. Smith, F.J. Martín-Torres, M.-P. Zorzano, O. Kemppinen, E. McCullough, Observational evidence of a suppressed planetary boundary layer in northern Gale Crater, Mars as seen by the Navcam instrument onboard the Mars Science Laboratory rover. Icarus **249**, 129–142 (2015a)

J.E. Moores, M.T. Lemmon, S.C.R. Rafkin, R. Francis, J. Pla-Garcia, M. de la Torre Juárez, K. Bean, D. Kass, R. Haberle, C. Newman, M. Mischna, A. Vasavada, N. Rennó, J. Bell, F. Calef, B. Cantor, T.H. Mcconnochie, A.-M. Harri, M. Genzer, M. Wong, M.D. Smith, F. Javier Martín-Torres, M.-P. Zorzano, O. Kemppinen, E. McCullough, Atmospheric movies acquired at the Mars Science Laboratory landing site: cloud morphology, frequency and significance to the Gale Crater water cycle and Phoenix mission results. Adv. Space Res. **55**, 2217–2238 (2015b)

P. Morgan, M. Grott, B. Knapmeyer-Endrun, M. Golombek, P. Delage, P. Lognonné, S. Piqueux, I. Daubar, N. Murdoch, C. Charalambous, W.T. Pike, N. Müller, A. Hagermann, M. Siegler, R. Lichtenheldt, N. Teanby, S. Kedar, A pre-landing assessment of regolith properties at the InSight landing site. Space Sci. Rev. **214**(6), 104 (2018). https://doi.org/10.1007/s11214-018-0537-y

M. Mucciarelli, M.R. Gallipoli, D. Di Giacomo, F. Di Nota, E. Nino, The influence of wind on measurements of seismic noise. Geophys. J. Int. **161**(2), 303–308 (2005)

D.P. Mulholland, P.L. Read, S.R. Lewis, Simulating the interannual variability of major dust storms on Mars using variable lifting thresholds. Icarus **223**, 344–358 (2013)

D.P. Mulholland, A. Spiga, C. Listowski, P.L. Read, An assessment of the impact of local processes on dust lifting in martian climate models. Icarus **252**, 212–227 (2015)

D.P. Mulholland, S.R. Lewis, P.L. Read, J.-B. Madeleine, F. Forget, The solsticial pause on Mars, 2: modelling and investigation of causes. Icarus **264**, 465–477 (2016)

N. Murdoch, B. Kenda, T. Kawamura, A. Spiga, P. Lognonné, D. Mimoun, W.B. Banerdt, Estimations of the seismic pressure noise on Mars determined from large eddy simulations and demonstration of pressure decorrelation techniques for the Insight Mission. Space Sci. Rev. (2017a)

N. Murdoch, D. Mimoun, R. Garcia, W. Rapin, T. Kawamura, P. Lognonné, Evaluating the wind-induced mechanical noise on the InSight seismometers. Space Sci. Rev. (2017b)

N. Murdoch, D. Alazard, N. Teanby, R. Myhill, B. Knapmeyer-Endrum, Flexible mode modelling of the InSight lander and consequences for the SEIS instrument. Space Sci. Rev. (2018 submitted for publication)

J.R. Murphy, S. Nelli, Mars Pathfinder convective vortices: frequency of occurrence. Geophys. Res. Lett. **29**(23), 230000 (2002)

J. Murphy, K. Steakley, M. Balme, G. Deprez, F. Esposito, H. Kahanpää, M. Lemmon, R. Lorenz, N. Murdoch, L. Neakrase, M. Patel, P. Whelley, Field measurements of terrestrial and martian dust devils. Space Sci. Rev. **203**(1), 39–87 (2016)

Y. Nakamura, D.L. Anderson, Martian wind activity detected by a seismometer at Viking lander 2 site. Geophys. Res. Lett. **6**, 499–502 (1979)

L.D.V. Neakrase, M.R. Balme, F. Esposito, T. Kelling, M. Klose, J.F. Kok, B. Marticorena, J. Merrison, M. Patel, G. Wurm, Particle lifting processes in dust devils. Space Sci. Rev. **203**(1), 347–376 (2016)

C.E. Newman, J. Gómez-Elvira, M. Marin, S. Navarro, J. Torres, M.I. Richardson, J.M. Battalio, S.D. Guzewich, R. Sullivan, M. de la Torre, A.R. Vasavada, N.T. Bridges, Winds measured by the rover environmental monitoring station (rems) during the mars science laboratory (msl) rover's bagnold dunes campaign and comparison with numerical modeling using marswrf. Icarus **291**(Suppl. C), 203–231 (2017)

A.O. Nier, W.B. Hanson, A. Seiff, M.B. McElroy, N.W. Spencer, R.J. Duckett, T.C.D. Knight, W.S. Cook, Composition and structure of the Martian atmosphere—preliminary results from Viking 1. Science **193**, 786–788 (1976)

Y. Nishikawa, P. Lognonné, T. Kawamura, A. Spiga, T. Bertrand, F. Forget, K. Kurita, Estimation and detection of Mars' background free oscillations for InSight mission. Space Sci. Rev. (2018 this issue)

S. Nishizawa, M. Odaka, Y.O. Takahashi, K-i. Sugiyama, K. Nakajima, M. Ishiwatari, S-i. Takehiro, H. Yashiro, Y. Sato, H. Tomita, Y.-Y. Hayashi, Martian dust devil statistics from high-resolution large-eddy simulations. Geophys. Res. Lett. **43**(9), 4180–4188 (2016). 2016GL068896

I. Ordonez-Etxeberria, R. Hueso, A. Sánchez-Lavega, A systematic search of sudden pressure drops on Gale crater during two Martian years derived from MSL/REMS data. Icarus **299**, 308–330 (2018)

A.A. Pankine, L.K. Tamppari, J.L. Bandfield, T.H. McConnochie, M.D. Smith, Retrievals of martian atmospheric opacities from MGS TES nighttime data. Icarus **226**, 708–722 (2013)

M.P. Panning, P. Lognonné, W. Bruce Banerdt, R. Garcia, M. Golombek, S. Kedar, B. Knapmeyer-Endrun, A. Mocquet, N.A. Teanby, J. Tromp, R. Weber, E. Beucler, J.-F. Blanchette-Guertin, E. Bozdağ, M. Drilleau, T. Gudkova, S. Hempel, A. Khan, V. Lekić, N. Murdoch, A.-C. Plesa, A. Rivoldini, N. Schmerr, Y. Ruan, O. Verhoeven, C. Gao, U. Christensen, J. Clinton, V. Dehant, D. Giardini, D. Mimoun, W. Thomas Pike, S. Smrekar, M. Wieczorek, M. Knapmeyer, J. Wookey, Planned products of the Mars structure service for the InSight mission to Mars. Space Sci. Rev. **211**, 611–650 (2017)

M.D. Paton, A.-M. Harri, H. Savijärvi, Measurement of Martian boundary layer winds by the displacement of jettisoned lander hardware. Icarus **309**, 345–362 (2018)

A. Petculescu, R.M. Lueptow, Atmospheric acoustics of Titan, Mars, Venus, and Earth. Icarus **186**(2), 413–419 (2007)

A. Petrosyan, B. Galperin, S.E. Larsen, S.R. Lewis, A. Määttänen, P.L. Read, N. Renno, L.P.H.T. Rogberg, H. Savijärvi, T. Siili, A. Spiga, A. Toigo, L. Vázquez, The Martian atmospheric boundary layer. Rev. Geophys. **49**, 3005 (2011)

A.O. Pickersgill, G.E. Hunt, The formation of Martian lee waves generated by a crater. J. Geophys. Res. **84**(B14), 8317–8331 (1979)

J. Pla-Garcia, S.C.R. Rafkin, M. Kahre, J. Gomez-Elvira, V.E. Hamilton, S. Navarro, J. Torres, M. Marín, A.R. Vasavada, The meteorology of Gale crater as determined from rover environmental monitoring station observations and numerical modeling. Part I: Comparison of model simulations with observations. Icarus **280**, 103–113 (2016)

A.-C. Plesa, M. Grott, M.T. Lemmon, N. Müller, S. Piqueux, M.A. Siegler, S.E. Smrekar, T. Spohn, Interannual perturbations of the Martian surface heat flow by atmospheric dust opacity variations. J. Geophys. Res., Planets **121**, 2166–2175 (2016)

J.B. Pollack, M.E. Ockert-Bell, M.K. Shepard, Viking Lander image analysis of Martian atmospheric dust. J. Geophys. Res. **100**, 5235–5250 (1995)

A. Pottier, F. Forget, F. Montmessin, T. Navarro, A. Spiga, E. Millour, A. Szantai, J.-B. Madeleine, Unraveling the martian water cycle with high-resolution global climate simulations. Icarus (2017)

S.C.R. Rafkin, J. Pla-Garcia, M. Kahre, J. Gomez-Elvira, V.E. Hamilton, M. Marín, S. Navarro, J. Torres, A. Vasavada, The meteorology of Gale Crater as determined from Rover Environmental Monitoring Station observations and numerical modeling, part II: interpretation. Icarus **280**, 114–138 (2016)

P.L. Read, S.R. Lewis, *The Martian Climate Revisited: Atmosphere and Environment of a Desert Planet* (Springer, New York, 2004)

D. Reiss, R.D. Lorenz, Dust devil track survey at Elysium planitia, Mars: implications for the insight landing sites. Icarus **266**, 315–330 (2016)

D. Reiss, A. Spiga, G. Erkeling, The horizontal motion of dust devils on Mars derived from CRISM and CTX/HiRISE observations. Icarus **227**, 8–20 (2014)

T.J. Ringrose, M.C. Towner, J.C. Zarnecki, Convective vortices on Mars: a reanalysis of Viking Lander 2 meteorological data, sols 1-60. Icarus **163**, 78–87 (2003)

D.M. Rubin, R.E. Hunter, Bedform alignment in directionally varying flows. Science **237**, 276–278 (1987)

S.W. Ruff, P.R. Christensen, D.L. Blaney, W.H. Farrand, J.R. Johnson, J.R. Michalski, J.E. Moersch, S.P. Wright, S.W. Squyres, The rocks of Gusev Crater as viewed by the Mini-TES instrument. Journal of Geophysical Research (Planets) **111**, E12S18 (2006)

C. Russell, D. Banfield, W. Banerdt, co authors, The InSight magnetometer (2018). Submitted to this Space Science Reviews special issue

J.A. Ryan, R.M. Henry, Mars atmospheric phenomena during major dust storms as measured at surface. J. Geophys. Res. **84**, 2821–2829 (1979)

J.A. Ryan, R.D. Sharman, Two major dust storms, one Mars year apart—comparison from Viking data. J. Geophys. Res. **86**, 3247–3254 (1981)

H. Savijärvi, Radiative fluxes on a dust free Mars. Contrib. Atmos. Phys. **2**, 103–112 (1991)

H. Sävijarvi, A model study of the atmospheric boundary layer in the Mars Pathfinder lander conditions. Q. J. R. Meteorol. Soc. **125**(554), 483–493 (1999)

M. Schimmel, Phase cross-correlations: Design, comparisons, and applications. Bull. Seismol. Soc. Am. **89**(5), 1366–1378 (1999)

M. Schimmel, E. Stutzmann, F. Ardhuin, J. Gallart, Polarized earth's ambient microseismic noise. Geochem. Geophys. Geosyst. **12**(7) (2011)

E.D. Schmitter, Brief communication "Modeling tornado dynamics and the generation of infrasound, electric and magnetic fields". Nat. Hazards Earth Syst. Sci. **10**(2), 295–298 (2010)

J.T. Schofield, D. Crisp, J.R. Barnes, R.M. Haberle, J.A. Magalhaães, J.R. Murphy, A. Seiff, S. Larsen, G. Wilson, The Mars Pathfinder Atmospheric Structure Investigation/Meteorology (ASI/MET) experiment. Science **278**, 1752–1757 (1997)

E. Sefton-Nash, N. Teanby, L. Montabone, P. Irwin, J. Hurley, S. Calcutt, Climatology and first-order composition estimates of mesospheric clouds from Mars climate sounder limb spectra. Icarus **222**(1), 342–356 (2013)

E. Sefton-Nash, N.A. Teanby, C. Newman, R.A. Clancy, M.I. Richardson, Constraints on Mars' recent equatorial wind regimes from layered deposits and comparison with general circulation model results. Icarus **230**, 81–95 (2014)

A. Seiff, D.B. Kirk, Structure of Mars' atmosphere up to 100 kilometers from the entry measurements of Viking 2. Science **194**, 1300–1303 (1976)

A. Seiff, J.E. Tillman, J.R. Murphy, J.T. Schofield, D. Crisp, J.R. Barnes, C. LaBaw, C. Mahoney, J.D. Mihalov, G.R. Wilson, R. Haberle, The atmosphere structure and meteorology instrument on the Mars Pathfinder lander. J. Geophys. Res., Planets **102**, 4045–4056 (1997)

M.D. Smith, Interannual variability in TES atmospheric observations of Mars during 1999–2003. Icarus **167**, 148–165 (2004)

P.H. Smith, M. Lemmon, Opacity of the Martian atmosphere measured by the Imager for Mars Pathfinder. J. Geophys. Res., Planets **104**, 8975–8986 (1999)

M.D. Smith, M.J. Wolff, N. Spanovich, A. Ghosh, D. Banfield, P.R. Christensen, G.A. Landis, S.W. Squyres, One Martian year of atmospheric observations using MER Mini-TES. J. Geophys. Res., Planets **111**(E10), 12 (2006)

G.G. Sorrells, A preliminary investigation into the relationship between long-period seismic noise and local fluctuations in the atmospheric pressure field. Geophys. J. **26**, 71–82 (1971)

N. Spanovich, M.D. Smith, P.H. Smith, M.J. Wolff, P.R. Christensen, S.W. Squyres, Surface and near-surface atmospheric temperatures for the Mars Exploration Rover landing sites. Icarus **180**, 314–320 (2006)

A. Spiga, Comment on "Observing desert dust devils with a pressure logger" by Lorenz (2012)—insights on measured pressure fluctuations from large-eddy simulations. Geosci. Instrum. Method. Data Syst. **1**(2), 151–154 (2012)

A. Spiga, F. Forget, A new model to simulate the Martian mesoscale and microscale atmospheric circulation: validation and first results. J. Geophys. Res., Planets **114**, E02009 (2009)

A. Spiga, F. Forget, B. Dolla, S. Vinatier, R. Melchiorri, P. Drossart, A. Gendrin, J.-P. Bibring, Y. Langevin, B. Gondet, Remote sensing of surface pressure on Mars with the Mars Express/OMEGA spectrometer, 2: meteorological maps. J. Geophys. Res., Planets **112**(E11), 8 (2007)

A. Spiga, F. Forget, S.R. Lewis, D.P. Hinson, Structure and dynamics of the convective boundary layer on mars as inferred from large-eddy simulations and remote-sensing measurements. Q. J. R. Meteorol. Soc. **136**, 414–428 (2010)

A. Spiga, F. González-Galindo, M-Á. López-Valverde, F. Forget, Gravity waves, cold pockets and CO_2 clouds in the Martian mesosphere. Geophys. Res. Lett. **39**, 2201 (2012)

A. Spiga, J. Faure, J.-B. Madeleine, A. Määttänen, F. Forget, Rocket dust storms and detached dust layers in the Martian atmosphere. J. Geophys. Res., Planets **118**, 746–767 (2013)

A. Spiga, E. Barth, Z. Gu, F. Hoffmann, J. Ito, B. Jemmett-Smith, M. Klose, S. Nishizawa, S. Raasch, S. Rafkin, T. Takemi, D. Tyler, W. Wei, Large-eddy simulations of dust devils and convective vortices. Space Sci. Rev. **203**, 245–275 (2016)

T. Spohn, M. Grott, S.E. Smrekar, J. Knollenberg, T.L. Hudson, C. Krause, N. Müller, J. Jänchen, A. Börner, T. Wippermann, O. Krömer, R. Lichtenheldt, L. Wisniewski, J. Grygorczuk, M. Fittock, S. Rheershemius, T. Spröwitz, E. Kopp, I. Walter, A.C. Plesa, D. Breuer, P. Morgan, W.B. Banerdt, The heat flow and physical properties package (HP3) for the InSight mission. Space. Sci. Rev. **214**(5), 96 (2018). https://doi.org/10.1007/s11214-018-0531-4

T. Statella, P. Pina, E.A. da Silva, Image processing algorithm for the identification of Martian dust devil tracks in MOC and HiRISE images. Planet. Space Sci. **70**, 46–58 (2012)

L.J. Steele, M.R. Balme, S.R. Lewis, A. Spiga, The water cycle and regolith-atmosphere interaction at Gale crater, Mars. Icarus **289**, 56–79 (2017)

J. Stevanović, N.A. Teanby, J. Wookey, N. Selby, I.J. Daubar, J. Vaubaillon, R. Garcia, Bolide airbursts as a seismic source for the 2018 mars insight mission. Space Sci. Rev. **211**(1), 525–545 (2017)

N. Suda, K. Nawa, Y. Fukao, Earth's background free oscillations. Science **279**, 2089 (1998)

R. Sullivan, R. Greeley, M. Kraft, G. Wilson, M. Golombek, K. Herkenhoff, J. Murphy, P. Smith, Results of the Imager for Mars Pathfinder windsock experiment. J. Geophys. Res. **105**, 24547–24562 (2000)

J.L. Sutton, C.B. Leovy, J.E. Tillman, Diurnal variations of the Martian surface layer meteorological parameters during the first 45 sols at two Viking lander sites. J. Atmos. Sci. **35**, 2346–2355 (1978)

P.A. Taylor, D.C. Catling, M. Daly, C.S. Dickinson, H.P. Gunnlaugsson, A.-M. Harri, C.F. Lange, Temperature, pressure, and wind instrumentation in the Phoenix meteorological package. J. Geophys. Res., Planets **113**, E00A10 (2008)

N.A. Teanby, J. Stevanović, J. Wookey, N. Murdoch, J. Hurley, R. Myhill, N.E. Bowles, S.B. Calcutt, W.T. Pike, Seismic coupling of short-period wind noise through Mars' regolith for NASA's InSight Lander. Space Sci. Rev. **211**, 485–500 (2017)

P.C. Thomas, P.B. James, W.M. Calvin, R. Haberle, M.C. Malin, Residual south polar cap of Mars: stratigraphy, history, and implications of recent changes. Icarus **203**, 352–375 (2009)

N. Thomas, G. Cremonese, R. Ziethe, M. Gerber, M. Brändli, G. Bruno, M. Erismann, L. Gambicorti, T. Gerber, K. Ghose, M. Gruber, P. Gubler, H. Mischler, J. Jost, D. Piazza, A. Pommerol, M. Rieder, V. Roloff, A. Servonet, W. Trottmann, T. Uthaicharoenpong, C. Zimmermann, D. Vernani, M. Johnson, E. Pelò, T. Weigel, J. Viertl, N. De Roux, P. Lochmatter, G. Sutter, A. Casciello, T. Hausner, I. Ficai Veltroni, V. Da Deppo, P. Orleanski, W. Nowosielski, T. Zawistowski, S. Szalai, B. Sodor, S. Tulyakov, G. Troznai, M. Banaskiewicz, J. Bridges, S. Byrne, S. Debei, M. El-Maarry, E. Hauber, C. Hansen, A. Ivanov, L. Keszthelyi, R. Kirk, R. Kuzmin, N. Mangold, L. Marinangeli, W. Markiewicz, M. Massironi, A. McEwen, C. Okubo, L. Tornabene, P. Wajer, J. Wray, The Colour and Stereo Surface Imaging System (CaSSIS) for the ExoMars Trace Gas Orbiter. Space Sci. Rev., 1897–1944 (2017)

J.E. Tillman, R.M. Henry, S.L. Hess, Frontal systems during passage of the Martian north polar hood over thet Viking lander 2 site prior to the first 1977 dust storm. J. Geophys. Res. **84**(B6), 2947–2955 (1979)

J.E. Tillman, L. Landberg, S.E. Larsen, The boundary layer of Mars: fluxes stability, turbulent spectra and growth of the mixed layer. J. Atmos. Sci. **51**(12), 1709–1727 (1994)

M.G. Tomasko, L.R. Doose, M. Lemmon, P.H. Smith, E. Wegryn, Properties of dust in the Martian atmosphere from the Imager on Mars Pathfinder. J. Geophys. Res. **104**, 8987–9008 (1999)

A. Trebi-Ollennu, W. Kim, K. Ali, O. Khan, C. Sorice, P. Bailey, J. Umland, R. Bonitz, C. Ciarleglio, J. Knight, N. Haddad, K. Klein, S. Nowak, D. Klein, N. Onufer, K. Glazebrook, B. Kobeissi, E. Baez, F. Sarkissian, M. Badalian, H. Abarca, R.G. Deen, J. Yen, S. Myint, J. Maki, A. Pourangi, J. Grinblat, B. Bone, N. Warner, J. Singer, J. Ervin, J. Lin, InSight Mars lander robotics instrument deployment system. Space Sci. Rev. **214**(5), 93 (2018). https://doi.org/10.1007/s11214-018-0520-7

D. Tyler, J.R. Barnes, Convergent crater circulations on Mars: influence on the surface pressure cycle and the depth of the convective boundary layer. Geophys. Res. Lett. **42**, 2015GL064957 (2015)

D. Tyler, J.R. Barnes, E.D. Skyllingstad, Mesoscale and large-eddy simulation model studies of the Martian atmosphere in support of Phoenix. J. Geophys. Res., Planets **113**(E12) (2008)

A. Ullán, M.-P. Zorzano, F. Javier Martín-Torres, P. Valentín-Serrano, H. Kahanpää, A.-M. Harri, J. Gómez-Elvira, S. Navarro, Analysis of wind-induced dynamic pressure fluctuations during one and a half Martian years at Gale Crater. Icarus **288**, 78–87 (2017)

G.K. Vallis, *Atmospheric and Oceanic Fluid Dynamics: Fundamentals and Large-Scale Circulation* (Cambridge Univ. Press, London, 2006)

B. Van Hove, ö. Karatekin, Observing the martian atmosphere using entry probe flight instrumentation, in *Mars Atmosphere: Modelling and Observation, 5th International Workshop*, ed. by F. Forget, M. Millour (2014), p. 4401

A.R. Vasavada, A. Chen, J.R. Barnes, P.D. Burkhart, B.A. Cantor, A.M. Dwyer-Cianciolo, R.L. Fergason, D.P. Hinson, H.L. Justh, D.M. Kass, S.R. Lewis, M.A. Mischna, J.R. Murphy, S.C.R. Rafkin, D. Tyler,

P.G. Withers, Assessment of environments for mars science laboratory entry, descent, and surface operations. Space Sci. Rev., 55 (2012)

C.A. Verba, P.E. Geissler, T.N. Titus, D. Waller, Observations from the High Resolution Imaging Science Experiment (HiRISE): Martian dust devils in Gusev and Russell craters. J. Geophys. Res., Planets **115**, E09002 (2010)

M. Vincendon, J. Audouard, F. Altieri, A. Ody, Mars Express measurements of surface albedo changes over 2004–2010. Icarus **251**, 145–163 (2015)

H. Wang, M.I. Richardson, The origin, evolution, and trajectory of large dust storms on Mars during Mars years 24–30 (1999–2011). Icarus **251**, 112–127 (2015)

H. Wang, M.I. Richardson, R.J. Wilson, A.P. Ingersoll, A.D. Toigo, R.W. Zurek, Cyclones, tides, and the origin of a cross-equatorial dust storm on Mars. Geophys. Res. Lett. **30**, 1488 (2003)

R.J. Warburton, J.M. Goodkind, The influence of barometric pressure variations on gravity. Geophys. J. R. Astron. Soc. **48**, 281–292 (1977)

R.W. Wilson, K. Hamilton, Comprehensive model simulation of thermal tides in the Martian atmosphere. J. Atmos. Sci. **53**, 1290–1326 (1996)

R.J. Wilson, J.M. Murphy, D. Tyler, Assessing atmospheric thermal forcing from surface pressure data: separating thermal tides and local topographic influence, in *The Mars Atmosphere: Modelling and observation*, ed. by F. Forget, M. Millour (2017), p. 1111

P. Withers, D.C. Catling, Observations of atmospheric tides on Mars at the season and latitude of the Phoenix atmospheric entry. Geophys. Res. Lett. **37** (2010)

P. Withers, M.D. Smith, Atmospheric entry profiles from the Mars exploration rovers spirit and opportunity. Icarus **185**, 133–142 (2006)

C. Wolfe, Using engineering cameras on mars rovers and landers to retrieve atmospheric dust loading. Master's thesis, Texas A & M University (2016). http://oaktrust.library.tamu.edu/handle/1969.1/158130

M.J. Wolff, R.T. Clancy, Constraints on the size of Martian aerosols from Thermal Emission Spectrometer observations. J. Geophys. Res., Planets **108**, 5097 (2003)

M.J. Wolff, R.T. Clancy, B. Cantor, R.M. Haberle, The MARCI water ice cloud optical depth (public) database, in *Mars Atmosphere: Modelling and Observation, 5th International Workshop*, ed. by F. Forget, M. Millour (2014), p. 2302

P. Wolkenberg, M.D. Smith, V. Formisano, G. Sindoni, Comparison of PFS and TES observations of temperature and water vapor in the martian atmosphere. Icarus **215**, 628–638 (2011)

A.P. Zent, M.H. Hecht, D.R. Cobos, S.E. Wood, T.L. Hudson, S.M. Milkovich, L.P. DeFlores, M.T. Mellon, Initial results from the thermal and electrical conductivity probe (TECP) on Phoenix. J. Geophys. Res., Planets **115**, E00E14 (2010)

R.W. Zurek, Martian great dust storm, an update. Icarus **50**, 288–310 (1982)

W. Zürn, R. Widmer, On noise reduction in vertical seismic records below 2 mHz using local barometric pressure. Geophys. Res. Lett. **22**, 3537–3540 (1995)

W. Zürn, J. Exß, H. Steffen, C. Kroner, T. Jahr, M. Westerhaus, On reduction of long-period horizontal seismic noise using local barometric pressure. Geophys. J. Int. **171**, 780–796 (2007)